Alkaline dust deposition to foliage surfaces likely enhances the dry deposition velocity of SO_2: An investigation in the Alberta Oil-Sands Region using the GEM-MACH air-quality model

Stefan Miller[1], Paul A. Makar[1], Kenjiro Toyota[1], Colin Lee[1], Verica Savic-Jovcic[1], Sepehr Fathi[1], Mahtab Majdzadeh[1], Katherine Hayden[1],

[1]Environment and Climate Change Canada, Toronto, ON, Canada

Correspondence to: Paul Makar (paul.makar@ec.gc.ca), Stefan Miller (stefan.miller@ec.gc.ca)

For submission to the Atmospheric Chemistry and Physics Special Issue on regional model deposition (AQMEII-4)

Abstract.

We examine the potential impact of alkaline particle deposition on foliage and its influence on sulphur dioxide dry deposition velocities, using a new theoretical development, a high resolution air-quality model, and comparisons to observations. Our study domain encompasses the Athabasca Oil Sands Region, an industrial area where base cation-bearing fugitive dust from open-pit mining and forest fires coexists with elevated SO_2 emissions from large stacks. Our pH-modulated dry deposition scheme links thin aqueous films on foliage to local chemical conditions, including alkaline dust accumulation. We present the mechanism's theoretical basis, along with a simplified algorithm predicting foliage water pH and linked to SO_2 deposition velocities.

We predict enhanced SO_2 deposition, due to increased leaf surface pH from dust co-deposition near major dust sources, often by more than 1 cm s^{-1}. These result in dry deposition fluxes 2.5 to 10 times greater than in the absence of these effects - consistent with estimates from aircraft studies. The enhanced deposition reduces surface SO_2 concentrations by up to 60% near sources, improves agreement with continuous monitoring data, and reduces the normalized mean bias at several stations. Taylor diagram statistics show improved model temporal variability performance. Further from sources of base-cation-containing dust, aqueous films on foliage remain acidic, reducing SO_2 deposition velocity and increasing concentrations.

We make specific recommendations for new observation data which would reduce formulation uncertainties. The findings have broad implications for global SO_2 budgets, given the significant role of wind-blown mineral dust and forest fire base cation emissions in influencing atmospheric acidity and trace gas removal.

1 Introduction

1.1 Phase 4 of the Air Quality Model Evaluation International Initiative

Formatted: Heading 2

Recent intercomparisons between regional air-quality model predictions and observations in both North America and Europe under the AQMEII4 initiative (Makar et al., 2025) have shown that these regional models have a tendency towards positive biases in the concentrations of sulphur dioxide (SO_2) and particulate sulphate. One possible cause of these positive biases are underestimates in the deposition velocity of SO_2, which if corrected would result in lower SO_2 concentrations and hence reduced production of particulate sulphate via SO_2 oxidation. Enhanced deposition of SO_2 through its co-deposition with ammonia (NH_3) has been reported in the past (cf. Fowler et al., 2001; Flechard et al., 1999; Nemitz et al., 2001). However, in addition to ammonia,

substantial deposition fluxes of other reactive base cations in the form of depositing dust have been recorded (Scheuvens et al., 2013, Wang et al., 2005, Avila et al., 1998, Rosas et al., 2025). These deposition fluxes may also influence the rate of SO_2 deposition. ~~,~~ ~~h~~However, a detailed process description of this influence has been heretofore unavailable. We examine here the potential ~~the~~ for simultaneous co-deposition of multiple base cations and acidic gases including SO_2, making use of a case study domain in the Athabasca Oil Sands Region, reporting the results as part of the AQMEII4 special issue on deposition.

1.2 Deposition in the Athabasca Oil Sands Region – Evidence for pH-modulation

Formatted: Heading 2

The Athabasca Oil Sands Region (AOSR) in northeastern Alberta, Canada contains one of the world's largest bitumen reserves, spanning approximately 142,000 km^2 (Government of Alberta, last access: June 30th, 2025). It is well established that this region is a significant source of various gaseous and particulate emissions (You et al., 2024; Zhang et al., 2018; Li et al., 2017). Among these, sulphur dioxide (SO_2) has drawn particular attention due to its known potential to adversely impact ecosystem health. SO_2 plays a central role in the development of acid rain (Irwin and Williams, 1988; Clark and Radojevic, 1987) and acid fog (Pandis and Seinfeld, 1989; Munger et al., 1983), both of which have been implicated in widespread ecosystem degradation throughout the world (Hames et al., 2002; Cape 1993; Cox et al., 1989; Schindler et al., 1989; Gilbert 1986; Hutchinson and Whitby, 1977). An input of excess SO_2 and particle sulphate (SO_4^{2-}) onto plant foliage can disrupt metabolic function (Rennenberg 1984; Knabe, 1976), cause irreversible damage to guard cells that regulate stomatal activity (Knabe, 1976), and may lead to leaf necrosis or plant mortality in sensitive species (Hutchinson and Whitby, 1977; Gordon and Gorham, 1963).

Two recent measurement campaigns in the AOSR investigated dry deposition of oxidized sulphur. The first wa~~i~~s an aircraft-based study (13 Aug to 7 Sep 2013; Hayden et al., 2021), which showed that dry deposition fluxes of total oxidized sulphur (SO_2 + particulate SO_4) decrease exponentially with increasing distance downwind from major AOSR sources. Their inferred deposition fluxes were 2 to 14 times higher than predicted by the GEM-MACH model (Makar et al., 2018), with inferred SO_2 deposition velocities ($V_{d_{SO_2}}$) of 1.2 to 3.4 cm s^{-1}, compared to modelled values of 0.58 to 0.72 cm s^{-1}. Additional ground-based measurements at Fort McKay (6 to 8 June 2018) yielded even higher median $V_{d_{SO_2}}$ values (median: 4.1 cm s^{-1}; range: 2.9 to 5.3 cm s^{-1}). Both the aircraft and Fort McKay tower data reflect daytime conditions. The second study (Gordon et al., 2022) involved continuous tower based SO_2 measurements from July to October 2021 at a forest site approximately 40 km north of Fort McMurray (located within the AOSR). Using the flux-gradient method, they reported inferred $V_{d_{SO_2}}$ values of 2.1 to 5.9 cm s^{-1} (mean: 4.6 cm s^{-1}), in agreement with the range reported by Hayden et al. (2021). These data may include both daytime and nighttime periods, although Gordon et al. (2022) acknowledge greater uncertainty during stable nighttime atmospheric conditions. Given the typically lower $V_{d_{SO_2}}$ at night due to an increased aerodynamic resistance (Wu et al., 2018; Finkelstein et al., 2000), the reported range likely remains dominated by higher daytime deposition events.

To investigate the discrepancy in $V_{d_{SO_2}}$ found between their observations and the model predictions from GEM-MACH, Hayden et al. (2021) performed a Monte Carlo simulation using five common inferential dry deposition algorithms (Wu et al., 2018; Makar et al, 2018). They employed this approach to study the importance of various parameters, including foliage pH. The Monte Carlo simulation demonstrated that $V_{d_{SO_2}}$ can be highly sensitive to the choice of foliage pH assumed in an algorithm developed by Wesely (1989) for cuticular resistance calculation, which is used in GEM-MACH. For example, as the foliage pH is increased from 6.68 to 8.0, the $V_{d_{SO_2}}$ predicted by the GEM-MACH algorithm shifted~~s~~ from 0.6 to 1.4 cm s^{-1}. However, the foliage pH in such ~~an~~ algorithms is usually assumed to represent neutral or near-neutral conditions; in GEM-MACH, the foliage pH is assumed to be constant at 6.68 (Makar et al, 2018). Hayden et al. (2021) hypothesized that the deposition of anthropogenic dust to forests downwind of the AOSR might cause the pH of foliage water layers to become alkaline (higher pH levels), in turn

leading to an increase in $V_{d_{SO_2}}$ (see Sect. 3). To support this hypothesis, the remainder of this Introduction summarizes key processes influencing foliage surface pH, including canopy particle deposition, leaf water dynamics, and dust-gas interactions, which form the foundation for our modelling approach.

1.3 Foliage Surface pH and Alkaline Dust

Formatted: Heading 2, Indent: First line: 0 cm

The importance of leaf surface water pH on determining $V_{d_{SO_2}}$ over wet foliage surfaces is cited in the development papers of some inferential dry deposition algorithms (Wesley 1989; Erisman, 1994). Moreover, the effect of pH on $V_{d_{SO_2}}$ has been demonstrated explicitly by wind tunnel measurements investigating the co-deposition of SO_2 and NH_3 into thin water layers (Adema and Heeres 1995), by field observations of foliage water pH made after precipitation (Wu et el., 2016; Neirynck et al., 2011), and by a leaf-scale model that predicts the pH of foliage water layers to better simulate the dry deposition of NH_3 (Flechard et al., 1999). To the authors' knowledge, the impact of base cation co-deposition with SO_2 has remained unstudied in the literature.

The assumption of alkaline material on foliage surfaces in the forests downwind of the AOSR is supported by in-situ measurements of particulate matter (PM) obtained from the processing facilities. The AOSR emits substantial primary and secondary PM from multiple sources, including surface mining and quarrying, bitumen extraction and processing, vehicle-induced dust on haul roads, natural gas power generation and natural sources such as soil erosion and forest fires (Zhang et al., 2018). Oil Sands processing is the dominant PM source (43 – 60 %), with surface mining and haul-road dust contributing 22 to 46 % (Wang et al., 2015; Mamun et al., 2021; Landis et al., 2019). Wang et al. (2015) analysed 27 dust samples from the AOSR and found (i) a significant amount of water-soluble Na^+ originates from sodium hydroxide (NaOH) used during bitumen extraction (Tamiz Bakhtiari et al., 2015) and road salt, (ii) Ca mostly in ionic form, with an abundance of calcite ($CaCO_3$) and some dolomite ($CaMg(CO_3)_2$), and (iii) consistently basic dust, with ratios of measured of cations/anions > 1.0. Similarly, Watson et al., (2014) found that without accounting for the carbonate ion (CO_3^2) in the charge balance equation, cations in AOSR dust were 11 to 12 times more abundant than anions on average. With CO_3^{2-} included, anions were about 55 % greater than cations on average. These studies confirm that AOSR dust is rich in base cations such as Ca^{2+}, Mg^{2+}, K^+ and Na^+.

The significance of alkaline dust towards deposition fluxes in the AOSR has also been demonstrated in throughfall measurements made in the boreal forest adjacent to the processing facilities. Watmough et al., (2019) found that within 3 km of open pit mines, deposition of Ca^{2+}, Mg^{2+} and Na^+ exceeded that of sulphur and nitrogen combined, with Ca^{2+} dominating base cation inputs. Similarly, Proemse et al., (2016) reported elevated calcium levels in ground Jack Pine needles collected at various distances downwind of Oil Sands facilities. Previous GEM-MACH modelling by Makar et al., (2018) indicated that base cations likely remain in excess up to 140 km downwind, suggesting that alkaline soil and foliage conditions may persist over this regional scale.

Outside of the AOSR, the impact of alkaline dust deposition on vegetation and soil health has been documented downwind of cement plants and limestone quarries. When moisture is present, dissolved cement-kiln dust can reach pH values of 10 to 13 due to high hydroxyl ion concentrations (Darley, 1966; Mandre and Tuulmets, 1995; Siqueira-Silva et al. 2016). Similarly, hydrated dust collected from foliage near a limestone quarry had pH values between 9 and 11 (Manning, 1971). Cement-kiln dust may contain up to 36 % acid-extractable base cations (Ca^{2+}, K^+, Na^+) by mass (Darely, 1966), whereas AOSR-derived dust contains about 5–6 % ionic base cations, primarily as Ca^{2+}, Mg^{2+}, K^+, and Na^+ (Wang et al., 2015). Despite this lower concentration, the base cation content in AOSR dust is sufficient to neutralize the observed ~2% SO_4^{2-} content, (Wang et al., 2015), suggesting a likely excess of alkaline species such as $CaCO_3$. Under moist conditions, this chemical composition can raise surface pH on foliage, paralleling effects observed near cement plants and limestone quarries. Supporting evidence comes from dew studies using inert surfaces (i.e., Teflon), which show that dew pH can exceed 8, and sometimes 10, in regions with significant alkaline

dust deposition (Odeh et al., 2017; Beysens et al., 2017; Lekouch et al., 2010). In contrast, dew in regions without significant alkaline dust deposition has a pH typically ranging from 3 and 7 (Wisniewski 1986; Pierson et al., 1986; Foster et al., 1990; Hughes and Brimblecombe 1993; Beysens et al., 2006; Wentworth et al., 2016), with the most acidic values (i.e., pH < 4) reported downwind of major roadways due to acid deposition (Fluckiger-Keller et al., 1978). We note here that the AOSR has sources of both anions and cations – the former from emissions of SO_2 and NO_x from large stacks and off-road vehicle fleets, and the latter from fugitive dust (Zhang et al., 2018). Both acidifying and neutralizing deposition in the AOSR would thus be expected (Makar et al., 2018).

1.4 Particle and Gas Deposition and Foliage

Formatted: Heading 2, Indent: First line: 0 cm

Particulate matter, such as dust, is deposited onto foliage through 'dry' physical processes, including gravitational sedimentation, Brownian diffusion, turbulent impaction and interception, but also through 'wet' processes such as precipitation and fog (occult deposition). Dry deposition dominates PM accumulation on foliage outside of persistently wet regions, and to a first order approximation, wet deposition can be neglected in a simplified process model representation (Freer-Smith et al., 2005). In general, the dry deposition characteristic of a particle is strongly affected by its diameter (D_p) and velocity, and so these factors strongly impact the canopy collection efficiency of PM (Emerson et al., 2020). The canopy collection efficiency of particles is defined here as the fraction of particle dry deposition that is to the forest canopy as opposed to the ground surface under the canopy. For foliar deposition of ultrafine particles ($D_p \leq 0.1\mu m$), Brownian diffusion is the most efficient dry deposition mechanism, while for particles in the PM_{10} range ($0.1 < D_p \leq 10$ μm) interception and impaction dominate (Tiwary et al., 2005; Beckett et al., 2000). The sedimentation process becomes significant only for coarse particles ($D_p > 8$ μm) (Beckett et al.,1998, 2000). Wind speed also enhances the rate of particle dry deposition by increasing particle velocity (Beckett et al., 2000; Hwang et al., 2011). More recent work by Emerson et al. (2020) compared observed deposition velocities as a function of size and vegetation classes, with a shift of the minimum deposition velocity to smaller sizes, and higher deposition velocities for the coarse mode. Once deposited, some PM may eventually become encapsulated into the leaf wax, especially when deposited onto newly expanding foliage, where it typically remains until leaf senescence (Przybysz et al., 2014).

Beyond particle specific properties, vegetation type plays a key role in determining the canopy PM collection efficiency. Coniferous species generally capture more PM than broadleaf species, particularly in the $PM_{2.5}$ size range ($0.1 < D_p \leq 2.5$ μm) due to their narrow needle-like foliage and associated aerodynamic properties (Emmerson et al., 2020; Chen et al., 2017; Przybysz et al., 2014; Hwang et al., 2011; Freer-Smith et al., 2005). This difference is reflected in the Stokes number, which is higher for conifers (~0.05) than for broadleaf species (~1.2×10^{-5}), and in the thickness of the leaf-boundary layer, which is thinner in conifers, enhancing the deposition efficiency (Beckett et al., 2000; Chen et al., 2017). The leaf-boundary layer is defined as the region of the atmosphere near the leaf surface where a reduction of the ambient wind speed occurs due to surface friction, impacting mass exchange (Schuepp 1993; Grace and Wilson, 1975). At the leaf level, traits such as high surface roughness (i.e., wrinkles, ridges, furrows and folds), abundant leaf hairs and glandular secretions have all been correlated to an increased PM capture efficiency (Corada et al. 2021; Chen et al., 2017). While PM can deposit to both sides of leaf surfaces, it typically accumulates more on the upper side (Ottelé et al., 2010). However, when leaf hairs are present only on the underside, that surface can become the dominant location of PM deposition (Hwang et al., 2011). Canopy collection efficiencies of PM vary between 0.40 to 0.95, with higher values observed for coarse PM and dense forests (Emerson et al., 2020; Pryor et al., 2013; Gronholm et al., 2009; Donat and Ruck 1999). Spatial variability within forests also matters: deposition is typically greater near forest edges than within the forest interior (Raynor et al., 1974; Draaijers et al., 1994; Ould-Dada et al., 2002; Wuyts et al., 2008).

In addition to PM, gaseous species are also deposited to foliage, but through a broader range of pathways. While PM typically deposits only to the external leaf surface (except perhaps ultrafine particles), gases and their chemical transformation products can also be accommodated onto the external surface (i.e., dry cuticles, drops and thin layers of dew water) or be assimilated by the leaf through the stomata. For example, over 80 % of HNO_3 is deposited to the external leaf surface and can be directly recovered via leaf washing (Cadle et al., 1991; Dasch 1989). In contrast, SO_2 shows more variable behaviour; the percentage deposited to the external leaf surface can range from near 0 to greater than 40 %, with the remainder assimilated into the leaf interior via the stomata (Dasch 1989; Taylor et al., 1983; Fowler and Unsworth 1979).

1.5 Removal of Deposited Material from Foliage

Formatted: Heading 2, Indent: First line: 0 cm

Estimating leaf surface pH in the presence of exogenous substances requires accounting for the removal fluxes of deposited ions and gases from the foliage surfaces. Once deposited, any mass (i.e., particle or gas) not immobilized by leaf waxes can be removed from the foliage and transferred to the ground or lower canopy layers. Under dry conditions, strong winds can remove PM either by directly dislodging particles from the leaf surface or through branch movement (Zheng and Li 2019; Ould-Dada and Baghini, 2001). However, outside of extremely arid regions, precipitation is the dominant removal process (Popek et al. 2019). During rainfall, soluble PM can dissolve in surface water and is typically washed off almost completely given sufficient runoff (Pullman 2009; Chiwa et al., 2003; Hansen et al. 1994; Potter and Ragsdale 1991; Fortmann and Johnson 1984; Carlson et al., 1976). In contrast, insoluble PM may remain adhered to the leaf surface regardless of precipitation intensity, duration or amount (Xu et al., 2024; Zhang et al., 2019; Xu et al., 2019; Cai et al., 2019; Weerakkody et al., 2018; Xu et al., 2017; Fortmann and Johnson 1984). Fine and ultrafine insoluble particles, which often become embedded in leaf microstructures, are most likely to be retained despite precipitation (Xu et al., 2024; Weerakkody et al., 2018; Przybysz et al., 2014). Observations suggest precipitation washoff is governed more by the cumulative precipitation amount rather than precipitation intensity or precipitation pH (Xu et al., 2017; Fortmann and Johnson 1984), although extremely intense rainfall can still mechanically dislodge PM (Zhang et al., 2019). On the scale of an individual tree, removal efficiency tends to be lowest near the inner crown, where less rainfall reaches the foliage (Ja Kwak et al., 2023).

1.6 Foliage Surface Water

Formatted: Heading 2, Indent: First line: 0 cm

As noted earlier, the deposition of PM (i.e., alkaline dusts) and gases may influence the dry deposition characteristics of the forest through a pH feedback effect. However, pH is only defined in aqueous solutions (Pye et al., 2020), requiring the presence of water on leaf surfaces to estimate surface pH. This water may exist as small droplets or thin water layers, forming aqueous reservoirs for gas dissolution. The likelihood of water condensation and hence the formation of foliage water droplets or layers is increased in the presence of leaf hairs (Konrad et al. 2015). Meteorological conditions can directly encourage the development of water droplets or thin water layers on foliage, either through precipitation or the development of dew, fog, or guttation. Guttation is the process where water droplets form and appear at the edges or tips of healthy leaves, occurring mainly because of pressure generated in the roots. The roots absorb water from the soil due to differences in ion concentrations (osmosis) between soil water and the root cells. Living cells in the roots actively help push this water (along with dissolved minerals) up through special tubes called xylem; this pressure builds up forcing the water out through small pores at the leaf edges (Singh, 2016).

In addition to direct sources of water, hygroscopic particulate matter can deliquesce as it interacts with a combination of atmospheric water vapor and transpired water from the leaf stomata (Tredenick et al., 2022; Coopman 2021; Katata and Held 2021; Burkhardt et al., 2001; Burkhardt et al. 1999; Eiden et al., 1994), as might be expected from the related chemical thermodynamics of salts found in PM (Miller et al., 2024). The presence of hygroscopic material can reduce the surface tension of the resulting

droplet (El Haber et al. 2024; Dutcher et al. 2010), promoting a likelihood of initially isolated droplets spreading into a thin water layer. Further spreading (even over a hydrophobic surface) can be achieved if the deliquesced PM is able to act as a surfactant (e.g. Rafai et al., 2002). Thus, the general result of hygroscopic aerosol deposition on plant foliage is the potential development of a thin (microscopic) water layer that can become quite concentrated (i.e., high ionic strength), as implied in studies from the observations of changes in electrical conductance in relation to relative humidity and the spreading behaviour of artificial salt deposits on leaf surfaces (Burkhardt and Eiden 1990; Burkhardt et al., 2012). These water layers may make a connection with the substomatal cavity of the leaf, forming a 'wick' that maintains the water layer even in hot and sunny meteorological conditions (Burkhardt, 2010; Burkhardt et al., 2009; Burkhardt 1995). Furthermore, if the canopy is thick and the wind is weak, a substantial mass transfer barrier due to the leaf boundary layer may be present. This leaf boundary layer acts to limit moisture exchange near the leaf surface with the ambient atmosphere, keeping the relative humidity higher, and increasing the likely presence of thin water layers on the foliage (Burkhardt et al., 2001; Boulard et al, 2002). It is worth noting, however, whether this aqueous solution takes the form of droplets or a thin layer is not necessarily essential for determining the gas uptake rates. In a study of modelling dew chemistry for reactive uptake of gases (including SO_2) from ambient air, Chameides (1987) noted that only minor quantitative differences were obtained in the simulated results regardless of whether the same volume of dew water was assumed to exist as droplets or a thin layer covering the leaf surface.

1.7 Overview of the Current Analysis

Formatted: Heading 2, Indent: First line: 0 cm

The work described herein investigates how the emission of large quantities of base cations from atmospheric dust impacts the pH of foliage water layers in the forests downwind of the source, and how this, in turn, modulates $V_{d_{SO_2}}$. While our air-quality model domain is focused on dust emissions from a major anthropogenic source in the AOSR, the co-deposition effects explored here are also applicable to other sources of particulate base cations, both anthropogenic (i.e., cement production) and natural (i.e., wind-blown topsoil and desert dust). Long-range transported dust, such as Saharan and Asian dust, often contains large fractions of $CaCO_3$ (> 25 %) and $CaSO_4$ (Scheuvens et al., 2013; Wang et al., 2005), and has been shown to influence forest biogeochemistry through base cation deposition (Avila et al., 1998; Rosas et al., 2025). These examples illustrate that the pH-mediated modulation of SO_2 deposition via co-deposited alkaline particles may have a broader global relevance, beyond the AOSR.

The pH-modulation of $V_{d_{SO_2}}$ results from a pH-driven term in the leaf cuticle resistance formula of the dry deposition algorithm (see Sect. 3), which is parameterized based on the effective Henry's law constant for SO_2 ($H^*_{SO_2}$). Hayden et al. (2021), using box modelling and a Monte-Carlo approach, hypothesized that alkaline foliage conditions in the AOSR could substantially increase $V_{d_{SO_2}}$ by reducing the leaf cuticle resistance via this $H^*_{SO_2}$ dependence. We test this hypothesis ~~using a~~through the development of a mechanistic foliage pH model that includes a thin water layer representation, embedded within the GEM-MACH regional chemical transport model. We find that the pH effect is sufficiently strong to account for the large observed SO_2 deposition velocities in this region, ~~and~~ that including the co-deposition effect significantly improves model performance, supporting the hypothesis of Hayden et al. (2021), and that local changes in SO_2 concentrations due to this effect can be on the order of a factor of two.~~.~~

Formatted: Subscript

The following methodology sections begins by describing the original deposition flux components used in GEM-MACH, starting with gaseous dry deposition, including how it may be influenced by the leaf surface pH, followed by particle dry deposition. We explain how the net deposition flux to leaf surfaces is calculated, and how this information is used to estimate the leaf surface pH, thereby introducing a feedback mechanism that modulates gas-phase deposition velocities and fluxes of soluble species. We then present results showing the predicted foliage pH and how the pH-dependent leaf cuticle resistance parametrization impacts

$V_{d_{SO_2}}$ and the SO_2 dry deposition flux. These results are evaluated against both surface monitoring and aircraft observations in the AOSR to assess model performance improvements. Finally, we discuss potential uncertainties and confounding factors, including precipitation-driven removal of deposited mass. The impact of the pH-modulation mechanism is demonstrated through a comparison with a Base Case assuming a fixed, near-neutral foliage pH of 6.68 (Makar et al., 2018).

2 The GEM-MACH model and model evaluation

2.1 Overview of GEM-MACH

The simulations reported herein were generated using a research version of the 3D deterministic Global Environmental Multiscale – Modelling Air-quality and CHemistry (GEM-MACH) numerical air-quality model (Makar et al., 2018; Moran et al., 2010, 2018). The underlying meteorological model is version 5.1.2 of the Global Environmental Multiscale (GEM) weather forecast model (Cote et al., 1998a, b; Caron et al., 2015; Milbrandt et al., 2016). Updates to the chemistry module (MACH) since Makar et al., (2018) include new or updated processes representations for aerosol speciation, biogenic volatilie organic compounds and nitrogen oxide emissions, cloud processing of gases and aerosols, gas-phase chemistry, forest fire smoke emissions, inorganic heterogeneous chemistry, major point source plume rise, NO_2 reactions on particle surfaces, particle and gas dry deposition, secondary organic aerosol formation and vehicle-induced turbulence (Makar et al., 2025 and references therein). In this study, we used GEM-MACH in a nested configuration, with an outer domain covering North American at a resolution of 0.09º (i.e., ~10 km grid cell size). The rotated inner domain has a resolution of 0.0225º (i.e., ~2.5 km grid cell size) and covers the entire Canadian provinces of Alberta and Saskatchewan as well as sections of British Columba, Manitoba, Northwest Territories, and the northwestern contiguous United States. The chemistry module is "fully coupled" to the meteorological model – this means that atmospheric aerosols can modulate the predicted meteorology through radiative transfer and cloud microphysics effects (Makar et al., 2015a, b; Gong et al., 2015; Makar et al., 2021). Simulations were carried out for May through August 2018, with a two-week spin-up period in April. The deposition algorithms are described in detail in Section 3 and the Supplement~~2.3~~.

2.2 Model evaluation

To assess the performance of the pH-modulated dry deposition algorithm an evaluation is performed against two main sources of data: (1) the literature-reported values of $V_{d_{SO_2}}$ from Hayden et al., (2021) and Gordon et al., (2023) made in the vicinity of the AOSR and (2) the Wood Buffalo environmental Association (WBEA) continuous monitoring station data that reported nearly continuous hourly observations of SO_2 during the period investigated in this work. The geographic locations of the 21 WBEA stations are shown in Fig. 1. SO_2 measurements made at a single point at a WBEA monitoring station may not necessarily be representative of the predicted grid cell mean because GEM-MACH model predictions of SO_2 are representative of the 20 m level of an entire grid cell which has area of ~6.25 km^2 (~2.5 x 2.5km grid cell size).

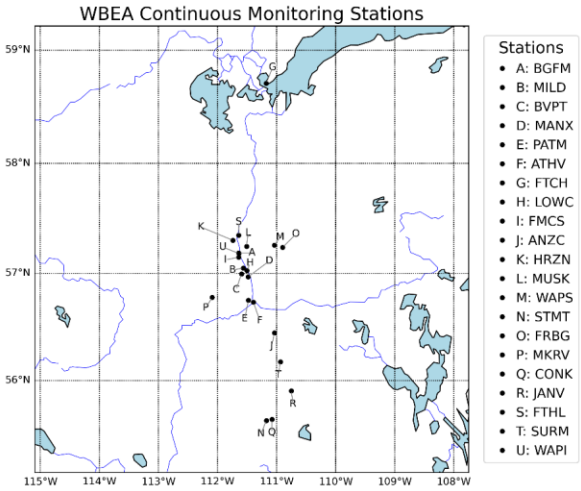

Figure 1: 21 Wood Buffalo Environmental Association (WBEA) continuous monitoring stations with observations available during the period investigated in this work. These stations reported hourly (nearly continuous) observations of SO_2 in ppbv during this period.

3 Dry deposition algorithms

The dry deposition velocity (m s^{-1}) in GEM-MACH follows a 'resistance model' approach (Erisman et al., 1994; Wyers et al., 1994; Wesely, 1989; Baldocchi et al 1987; Fowler 1978; Wesley and Hicks, 1977; Garland, 1977), where the total deposition velocity for a grid cell is a land-use-fraction weighted sum, calculated as

$$V_{d_{gas}} = \sum_{i=1}^{nlus} (v_{d_i} \times f_i), \tag{1a}$$

where

$$v_{d_i} = \frac{1}{r_a + r_b + r_c}. \tag{1b}$$

In Eq. (1a), f_i is the fractional land use (0.0 to 1.0) of land use type i (with a total of $nlus$ land use categories). r_a is the gas-independent aerodynamic resistance between height z_r and the surface, r_b is the quasi-laminar sublayer resistance and r_c is the bulk surface resistance. The aerodynamic resistance depends on meteorological and land surface characteristics, while the r_b and r_c terms also depend on the gas being deposited. All resistance 'r' terms have units of s m^{-1}. In GEM-MACH, the parametrization described in Wesely (1989) is used to calculate the bulk surface resistance r_c ~~as~~

$$r_c = \frac{1}{\frac{1-W_{st}}{r_s + r_m} + \frac{1}{r_{cut_{zha}} + r_{cut}} + \frac{1}{r_{conv} + r_{exp}} + \frac{1}{r_{ac} + r_g}}, \tag{2}$$

where r_m is the mesophyll resistance, r_s is the stomatal resistance with $W_{st} = 0$ for no stomatal blockage and $W_{st} = 0.5$ to account for the partial blockage of the stomata by water during precipitation and at high ambient relative humidity. r_{cut} is the leaf cuticular resistance, r_{conv} is the resistance of gas-phase transfer due to buoyant convection, r_{exp} is the resistance of leaves, twigs, bark and other exposed surfaces in the lower canopy (including buildings), r_{ac} is the in-canopy aerodynamic resistance (which depends on the canopy height and the canopy density) and r_g is the ground (soil) resistance. Details of the terms in the deposition algorithm

are provided in the Supplement, Appendix A. Three terms however include a dependence on the surface concentration of the hydrogen ion, through effective Henry's Law constants: r_m, r_{cut}, and r_{exp}. The formulae for these terms ~~terms~~ are, respectively (Makar et al., 2018; Clifton et al., 2023),

$$r_m = \frac{1}{\mathrm{LAI}\left(\frac{H^*_{sp}}{3000} + 100 x_{0_{sp}}\right)}, \quad (3)$$

~~$r_s = \frac{r_{s_{min}}}{k_s(Q_p) k_s(\mathrm{VPD}) k_s(T) k_{sc} \mathrm{LAI}} \frac{D_{H_2O}}{D_{sp}}$, (4)~~

$$r_{cut_{zha}} = \frac{r_{cut_0}}{\frac{H^*_{sp}}{10^5} + x_{0_{sp}}} \quad ~~r_{cut} = \frac{r_{cut_0}}{\mathrm{LAI}\left(\frac{H^*_{sp}}{10^5} + x_{0_{sp}}\right)}~~, \quad (4)$$

and

~~$r_{conv} = 100\left(1 + \frac{1000}{Q_p + 10}\right)$, (6)~~

$$r_{exp} = \frac{1}{\frac{H^*_{sp}}{10^5 r_{exp,SO_2}} + \frac{x_{0_{sp}}}{r_{exp,O_3}}}, \quad (5)$$

~~and~~

~~$r_g = \frac{1}{\frac{\epsilon}{r_{g,SO_2}} + \frac{p}{r_{g,O_3}}}$. (8)~~

In these formulae, LAI is the single-sided leaf area index (m^2 leaf area per m^2 ground area), and the relative surface reactivity term $x_{0_{sp}}$ has been parameterized using half-redox potentials outlined in Zhang et al., (2002). H^*_{sp} is the species (sp) – dependent effective Henry's law constant, and r_{exp,SO_2} and r_{exp,O_3} are parameterized resistances which depend on the land use type.~~), and the relative surface reactivity term x_0 has been parameterized using half-redox potentials outlined in Zhang et al., (2002). Note that the LAI term in Eq. (3) was inadvertently left out of the corresponding formula in Makar et al., (2018) but has been corrected in subsequent work and herein. In Eq. (4), $r_{s_{min}}$ is the minimum stomatal resistance. $k_s(Q_p)$, $k_s(\mathrm{VPD})$, $k_s(T)$ and k_{sc} are correction factors (unitless, ranging between 0 and 1) for solar irradiance, the ambient vapor pressure deficit, the air temperature and the atmospheric CO_2 concentration respectively. $\frac{D_{H_2O}}{D_{sp}}$ is the ratio of the molecular diffusivity of water vapor in air to that of the gas species of interest. The equations describing the correction factors for r_s and $\frac{D_{H_2O}}{D_{sp}}$ can be found in the supplement of Makar et al., (2018). In Eq. (5), r_e^* is a constant land-use-specific cuticular resistance for SO_2. In Eq. (6), Q_p is the solar irradiance incident at the top of the canopy ($W\ m^{-2}$). In Eq. (7) and (8), r_{exp,SO_2}, r_{exp,O_3}, r_{g,SO_2} and r_{g,O_3} are constant land-use and season specific reference resistances for SO_2 and O_3, with values given in the supplement of Makar et al., (2018).

Wesely's formulations for the cuticle, mesophyll, lower canopy and ground surface resistances all incorporate "parallel" resistance pathways for the removal of gases at each of these depositing surfaces via two chemical processes: (1) dissolution of soluble species ~~(making use of a chemical species-dependent effective Henry's law constant, H^*_{sp})~~, and (2) reactive destruction at the surface (making use of a chemical species-dependent parameter x_0). Wesely (1989) recognized that most direct observations of gas deposition fluxes are for the gases SO_2 and O_3 – the former being strongly influenced by the surface dissolution pathway, while the latter by the surface reactive destruction pathway. Hence the cuticle, mesophyll, lower canopy and ground surface resistance terms make use of ratios of the depositing specie's H^*_{sp}~~H^*~~ to that of SO_2, and x_0 is usually expressed to give a relative

Formatted: Left

surface reactivity relative to that of O_3. Thus, in the Wesely formulation of r_c adopted in the GEM-MACH air quality model (Makar et al., 2018), H^*_{sp} is used in the terms describing r_m, $r_{cut_{zha}}$ ~~$r_{\overline{cut}}$~~ and r_{exp} to "scale the rates of uptake by moist and wet surfaces relative to rates for SO_2 uptake" (Wesely, 1989). ~~, while the ground resistance term makes use of a two-parameter pair of parallel resistances for SO_2 and O_3 (Zhang et al., 2002).~~ This scaling relative to SO_2 is the reason for division of H^*_{sp} by 10^5 in the above formulae for $r_{cut_{zha}}$ ~~$r_{\overline{cut}}$~~ and r_{exp}, because for neutral conditions H^*_{sp} for SO_2 ($H^*_{SO_2}$, where $H^*_{SO_2 neutral} = H^*_{SO_2 n}$) $\approx 10^5$ M atm^{-1}; ~~$H^*_{\overline{sp}} \approx 10^5$ M atm^{-1} (referred to as $H^*_{SO_{2\overline{n}}}$ hereafter) and the~~ near-neutral conditions are presumed to be typical of water in plant sap and in the substomatal cavities of the leaves (Wesely, 1989). H^*_{sp} for chemical species which dissociate are usually functions of the concentration of hydrogen ions in the solution.

~~Following a multi-model evaluation of ozone deposition algorithms, in which the above GEM-MACH algorithm was found to have a positive bias in the ozone deposition velocity relative to those inferred from ozone flux measurements (Clifton et al., 2023), a re-evaluation of the theoretical basis of the equations was carried out, and two key errors in the original formulation (Makar et al. 2018) were corrected. Equation (5) as above includes an explicit LAI dependence. However, the reference coefficients $r_{\overline{cut_0}}$ dependant on land-use types and seasons were taken from Zhang et al (2002) wherein the LAI dependence was effectively included in the coefficient formulation. The LAI dependence was thus double counted in Makar et al., (2018) and Clifton et al. (2023), and has been corrected herein with the removal of the explicit LAI term. Thus, Eq. (5) has been removed from the system of equations in the current work and replaced with Eq. (9):~~

~~$$r_{\overline{cut_{zha}}} = \frac{r_{\overline{cut_0}}}{\frac{H^*_{\overline{sp}}}{10^5} + x_{0_{\overline{sp}}}}. \quad (9)$$~~

~~Similarly, the in-canopy canopy aerodynamic resistance ($r_{\overline{ac}}$) term in Makar et al. (2018) and Clifton et al. (2023) was based on Zhang et al. (2003) and only took the reference values ($r_{\overline{ac_0}}$) as a function of season and land use only (i.e., values obtained only from a lookup table, that is, $r_{\overline{ac}} = r_{\overline{ac_0}}$). However, Zhang et al. (2003) had also included $r_{\overline{ac}}$ dependencies on the friction velocity (u^*) and LAI, which was neglected in Makar et al., (2018) and Clifton et al. (2023). In this work, these dependencies have been implemented, resulting in a functional expression for $r_{\overline{ac}}$ as~~

~~$$r_{\overline{ac}} = \frac{r_{\overline{ac_0}} \mathrm{LAI}^{3/4}}{u^{*2}}. \quad (10)$$~~

~~The impact of these updates is examined elsewhere in this special issue (Toyota et al., 2025).~~

~~Values of $H^*_{\overline{sp}}$, x_0, α and β are given in Table 1 for selected gas species. $r_{\overline{ac_0}}$ and $r_{\overline{cut_0}}$ as a function of land use type and season are given in Tables S3 and S6 of Makar et al. (2018). The constant values of $H^*_{\overline{sp}}$ were obtained from Wesley (1989) and Zhang et al., (2002) and are representative of 'neutral conditions' at standard temperature and pressure. x_0, α and β were obtained from the supplement of Makar et al., (2018) and Zhang et al., (2002). In this work, $H^*_{\overline{sp}}$ is allowed to vary with the predicted [H$^+$] concentration in the leaf water solution (see Sect. 2.2) and the air temperature (T with units K).~~ The formulae describing the [H$^+$] dependence on H^* for key~~some~~ gas species are given in Table S1, while other parameters for the deposition velocity calculations are provided in Table S2. H^*_{sp} for dissociating species will have a first or second-order inverse dependence on the hydrogen ion concentration (that is, $H^*_{sp}([\mathrm{H}^+]) \propto [\mathrm{H}^+]^{-1}$ for a single dissociation stage, while species with two levels of dissociation will also have $H^*_{sp}([\mathrm{H}^+]) \propto [\mathrm{H}^+]^{-2}$). Noting that $\mathrm{pH} = -log_{10}[\mathrm{H}^+]$, increases in pH (i.e. decreases in [H$^+$]) will lead to increases in H^*_{sp}, and hence resulting in decreases in the mesophyll, cuticle and lower canopy resistances (equations (3-5)), leading potentially to decreases in the surface resistance r_c (equation (2)) and thus increases in the deposition velocity (equation 1). ~~Effective Henry's~~

Law constants H^*_{sp} are different from the intrinsic Henry's law constants H_{sp} in that they can include the effects of ionic dissociation of the dissolving gas into multiple stages of ions within solution, which may increase the partitioning to the aqueous phase.

Table 1: Values of H^*_{sp} and x_0 for some common gaseous species. Tabulated data for H^*_{sp} are from Wesley (1989) and Zhang et al., (2002). x_0, α and β are from Zhang et al., (2002) and Makar et al., (2018). The formula describing $H^*_{SO_2}$ and $H^*_{NH_3}$ were obtained from Chameides (1984) and Shi et al., (1999) respectively. The remaining H^* formulae are from Evrens et al. (2003).

Gaseous species (sp)	Chemical formula	H^*_{sp} ($M\ atm^{-1}$) (Wesley, 1989)	H^*_{sp} ($M\ atm^{-1}$)	x_0	α	β
Sulphur dioxide	SO_2	10^5	$H^*_{SO_2} = 1.23\exp\left[3120\left(\frac{1}{T}-\frac{1}{298}\right)\right]\left(1+\frac{K_{eq_1}}{[H^+]}+\frac{K_{eq_1}K_{eq_2}}{[H^+]^2}\right)$, where $K_{eq_1} = 1.7\times10^{-2}\exp\left[2090\left(\frac{1}{T}-\frac{1}{298}\right)\right]$, and $K_{eq_2} = 6\times10^{-8}\exp\left[1120\left(\frac{1}{T}-\frac{1}{298}\right)\right]$	0	1	0
Ozone	O_3	0.01	$H^*_{O_3} = H_{O_3} = 1.42\times10^{-2}\exp\left[2800\left(\frac{1}{T}-\frac{1}{298.15}\right)\right]$	1	0	1
Nitrogen dioxide	NO_2	0.01	$H^*_{NO_2} = H_{NO_2} = 1.0\times10^{-2}$	0.1	0	0.8
Nitric oxide	NO	2×10^{-3}	$H^*_{NO} = H_{NO} = 1.93\times10^{-3}\exp\left[1600\left(\frac{1}{T}-\frac{1}{298.15}\right)\right]$	0	0	0.01
Nitric acid	HNO_3	10^{14}	$H^*_{HNO_3} = 2.1\times10^5\exp\left[8700\left(\frac{1}{T}-\frac{1}{298.15}\right)\right]\left[\frac{1+22\exp\left[1800\left(\frac{1}{T}-\frac{1}{298.15}\right)\right]}{[H^+]}\right]$	0	10	10
Hydrogen peroxide	H_2O_2	10^5	$H^*_{H_2O_2} = H_{H_2O_2} = 1.42\times10^5\exp\left[6300\left(\frac{1}{T}-\frac{1}{298.15}\right)\right]$	1	1	1
Ammonia	NH_3	2×10^4	$H^*_{NH_3} = H_{NH_3}\left(1+\frac{K_{NH_4^+}}{K_w}[H^+]\right)$ $H_{NH_3} = 59.8\exp\left[4200\left(\frac{1}{T}-\frac{1}{298.15}\right)\right]\ [M\ atm^{-1}]$ $K_{NH_4^+} = \exp\left(16.97-\frac{4411.1}{T}-0.044T\right)\ [M]$ $K_w = \exp\left(-23.6+\frac{1550.1}{T}-\frac{1.229\times10^5}{T^2}\right)\ [M^2]$	0	1	0
Nitrous acid	HONO	10^5	$H^*_{HONO} = 48.6\exp\left[4800\left(\frac{1}{T}-\frac{1}{298.15}\right)\right]\left[\frac{1+5.3\times10^{-4}\exp\left[-1760\left(\frac{1}{T}-\frac{1}{298.15}\right)\right]}{[H^+]}\right]$	0.1	2	2

A key point of the work described herein is that past work such as Wesely (1989) and many subsequent models use a constant value of H^*_{sp} or its equivalent metric, usually taken to represent a 'neutral' solution at the surface of the different vegetation components as described in the earlier equations. In contrast, some chemical transport models employed an approach to use 'climatological' soil pH categories indicated from geophysical data as the basis for changing the reference values of r_{g,SO_2} spatially across the land surface (Ganzeveld et al., 1998; Kerkweg et al., 2006). However, the leaf surface pH may be perturbed quite dynamically by the recent deposition history of all depositing species, implying potentially higher or lower deposition conductances or net deposition velocities than predicted by assuming neutral conditions. To obtain H^*_{sp} for SO_2 $H^*_{SO_{2n}} = H^*_{SO_{2n}}$ ($= 10^5$ M atm^{-1}) as used in Wesely (1989) and Zhang et al. (2002), the solution pH of the surface must be 6.59, (i.e., $[H^+] = 2.57\times10^{-7}$ M,) using the formula in Table S1) at a standard ambient temperature of 298 K. In this case, when $H^*_{SO_2} > H^*_{SO_{2n}}$ (i.e., pH > 6.59) the impact of the $\frac{H^*_{sp}}{10^5}$ term is to reduce the cuticular resistance ($r_{cut_{zha}}$ r_{cut}), thereby decreasing the bulk surface resistance (r_c) and increasing the deposition velocity of SO_2 ($V_{d_{SO_2}}$). The converse is true when $H^*_{SO_2} < H^*_{SO_{2n}}$ (pH < 6.59) with an increase in r_c and hence a

Formatted: Indent: First line: 1.27 cm

Formatted: Subscript

decrease in $V_{d_{SO_2}}$. Thus, by allowing H^*_{sp} to vary with surface pH rather than assuming a neutral value, we see from the formulae of Table S1 that solution pH (i.e., within a water layer on a leaf surface) can directly impact the deposition of soluble gas species which dissociate or hydrate upon dissolution to give off H^+, such as SO_2, HNO_3, HONO and NH_3. The linear dependence of the reactive gas uptake rate on H^*_{sp} was demonstrated in a formulation of multiphase chemical interactions between air and leaf-surface dew water by Chameides (1987, see their Eqs. (14), (15), and (18)) for a highly conceptual process-oriented study, where additional factors such as the chemical loss rate for depositing compounds within the dew, the total volume of dew water and its growth or shrinkage rate were also shown to control the gas uptake kinetics. Non-linearity in how these additional factors synergistically contribute to the rate of the gas uptake, hence the conductance for the gas deposition on the leaf surface, etc., is missing in the resistance formulations such as for $r_{cut_{zha}}$ ~~r_{cut}~~ in Eq. (45) despite allowance being made for the serial addition of the chemical reactivity term ($x_{0_{sp}}$) and will be a subject of our potential future studies.

The 'solution pH effect' is demonstrated for SO_2 in Fig. 2, for the GEM-MACH "evergreen needleleaf forest" land use category in mid-summer, using an LAI = 3.5, u_* = 0.6 m s^{-1}, a Monin–Obukhov length L = 250 m, Q_p = 450 W m^{-2}, T = 22ºC, RH = 62 % and [CO_2] = 425 ppm. These values are representative of mid-summer AOSR conditions (Hayden et al. 2021). Immediately obvious from Fig. 2 is the rapid variation in V_d with a unit change in the foliage pH; an increase in the pH from 7.0 to 8.0 increases V_d from about 1.0 cm s^{-1} to 2.4 cm s^{-1}, an increase of 140 % or a factor of 2.4x. The pH impact on $r_{cut_{zha}}$ ~~$_{cut}$~~ (and hence V_d) is largely confined to the range between pH = 5.0 and pH = 9.0. Below pH = 5.0 and above pH = 9.0, r_c reaches an asymptote, regardless of whether $r_{cut_{zha}}$ ~~r_{cut}~~ is further increased or decreased respectively. Hence in this study, $r_{cut_{zha}}$ ~~r_{cut}~~ is bounded within the range between 0.01 and 99999.9 s m^{-1}; for comparison this lower limit of 0.01 s m^{-1} for $r_{cut_{zha}}$ ~~r_{cut}~~ is 2000 times smaller than the lower limit of 20 s m^{-1} suggested by Zhang et al. (2002) (see Sect. ~~5.2~~5.2).

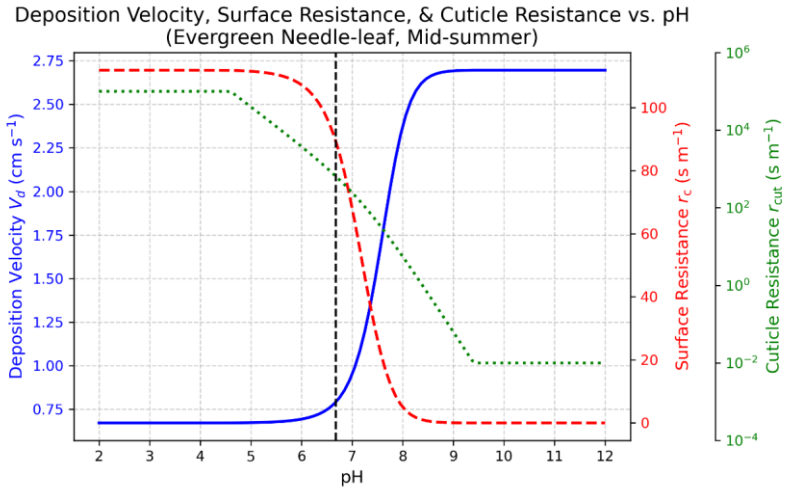

Figure 2: The variation in the deposition velocity ($\boldsymbol{V_d}$, cm s^{-1}), bulk surface resistance ($\boldsymbol{r_c}$, s m^{-1}) and the cuticular resistance ($\boldsymbol{r_{cut}}$, s m^{-1}) of SO_2 as a function of foliage pH, calculated using the equation for $\boldsymbol{H^*_{SO_2}}$ given in Table 1. The land use type was selected as an evergreen needleleaf forest in mid-summer, with an LAI = 3.5, $\boldsymbol{u_*}$ = 0.6 m s^{-1}, $\boldsymbol{L}$ = 250 m, $\boldsymbol{Q_p}$ = 450 W m^{-2}, $\boldsymbol{T}$ = 22ºC, $\boldsymbol{RH}$ = 62 % and [CO_2] = 425 ppm, representative of the AOSR during this time of year (Hayden et al. 2021). The black dashed line indicates a pH = 6.68, which is the current "near-neutral" pH assumed in GEM-MACH calculations of $\boldsymbol{H^*_{SO_2}}$.

4 Simulating foliage pH: Modifications to the dry deposition algorithm

Several considerations must be addressed in order to carry out the calculation of foliage pH for the purposes of deposition velocity estimation, in addition to incorporating the dependence of V_d on $[H^+]$, as described in Sect. 3. Choices must be made regarding which foliage types should be subject to pH-dependent deposition. The accumulation of previously deposited material must be tracked across time steps (since this will determine the pH of the foliage surface in the current time step). This tracking must include both deposition fluxes to the foliage and the removal of deposited material via precipitation (washoff). The amount of liquid water adhering to leaf surfaces must also be estimated, from both meteorological and thermodynamic sources. The pH calculation must take into account high-concentration thermodynamic chemistry, since the water amounts can be sufficiently small that non-ideal solution chemistry solvers must be employed. The formula representing deposition must make use of the resulting pH values, and account for varying types of foliage within each model grid cell; the extent to which deposition specifically to the foliage portion of the surface is resolved may depend on the algorithm (for example, the gas and particle deposition algorithms may differ in this respect). These aspects of the simulation of foliage pH are discussed in Sections 4.1 through 4.5. Note that none of the pH calculations are employed in the Base Case simulations, which use the default pH value of 6.68.

4.1 Restricting the pH dependence to "Natural Vegetation"

Formatted: Heading 2

In the GEM-MACH model, the deposition of a gaseous species to foliage has two main pathways: (1) to the leaf surface (leaf cuticle) and (2) to the leaf interior (trans-cuticular and stomatal deposition). The relative importance of the different pathways may depend on both the vegetation type and the identity of the gas. In this investigation, the fraction of gaseous deposition that occurs to the leaf surface in a grid cell is estimated via effective conductances for each land-use type containing 'natural vegetation'. While GEM-MACH has 15 unique land-use types for dry deposition modelling, only 4 of these are considered in our high resolution foliage pH co-deposition simulations, including: (1) evergreen needleleaf forests, (2) deciduous broadleaf forests, (3) mixed forests and (4) dwarf trees and shrubs (Fig. 3). Vegetation classes containing grassland or crops were not considered since these types of vegetation may have non-trivial anthropogenic interventions at the leaf foliage level (i.e., fertilizer application, harvesting, pruning), thus generating a large uncertainty in the deposition accumulators, and as a result, the predicted foliage pH. In all cases, deposition accumulation (and pH calculation) is only considered for forest canopies with canopy heights $h_c > 1$ m, but in almost all cases h_c is well above this limiting value for the selected vegetation classes.

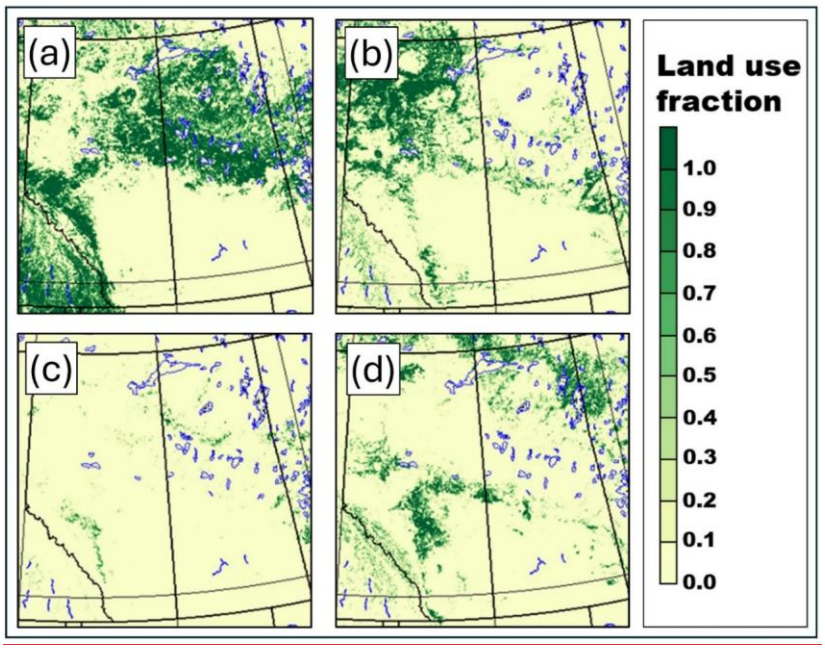

Figure 3: Land use fractions (0.0 – 1.0) for vegetation classes in GEM-MACH simulations: (a) evergreen needleleaf forests, (b) deciduous broadleaf trees, (c) mixed wood forests and (d) dwarf trees, shrubs with ground cover. While GEM-MACH contains classes for evergreen broadleaf and deciduous needleleaf forests, the land-use fraction for these categories is 0.0 in the entire geographic domain investigated here.

Formatted: Normal

~~4.1 Accumulating deposited species on foliage: gases~~

Formatted: Heading 2

~~In the GEM-MACH model, the deposition of a gaseous species to foliage has two main pathways: (1) to the leaf surface (leaf cuticle) and (2) to the leaf interior (trans-cuticular and stomatal deposition). The relative importance of the different pathways may depend on both the vegetation type and the identity of the gas. In this investigation, the fraction of gaseous deposition that occurs to the leaf surface in a grid cell is estimated via effective conductances for each land-use type containing 'natural vegetation'. While GEM-MACH has 15 unique land-use types for dry deposition modelling, only 6 of these are considered in our foliage pH simulations, including: (1) evergreen needleleaf forests, (2) evergreen broadleaf forests, (3) deciduous broadleaf forests, (4) deciduous needleleaf forests, (5) mixed forests and (6) dwarf trees and shrubs. While these six categories are handled in the dry deposition parametrization of GEM-MACH, the deciduous needleleaf forests and evergreen broadleaf forests categories are not present in the default land-use database used for the 2.5km resolution inner model domain used in this study . The fractions of the remaining four vegetation classes in model grid cells are shown in Fig. 3. Vegetation classes containing grassland or crops are not considered since these types of vegetation may have non-trivial anthropogenic interventions at the leaf foliage level (i.e., fertilizer application, harvesting, pruning), thus generating a large uncertainty in the deposition accumulators, and as a result, the predicted foliage pH. In all cases,~~

~~deposition accumulation (and pH calculation) is only considered for forest canopies with canopy heights h_c > 1 m, but in almost all cases h_c is well above this limiting value for the selected vegetation classes.~~

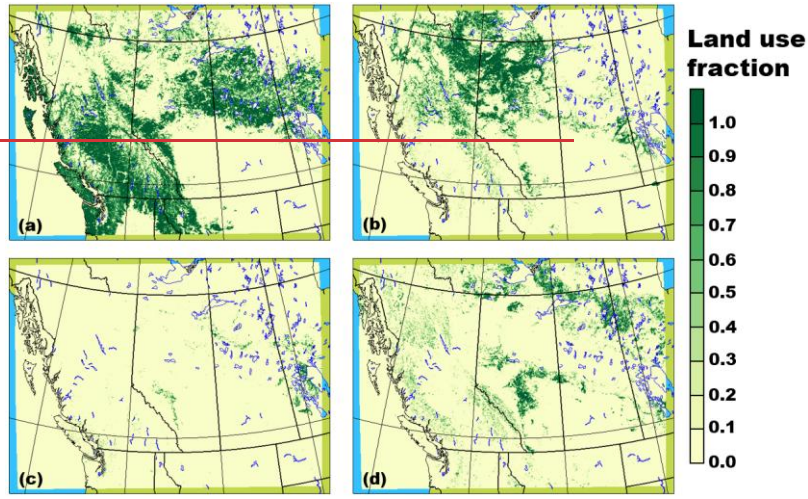

~~Figure 3: Land use fractions (0.0 – 1.0) for vegetation classes in GEM-MACH simulations: (a) evergreen needleleaf forests, (b) deciduous broadleaf trees, (c) mixed wood forests and (d) dwarf trees, shrubs with ground cover. While GEM-MACH contains classes for evergreen broadleaf and deciduous needleleaf forests, the land-use fraction for these categories is 0.0 in the entire geographic domain investigated here.~~

4.2 Comparison of resistances: cuticle resistance as the main pathway for pH dependence

The cuticle resistance pathway is the only pathway present in the Wesely parameterization wherein an H^* dependent term critically controls the entire pathway's contribution to the deposition flux. For example, the mesophyll pathway, which also includes an H^* dependence, is already characterized by a very low resistance for the mesophyll portion, consistent with observations that show the stomatal resistance is ~~the~~ the dominant barrier to SO_2 assimilation (Pfraz et al. 1987). The mesophyll resistance is added in series to the stomatal resistance, and the latter lacks an H^* dependence. The net deposition flux via the overall stomatal pathway is determined largely by the stomatal resistance itself, and consequently the influence of H^*on the combined pathway is likely to be small. Furthermore, the mesophyll pH, representative of the apoplastic fluid within the leaf, remains relatively constant at a neutral to slightly acidic pH, making the use of a constant H^* in this term more appropriate (Yu et al., 2000; Savchenko et al., 2000). For the soil pathway, the r_{ac} term adds in series with the r_g term, the former of which is not dependent on H^* in the above formulation. Since typically $r_{ac} \gg r_g$ for the forest categories of the land-use type, the H^* term has a minor influence on the soil pathway. The lower canopy (r_{exp}) term's H^* dependence, coupled with the low value of r_{conv}, implies it may be a candidate pathway for an H^* dependence. However, the relatively high values of the r_{exp,SO_2}, and r_{exp,O_3} coefficients ensure that this overall pathway has relatively little mass flux (and is often left out of deposition algorithms altogether). In contrast, the cuticle pathway's H^* dependence is capable of controlling (and greatly reducing) the cuticle resistance without interferences from

Formatted: Heading 2, Left, Don't keep with next

Formatted: Normal

Formatted: English (United Kingdom)

Formatted: Heading 3, Indent: First line: 0 cm

Formatted: Indent: First line: 1.27 cm

additional resistances acting directly within this pathway and hence may have a significant impact on the resulting deposition velocity. We therefore focus specifically on the pH influence on the cuticle pathway, in our work that follows.

4.3 Accumulation of Deposition Fluxes

From the above development, a requirement for calculating cuticle surface pH is the need to track and accumulate the past history of that portion of the deposition flux which ends up on the cuticles of natural vegetation foliage. This calculation is specific to the deposition algorithm employed: equations (6, 7 and 8), below, and their theoretical development in the Supplement (Appendix B and Appendix C), are specific to GEM-MACH's deposition algorithms, but the methodology employed is generalizable to any deposition algorithm.

4.3.1 Accumulating the flux of gases to cuticle surfaces

The potential impact of changes to the H^* value associated with gaseous deposition via the cuticle pathway requires that an estimate be made of the deposition flux via that pathway. This was done by using the concept of effective fluxes (Galmarini et al., 2021). Appendix B (Supplement) describes the development of the terms for the portion of the deposition flux which is associated with both the cuticle resistance and the natural vegetation types as per Figure 3. Note that the formulae are specific to the gas deposition algorithm used in GEM-MACH, but the same methodology may be applied to other deposition algorithms using the effective conductance formulation specific to that algorithm, as outlined in Appendix B. Here we state the final resulting formulae.

For gases *other than ammonia*, the deposition flux to vegetation cuticles on the leaf surfaces of natural vegetation for the *j*'th gas is given by:

$$F_{cut_j} = \frac{\sum_{i=1}^{nlus}\left[v_{d_{j,i}} \times f_i \times \delta_i \times \left(\frac{\frac{1}{r_{cut_{j,i}}}}{\frac{1-W_{st}}{r_{s_{j,i}}+r_{m_{j,i}}} + \frac{1}{r_{cut_{j,i}}} + \frac{1}{r_{exp_{j,i}}+r_{conv_{j,i}}} + \frac{1}{r_{ac_{j,i}}+r_{g_{j,i}}}} \right) \right]}{\sum_{i=1}^{nlus}(v_{d_{j,i}} \times f_i)} \times F_j \quad (6)$$

Where *j,i* indicates the *j*'th gas and the *i*'th land-use type, f_i is the fractional area comprised of land-use type *i* within a given grid cell, F_j is the total flux, and $\delta_i = 1$ when the land-use type is one in which the pH dependence is to be calculated, and $\delta_i = 0$ otherwise.

Gases with *bidirectional fluxes* such as ammonia (NH_3) require a treatment that depends on the bidirectional flux algorithm employed. In the case of the bidirectional NH_3 flux algorithm employed in GEM-MACH (Zhang et al., 2010), the NH_3 flux through the cuticle pathway is always downward, and depends on vegetation-and-meteorology-dependent canopy compensation point concentration of NH_3 ($x_{c_{NH_3}}$, μg m^{-3}), and on the cuticle resistance $r_{cut_{NH_3}}$ (s m^{-1}); the cuticle flux in $F_{cut_{NH_3}}$ (mol m^{-2}) for a given land use type is given by:

$$F_{cut_{NH_3}} = \frac{x_{c_{NH_3}} \times 10^{-6}}{r_{cut_{NH_3}} \times M_{NH_3}} \times \Delta t \quad (7)$$

Equations (6) and (7) may be used to accumulate the fluxes of gases to cuticle surfaces, for later calculation of the cuticle surface pH. ~~For the Wesely-based (1989) scheme used in GEM-MACH, Eq. (1a) can be separated into two components: (1) V_{d_Y} representing the deposition velocity to land-use categories containing 'natural' vegetation (i.e., Fig. 3) and (2) V_{d_X} representing the deposition velocity to other land-use categories,~~

~~$$V_{d_{gas}} = \sum_{i=1}^{nlus}(v_{d_i} \times f_i) = V_{d_Y} + V_{d_X} = \sum_{i=1}^{nlus}(v_{d_i} \times f_i \times \delta_i) + \sum_{i=1}^{nlus}(v_{d_i} \times f_i \times [1-\delta_i]), \quad (11)$$~~

where δ_i = 1 if the land use category is classified as natural vegetation, and 0 otherwise. V_{d_Y} can be further separated by deposition pathways, with a deposition to the leaf cuticle ($v_{d_{Y-C}}$) and deposition with a pathway to other surfaces ($v_{d_{Y-O}}$) within a given land use type, such that

$$V_{d_Y} = v_{d_{Y-C_i}} + v_{d_{Y-O_i}} = j_{sp_i} v_{d_i} + \left(1 - j_{sp_i}\right) v_{d_i}, \quad (12)$$

where j_{sp} is the land use dependent fraction of the deposition velocity with a pathway to the leaf cuticle (Galmarini et al., 2021),

$$j_{sp} = \frac{\frac{1}{r_{cut}}}{\frac{1-W_{st}}{r_s + r_m} + \frac{1}{r_{cut}} + \frac{1}{r_{exp} + r_{comm}} + \frac{1}{r_{ac} + r_g}}. \quad (13)$$

Returning to Eq. (11) and expanding it to include the terms outlined in Eq. (12), we obtain

$$V_{d_{gas}} = \sum_{i=1}^{nlus} (v_{d_i} \times f_i) = V_{d_{Y-C}} + V_{d_{X-O}} + V_{d_X} = V_{d_{Y-C}} + V_{d_{other}}, \quad (14)$$

which can be rearranged to

$$V_{d_{gas}} = V_{d_{gas}} \alpha_{cut_{gas}} + V_{d_{gas}} \left(1 - \alpha_{cut_{gas}}\right), \quad (15)$$

where

$$\alpha_{cut_{gas}} = \frac{V_{d_{Y-C}}}{V_{d_{gas}}} = \frac{\sum_{i=1}^{nlus} (j_{sp_i} \times v_{d_i} \times f_i \times \delta_i)}{\sum_{i=1}^{nlus} (v_{d_i} \times f_i)} \quad (16)$$

is a value ranging between 0.0 and 1.0 that represents the fraction of the deposition velocity in the grid cell that is (1) being deposited to natural vegetation and (2) is being deposited to the leaf cuticle of this natural vegetation. This allows the natrual cuticular portion of the net deposition over each model timestep to be quantified (mol m^{-2}) as

$$F_{cut_{gas}} = \alpha_{cut_{gas}} \times V_{d_{gas}} \times C_{gas} \times \Delta t = \alpha_{cut_{gas}} \times F_{gas}. \quad (17)$$

Thus, to calculate $F_{cut_{gas}}$ the only additional quantity required to be tracked at each model timestep is $\alpha_{cut_{gas}}$, calculated from Eq. (16). NH_3 must be considered as a special case; in GEM-MACH a bi-directional flux algorithm is applied to NH_3 (Zhang et al., 2010, see Figure S1 for the corresponding deposition resistance diagram), wherein the leaf cuticle is always a sink and hence the calculation $F_{cut_{NH_3}}$ (mol m^{-2}) is calculated as

$$F_{cut_{NH_3}} = V_{d_{cut_{NH_3}}} \times C_{NH_3}^{canopy\_top} \times \Delta t \quad (18)$$

where

$$V_{d_{cut_{NH_3}}} = \frac{1}{r_{cut}} \text{ and} \quad (19)$$

$$C_{NH_3}^{canopy\_top} = \frac{x_{NH_3} \times 10^{-6}}{M_{NH_3}}. \quad (20)$$

~~$V_{d_{cut_{NH_3}}}$ is the dry deposition velocity of NH_3 to the leaf cuticle (m s^{-1}), Δt is the model timestep with units of s, $x_{c_{NH_3}}$ is a vegetation-and-meteorology-dependent canopy compensation point concentration of NH_3 (µg m^{-3}, or the concentration of NH_3 at the canopy top), M_{NH_3} = 17.031 g mol^{-1} is the molecular mass of NH_3 and the 10^{-6} factor is applied to convert from µg to g. In the Zhang et al., (2010) bidirectional NH_3 flux parameterization applied herein, the resulting deposition velocity $V_{d_{cut_{NH_3}}}$ does not depend on H^*. Instead, r_{cut} for NH_3 is determined from Eq. (9) presented in Zhang et al., (2003), where the LAI, relative humidity, and friction velocity (u_*) are used as factors to dynamically adjust a constant value of r_{cut_0} value ascribed to different land use types and to meteorological conditions (i.e., rain vs. dew vs. dry).~~

4.3.22 Accumulating ~~deposited species on foliage: particles~~the flux of particle species to cuticle surfaces

The capture of particulate matter by vegetation is highly dependent on both particle and foliage specific traits. Foliage surface area, pubescence (i.e., leaf hairs) and roughness (i.e., grooves, ridges, folds) can all impact the retention of particles by vegetation, with each trait being highly specific to the vegetation species (see Sect. 1). Regional air quality models cannot resolve these foliage-specific factors, and hence simplified parameterizations are applied to estimate deposition of particles to vegetation. For particulate species, dry deposition in a vegetated area may occur to the plant surface (i.e., leaves, bark) or to the ground. Unlike the algorithm for gases, the deposition algorithm for particles in GEM-MACH does not explicitly separate between these individual pathways but instead employs a parameterized particle-size-dependent 'surface collection efficiency' ($\varepsilon_{i,k}\bar{\epsilon}^{i,k}$) to represent the fraction of particles of size range k that are collected by any canopy and surface elements (leaves, soil, etc.) on the land-use type i. The particle flux specifically to cuticles must be estimated using the available information (Supplement, Appendix C). Here we provide the final result for $F_{cut_{sp}}$, the net flux of particulate species sp to cuticle surfaces for natural vegetation:~~For a particle of median size index k, the deposition velocity in GEM-MACH for land-use type i is calculated as (Zhang et al., 2001; Emmerson et al., 2020)~~

$$F_{cut_{sp}} = \left(\frac{\mathrm{LAI}}{\mathrm{LAI}+1.0}\right) \times \sum_{k=1}^{n_{size}} \left[\left(\frac{\sum_{i=1}^{nlus}\left[\delta_i \times f_i \times v_{d_{i,k}}\right]}{\sum_{i=1}^{nlus}\left[f_i \times v_{d_{i,k}}\right]} \right) \times F_{sp,k} \right] \quad (8)$$

Where f_i, δ_i are defined as for (6) above, LAI is the leaf area index for the grid cell, $v_{d_{i,k}}$ is the deposition velocity of particles of size k for land-use type i, and $F_{sp,k}$ is the total flux of particulate species sp for particle size k.

Equation (8) may be used to accumulate the flux of particulate species to cuticle surfaces, needed for the calculation of cuticle surface pH.

4.3 Removal of mass on foliage surfaces by precipitation

Particles deposited onto the leaf surface can be removed from the foliage surface by precipitation, a process referred to as *washoff*. The precipitation may dissolve solid soluble particles forming an aqueous solution or physically dislodge insoluble particles captured in the grooves or by the hairs of the leaf (Sect. 1). The net result is a reduction in the particle mass on the leaf surface. Experimental investigations into washoff under controlled conditions have shown that the cumulative precipitation amount is the dominant factor determining how much mass is removed from the leaf (Formann and Johnson, 1984; Potter and Ragsdale (1991); Pullman 2009; Xu et al., 2019). Potter and Ragsdale (1991) investigated the removal of SO_4^{2-} and K^+ ions by precipitation from freshly collected broadleaf forest species in North Carolina (*Acer rubrum L., Quercus prinus L., Cornus florida L., and Rhododendron maximum L*) using sequential simulated rainfall events. Their results showed that sulphate removal approached zero after 8 to 11 mm of precipitation, suggesting complete removal of soluble material is possible. Pullman (2009) similarly studied the washoff of applied KNO_3 particles from coniferous needles (*Pinus strobus*, *Taxus cuspidate* and *Tsuga canadensis*) and found that 70 to 90% of deposited mass was removed after 18.5 mm of simulated rainfall. To parameterize the washoff, Pullman (2009) suggested the function

Formatted: Heading 3

Formatted: Font: Italic

Formatted: Font: Italic

Formatted: Font: Italic

Formatted: Font: Italic

Formatted: Font: Italic

$$R(P) = y_0 + ae^{-bP}, \quad (9)$$

where $R(P)$ is the remaining fraction of surface mass after cumulative precipitation P (in mm) and y_0, a and b are observation-based fitted constants. In Pullman (2009), the fitted y_0 value is nonzero, suggesting some residual mass is retained even after extensive precipitation – potentially due to insoluble material or mechanical retention within leaf structures. In this work, we adopt a simplified approach based on the sulphate data reported in Potter and Ragsdale (1991), where it is assumed that all particle species are fully soluble and subject to complete washoff with sufficient precipitation. Accordingly, we set $y_0 = 0$, $a = 1$ and determine $B = 0.189 \pm 0.032$ via least-squares regression of the Potter and Rasdale (1991) sulphate washoff measurements. The least squares regression is shown in Fig. 4 as a dashed line. This simplification assumes that all modelled particulate matter is readily water-soluble, representing a significant source of uncertainty and a likely oversimplification, especially for modelling the washoff of insoluble or the partially soluble part of material deposited on leaf surfaces (see Sect. 5.5 and 6.0). Nonetheless, we believe that it is not a major drawback for this study because our primary purpose is the simulation of pH in the hygroscopic material.

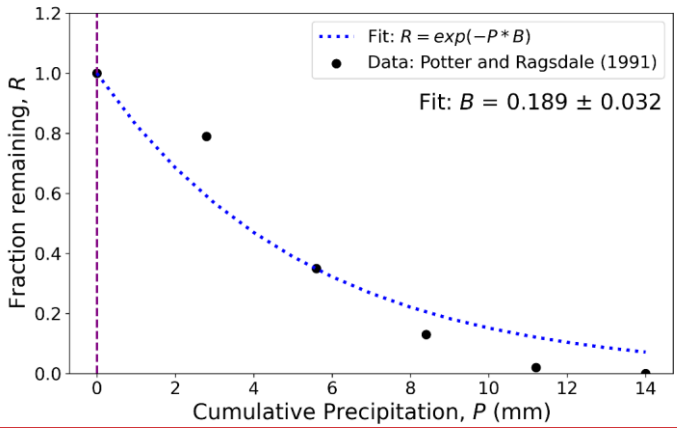

Figure 4: Linear least squares best fit of $\boldsymbol{R = \exp(-P \times B)}$, where $\boldsymbol{R}$ is the fraction of mass remaining on the leaf after $\boldsymbol{P}$ mm of cumulative rainfall. The fitting parameter $\boldsymbol{B}$ is estimated to be 0.189 ± 0.032. Data were obtained by interpolating data presented graphically in Potter and Ragsdale (1991).

Since GEM-MACH is a timestep based model, it is necessary to determine the washoff that would occur over the timestep Δt. For each rainfall event, this requires tracking of (1) the concentration of each species (gas and particle) in the canopy volume at the commencement of the rainfall (M_{init}), and (2) the cumulative precipitation (P) at the current (i) and previous ($i-1$) timestep. Here the cumulative precipitation is tracked per timestep per rainfall event. Over timestep Δt where q mm of rainfall occurs ($P_i = P_{i-1} + q$), the mass of a deposited soluble species removed from the canopy volume after a timestep of precipitation (WO_t) is modelled as

$$WO_t = WO_{t-1}[e^{-bP_{i-1}} - e^{-bP_i}]. \quad (10)$$

It should be noted that dry deposition is not accumulated on the leaf surface during precipitation events, and thus during precipitation events only removal is considered. Furthermore, a lower concentration limit of 1.0×10^{-20} mol m^{-3} is used in the case of complete removal, to avoid division by zero. ~~$v_{\overline{a}}^{i,k} = v_{\overline{s}}^{k} + \frac{1}{r_{\overline{a}}^{i} + r_{\overline{c}}^{i,k}}$ (21)~~

Formatted: Justified

4.4 Estimating Water on Foliage Surfaces: the importance of the lower threshold for layer thickness

An important requirement in calculating cuticle surface pH is an accurate estimate of the amount of water residing on the leaf surface. The quantity of liquid water retained on the leaf, defined here in terms of the leaf water layer thickness, crucially affects the leaf water layer pH (Burkhardt and Eiden 1990; Chameides 1987; Klemm et al., 1987). Chemical thermodynamics solvers such as HETP (see Sect. 4.5.1) predict foliage water that would result from *aerosol deliquescence*, but additional water may be present on the foliage due to meteorological conditions such as rain, dew, fog and leaf guttation (the secretion of plant water from foliage). These additional water inputs were not considered in the original HETP calculations, and if present, neglecting these additional sources of water would result in a bulk leaf water solution that is too concentrated. However, the GEM weather forecast model (upon which the GEM-MACH air-quality model is based) simulates rainfall and dew water intercepted by the canopy in its physical parameterization based on the ISBA (Interactions between Soil, Biosphere and Atmosphere) land surface scheme, providing an estimate of the canopy water content w_r (kg m^{-2} ground area) (Belair et al. 2002), hereafter referred to as 'meteorological water'. We convert this w_r to a bulk canopy-level estimate (kg per m^3 of canopy volume) by dividing by the canopy height as

Formatted: Indent: First line: 0 cm

Formatted: Font: Italic

$$W_{met} = \frac{w_r}{h_c}. \quad (11)$$

In this work, HETP has been modified to accept the meteorological water W_{met} as an input at the start of the thermodynamic calculations used in cuticle surface pH estimation. W_{met} remains constant during the iterative process within HETP to determine [H$^+$] – hence this additional non-aerosol water is allowed to perturb the thermodynamic equilibrium. In addition to W_{met} predicted by the GEM weather model, HETP may increase the total foliage water by an amount determined from aerosol deliquescence (W_{aero}). W_{aero} is not accounted for in W_{met}, since the ISBA parameterization used in GEM does not consider aerosol deliquescence (Belair et al. 2002). Since it is often the case that $W_{met} \gg W_{aero}$, W_{aero} becomes important only during times when $W_{met} \approx 0$. Upon the exit of its process calculations, HETP provides the total foliage water (W_{tot}) with units of kg per m^3 of canopy volume, calculated as the sum of W_{met} (unchanged) and W_{aero}, that is, $W_{tot} = W_{met} + W_{aero}$. W_{tot} is then used in conjunction with [H^+_{air}] (with units of mol m^{-3}) to estimate a bulk foliage pH as

$$\mathrm{pH}_{leaf} = -\log_{10}\left(\frac{[\mathrm{H}^+_{air}]}{W_{tot} \times \frac{1\mathrm{L}}{1\mathrm{kg}}}\right) \quad (12)$$

From W_{tot}, a leaf-level bulk estimate of the water layer thickness (in µm) is calculated[1] as

$$L_w = 1000 W_{tot} h_c / (2\mathrm{LAI}). \quad (13)$$

[1] Note that the 2 in the denominator of Eq. (13) is required to produce an estimate of the water layer that would cover both sides of the entire leaf surface, as opposed to one side (i.e., LAI defines the single-sided leaf area per unit ground area).

Formatted: English (United States)

pH_{leaf} is only calculated if L_w is greater than or equal to a threshold value $L_{w_{Thres}}$. If $L_w \leq L_{w_{Thres}}$, that is, the water layer thickness falls below the threshold value, we assume that pH_{leaf} has a neutral value of 6.68. This threshold on L_w is also physically necessary in that at sufficiently low surface concentrations, water is unlikely to form a contiguous layer.

Previous studies have estimated microscopic water layers on foliage surfaces to typically be in the range of 0.05 µm to 5 µm (Burkhardt and Hunsche, 2013; Van Hove et al., 1989; Sutton et al., 1998), while some studies have suggested the possibility of much thinner water layers, between 1 and 4 nm (Adema and Heeres 1995; Burkhardt and Eiden 1994; Burkhardt and Eiden 1990). To investigate the impact of the choice of the $L_{w_{Thres}}$ on the resulting dry deposition velocities of SO_2, two thresholds were investigated: $5x10^{-4}$ µm and 0.1 μm. We investigated the impact of these alternative values of $L_{w_{Thres}}$ on resulting pH estimates in multi-month simulations on a North American domain (see Fig. S2): the lower threshold resulted in unrealistically extreme pH values, either very acidic (pH < 2) or very basic (pH > 10). The higher threshold also resulted in better performance in comparison with surface SO_2 observations in the relatively dry month of May. In that month, foliage water layers are often sustained only by aerosol deliquescence (W_{aero}), resulting in very high ionic strength. Under these conditions, simulations employing the higher water layer threshold and hence lower ionic strength) had better statistical agreement with observations than those with the lower threshold. Hence in the sections that follow, we employ $L_{w_{Thres}}$= 0.1 μm.

Formatted: Superscript

Formatted: Subscript

where v_{s}^{k} is the size-dependant settling velocity of the particles of median size k, and r_{a}^{i} is the aerodynamic resistance. $r_{c}^{i,k}$ is the canopy resistance for particles of median size k, and is calculated in GEM-MACH as (Zhang et al., 2001; Emerson et al., 2020),

$$r_{c}^{i,k} = \frac{1}{\alpha_{0} u_{*} \varepsilon_{i}^{i,k}} \quad (22)$$

where α_{0} is set to a constant value of 3.0. GEM-MACH resolves size-dependant particle deposition across 12 size bins (index n_{size}). Hence, for each grid cell the fraction of the deposition velocity that is to a natural vegetative land use type for particle size range k is calculated as

$$f_{vk} = \frac{\sum_{i=1}^{nlus} \left[\delta_{i} \times f_{i} \times v_{d}^{i,k} \right]}{\sum_{i=1}^{nlus} \left[f_{i} \times v_{d}^{i,k} \right]} \quad (23)$$

We can then define the flux of a particle species sp within the internally-mixed particle of size k across all vegetation types in a grid cell and its fraction entering the natural land-use types as $F_{sp,k}$ and $\eta_{veg_{vsp}}$ respectively,

$$\eta_{veg_{sp}} = \frac{\sum_{k=1}^{n_{size}} \left(f_{vk} \times F_{sp,k} \right)}{\sum_{k=1}^{n_{size}} \left(F_{sp,k} \right)} = \frac{\sum_{k=1}^{n_{size}} \left(f_{vk} \times F_{sp,k} \right)}{F_{sp}}, \quad (24)$$

where F_{sp} is the total mass flux of the particle species sp across all sizes within the grid cell. Finally, the calculation of the total deposition flux for the particle species sp in the grid cell to the leaf cuticle pathway requires the introduction of the partitioning factor ($\alpha_{cut_{sp}}$) as

$$F_{cut_{sp}} = \alpha_{cut_{sp}} \times \eta_{veg_{sp}} \times F_{sp} \quad (25)$$

$\alpha_{cut_{sp}}$ represents the fraction of $\eta_{veg_{sp}}$ due to deposition to the leaf surface (as opposed to deposition to bark or the ground beneath the canopy), thus $\alpha_{cut_{sp}} \times \eta_{veg_{sp}}$ has an interpretation analogous to $\alpha_{cut_{gas}}$ from Eq. (16). Since our dry deposition paramterization for aerosol particles, namely, Eq. (21), is not built upon attributions of the individual pathways of deposition, $\alpha_{cut_{sp}}$ must be estimated using surrogate information. Here, we have assumed that the total area available for deposition of particles is the sum of the leaf area in the vertical column through the canopy (i.e. the leaf area index, LAI) plus the surface area of the ground below the leaves. A first approximation to $\alpha_{cut_{sp}}$ is thus given by

$$\alpha_{cut_{vsp}} = \frac{LAI}{LAI + 1.0}. \quad (26)$$

Eq. (26) is strictly a function of the LAI but could be modified if additional data became available (for example, the relative amount of surface area available for deposition in the vertical column which is composed of twigs, branches, etc). Any

Formatted: Heading 2
Formatted: Heading 2, Left
Formatted: Heading 2
Formatted: Heading 2, Left
Formatted: Heading 2
Formatted: Heading 2, Left
Formatted: Heading 2
Formatted: Heading 2, Left
Formatted: Heading 2
Formatted: Heading 2, Left
Formatted: Heading 2

~~additional terms added to Eq. (26) would likely appear in the denominator, hence the value of $F_{cut_{sp}}$ calculated using Eq. (26) and Eq. (26) should probably be taken as an upper limiting value.~~

4.~~5~~3 Foliage pH calculations

4.5.1 Initial pH calculation: HETP

The foliage pH is first estimated from the Heterogeneous Vectorized or Parallel (HETP) model of chemical thermodynamics (Miller et al., 2024), using the concentrations of accumulated gases and particles in the canopy volume, and the occurrence of precipitation as inputs, as well as the foliage water predicted by the GEM meteorological model. HETP was selected for this purpose since it includes the computation of activity coefficients in its prediction of pH, which is important for dealing with 'non-ideal' solutions; those with high ionic strength expected to occur under subsaturated humidity conditions on the cuticle surface.

In order to estimate pH, we first convert the accumulation of timestep atmospheric deposition $F_{cut_{gas}}$ and $F_{cut_{sp}}$ subsequent to the last precipitation event at each timestep to a bulk canopy 'concentration' with units of mol per m^3 of canopy volume by dividing by the canopy height h_c (m) as

$$G_{sp_{cut}} = \frac{F_{cut_{gas}}}{h_c} \quad (14\text{~~27a~~}) \tag{14}$$

and

$$P_{sp_{cut}} = \frac{F_{cut_{sp}}}{h_c}. \quad (15\text{~~27b~~}) \tag{15}$$

This simplification assumes that the deposited mass (and predicted foliage water) is evenly distributed over the entire height of the canopy; this allows a calculation of the pH for the canopy to be made a "bulk" calculation, in analogy to the typical application of algorithms such as HETP to particle inorganic chemistry. $G_{sp_{cut}}$ and $P_{sp_{cut}}$ are accumulated over time, referred to hereafter as 'deposition accumulators', and denoted as T_t^{gas} and T_t^{par} at time t. In this study, the removal of mass from foliage surfaces (and a consequent reduction in T_t^{gas} and T_t^{par}) occurs only through the dominant process of precipitation washoff (WO_t^{sp}), although strong winds may also cause removal of particle mass (Sect. 1). Precipitation washoff, given a sufficient amount of precipitation occurring over a sufficient amount of time, is assumed to be complete for the deposited gases ($WO_t^{gas} = T_{t-1}^{gas}$) and particle species ($WO_t^{par} = T_{t-1}^{par}$). Note that washoff by precipitation occurs over time according to Eq. (10~~36~~) ~~(see below)~~. Gases and particles deposited to the leaf are thus assumed to be completely soluble in an excess of water (except for $CaSO_4$, which has relatively low solubility and hence is assumed to remain on the leaf surfaces). In addition, no mass is accumulated on the leaf surfaces during rainfall ($G_{sp_{cut}} = P_{sp_{cut}} = 0$; all depositing mass is assumed to be removed during rainfall events), and as such, a contribution from wet deposition of soluble gases and ions is also ignored in the calculation of foliage pH. Thus, the total bulk concentration residing on the foliage due to dry deposition in a canopy volume at timestep t is simulated for gas species as

$$T_t^{gas} = T_{t-1}^{gas} + G_{sp_{cut}} - WO_t^{gas}, where \begin{cases} WO_t^{gas}, & (Precipitation\ is\ occuring\ at\ time\ t) \\ WO_t^{gas} = 0, & (Otherwise) \end{cases} \quad (16\text{~~28a~~}) \tag{16}$$

and likewise for particle species

$$T_t^{par} = T_{t-1}^{par} + P_{sp_{cut}} - WO_t^{par}, where \begin{cases} WO_t^{par}, & (Precipitation\ is\ occuring\ at\ time\ t) \\ WO_t^{par} = 0, & (Otherwise) \end{cases}. \quad (17\text{~~28b~~}) \tag{17}$$

In our simulation of the foliage pH, only the inorganic soluble gases SO_2, HNO_3, HCl and NH_3 are included for gaseous deposition accumulators, while for particle species, SO_4^{2-}, HSO_4^-, NO_3^-, NH_4^+, Na^+, Cl^-, Ca^{2+}, Mg^{2+} and K^+ are included. These deposition accumulators are then used to calculate the hydrogen ion concentration $[H^+]$ using HETP; note that HETP assumes a unity activity coefficient for H^+. HETP requires as input the total gas + aerosol concentrations (mol m^{-3}) of total sulphate, total nitrate, total ammonia and total chloride. These are defined as, respectively, $TS = SO_2 + HSO_4^- + SO_4^{2-}$, $TN = HNO_3 + NO_3^-$, $TA = NH_3 + NH_4^+$ and $TCl = HCl + Cl^-$. Here, SO_2 is simply assumed to be oxidized to sulphate upon deposition on the leaf surface, which we note is potentially inaccurate as a process description in cases where the S(IV) oxidation is limited by the co-deposition of atmospheric oxidants such as H_2O_2 and O_3 (Chameides, 1987; Wesely et al., 1990), and/or where antioxidants exudated from inside the leaves as speculated for example by Fuentes et al. (1994) are so high as to compete with or dominate over S(IV) in the consumption of oxidants in the leaf-surface aqueous solution. In addition to the above-mentioned inputs, HETP also requires the relative humidity and air temperature. For these simulations, the relative humidity and air temperature are set to the value of the lowest model layer (i.e., screen level). Since these calculations are being done using 'bulk' concentrations, this work does not consider a 'leaf-level' relative humidity or temperature.

~~HETP predicts foliage water that would result from aerosol deliquescence, but additional water may be present on the foliage due to rain, dew, fog and leaf guttation (the secretion of plant water from foliage). These additional water inputs are not considered in the original HETP calculations. If present, neglecting these additional sources of water will result in a bulk leaf water solution that is too concentrated. However, the GEM weather forecast model (upon which the GEM-MACH air-quality model is based) simulates the interception of rainfall and dew water intercepted by the canopy in its physical paramterization based on the ISBA (Interactions between Soil, Biosphere and Atmosphere) land surface scheme, providing an estimate of the canopy water content w_F (kg m^{-2} ground area) (Belair et al. 2002), hereafter referred to as 'meteorological water'. The w_F is converted to a bulk canopy-level estimate (kg per m^3 of canopy volume) by dividing by the canopy height as~~

$$W_{met} = \frac{w_F}{h_c}. \quad (29)$$

~~In this work, HETP has been modified to accept the meteorological water W_{met} as an input at the start of the thermodynamic calculations. W_{met} remains constant during the iterative process within HETP to determines $[H^+]$ — hence this additional non-aerosol water is allowed to perturb the thermodynamic equilibrium. In addition to W_{met} predicted by the GEM weather model, HETP will increase the total foliage water by an amount determined from aerosol deliquescence (W_{aero}). W_{aero} is not accounted for in W_{met} since the ISBA parameterization used in GEM does not consider aerosol deliquescence (Belair et al. 2002). Since it is often the case that $W_{met} \gg W_{aero}$, when W_{met} is not equal to zero, W_{aero} becomes important only during times when $W_{met} \approx 0$. Upon the exit of its process calculations, HETP will provide the total foliage water (W_{tot}) with units of kg per m^3 of canopy volume, calculated as the sum of W_{met} (unchanged) and W_{aero}, that is, $W_{tot} = W_{met} + W_{aero}$. W_{tot} is then used in conjunction with $[H^+_{air}]$ (with units of mol m^{-2}) to estimate a bulk foliage pH as~~

$$\mathrm{pH} = -\log_{10}\left(\frac{[H^+_{air}]}{W_{tot} \times \frac{1L}{1kg}}\right) \quad (30)$$

~~From W_{tot} a leaf-level bulk estimate of the water layer thickness (in μm) is calculated as~~

$$L_w = 1000 W_{tot} h_c / (2\mathrm{LAI}). \quad (31)$$

~~Note that the 2 in the denominator of Eq. (31) is to produce an estimate of the water layer that would cover both sides of the entire leaf surface, as opposed to one side (i.e., LAI defines the single-sided leaf area per unit ground area). In this study, pH_{leaf} is only calculated if $L_w \geq L_{w\,Thres}$. The constraint of using $L_{w\,Thres}$ is placed on the pH_{leaf} calculations to investigate the possibility of very thin water layers being present on the leaf, but also to avoid pH calculations during times with unrealistically thin water layers (that give unrealistically high ionic strength). If $L_w < L_{w\,Thres}$, that is, the water layer thickness falls below the threshold value, we assume that pH_{leaf} has a neutral value of 6.68. This threshold is necessary in that at sufficiently low surface concentrations water is unlikely to form a contiguous layer. To investigate the impact of the choice of the $L_{w\,Thres}$ on the resulting dry deposition velocities of SO_2, two thresholds were investigated. The first test set $L_{w\,Thres}$ = 0.1 μm (i.e. a 100 nm thick water layer if both sides of the leaf are covered), while the second test set $L_{w\,Thres}$ = 0.5 nm (i.e., a length scale of nearly twice the monomolecular layer of water). Previous studies that have estimated microscopic water layers on foliage surfaces to typically be in the range of 0.05 μm to 5 μm (Burkhardt and Hunsche, 2013; Van Hove et al., 1989; Sutton et al., 1998), while some studies have suggested the possibility of much thinner water layers, between 1 and 4 nm (Adema and Heeres 1995; Burkhardt and Eiden 1994; Burkhardt and Eiden 1990). We discuss the impact of the $L_{w\,Thres}$ choice on model results, below.~~

HETP in its original form (Miller et al., 2024) assumes a metastable state in all thermodynamic calculations, therefore the final speciation consists only of aqueous ions and gases (except for $CaSO_4$, which is assumed to be insoluble). Prior to performing thermodynamic calculations, HETP determines the mass of anions and cations that can partition into a set of atmospherically relevant salts. These salts are then assumed to completely deliquesce, forming the initial aqueous phase speciation that is then used to seek the equilibrium state of the chemical system. In this approach HETP does not consider any 'excess' mass of base cations beyond that required for thermodynamic equilibrium. ~~.~~ For example, if the leaf surface contains only sulphate (TS) and potassium (TK), the dominant salt in HETP is assumed to be K_2SO_4. The concentration is determined[2] as $[K_2SO_4] = \min(TS, 0.5TK)$, potentially giving an excess or 'free' amount of potassium as $K_{free} = TK - 2[K_2SO_4]$ in cases where $TS < 0.5K$. This 'free' amount is not used when solving for thermodynamic equilibrium and as a result, does not affect $[H^+]$ (solution pH) predicted by the original HETP. The initial $[H^+]$ calculated by HETP is thus that of the portion of the deposited mass which is in equilibrium with anions, but does not include the influence of any "leftover" (i.e. "free") excess base cation mass. Consequently~~Thus~~, the maximum pH simulated by the original HETP algorithm alone is near 7.5. The focus for algorithms such as HETP is to determine the equilibrium between inorganic gaseous and particulate matter, hence the "excess" mass remains in the particulate phase, since it does not change the particle mass through partitioning. In most cases, this excess mass of base cations is originally balanced by carbonate alkalinity from CO_3^{2-} and/or HCO_3^-, which are prone to titration and the release of gaseous CO_2 promptly via chemical processing of the PM towards its neutralization and acidification in the atmosphere (i.e., Chameides and Stelson 1992; Dentener et al., 1996). This is a process often neglected in HETP and other models of aerosol chemical thermodynamics. However, in cases where a significant amount of excess base cation mass exists *on the leaf surface*, for example downwind of cement processing facilities (Darley, 2012), the pH of the leaf water layer can exceed 7.5, because the amount of excess base cations and carbonate alkalinity is most likely in far excess of that of co-deposition acids. In these cases, the CO_3^{2-} from dissociated salts (such as calcium carbonate $CaCO_3$) may hydrolyse in the leaf water layer to form OH^-, thereby buffering the solution in alkaline conditions. ~~To~~ A

[2] The values of TS and TK are in molar units, and the salt which they may form (K_2SO_4) contains half as many moles of sulphate as potassium. Consequently, the maximum amount of potassium sulphate which may form is the minimum of the sulphate amount and half of the potassium amount.

Formatted: Indent: First line: 1.27 cm

Formatted: Heading 3

Formatted: Font: Italic

Formatted: English (United States)

second adjustment to the initial [H^+] calculated by HETP is therefore required. We investigated t~~investigate how relevant this may be in the GEM-MACH simulations, t~~wo different adjustments ~~were examined for application following the initial [H^+] calculation from the original HETP algorithm~~. The first made use of a simple charge balance, and the second employed high-concentration, non-ideal chemical equilibria (CALCCO3, Sect. 4.5.2). The use of a simple charge balance was found to frequently result in unrealistically high pH values (e.g. greater than 10), and poorly resolved pH in the crucial 7.5 to 9.0 range. The water layers on foliage surfaces are sufficiently thin that calculations consistent with high concentration solution chemistry are therefore required to accurately represent pH (Miller et al., 2023; Fountoukis and Nenes, 2007). We therefore recommend the use of CALCCO3 instead of a simple charge balance for leaf foliage pH calculations, and focus on the use of CALCCO3 hereafter.

Formatted: Heading 3, Indent: First line: 0 cm

~~The first adjustment to account for the effects of free base cation mass subsequent to the application of HETP is a simple charge balance adjustment that uses the ion concentrations predicted by HETP (i.e., aqueous phase output) but also considers the free amount of each base cation species (Ca_{free}, Mg_{free}, K_{free} and Na_{free}) to determine [H+] and hence pH. In this adjustment, referred to hereafter as 'charge-adj', the free base cation mass is assumed to be completely soluble and dissociated in an aqueous solution present on the leaf leading to an excess of OH^-. The charge balance is recalculated as~~

~~$$Na^+ + Na_{free} + 2Ca^+ + 2Ca_{free} + 2Mg^+ + 2Mg_{free} + K^+ + K_{free} + NH_4^+ = 2SO_4^{2-} + HSO_4^- + NO_3^- + Cl^- + OH^- \quad (32a)$$~~

~~so that~~

~~$$OH^- = \left(Na^+ + Na_{free} + 2Ca^+ + 2Ca_{free} + 2Mg^+ + 2Mg_{free} + K^+ + K_{free} + NH_4^+\right) - \left(2SO_4^{2-} + HSO_4^- + NO_3^- + Cl^-\right) \quad (32b)$$~~

~~and~~

~~$$pOH = -\log_{10}\left[\frac{[OH^-]}{W_{tot}\times\frac{1L}{1kg}}\right]. \quad (33)$$~~

~~Using the relationship at 25ºC that $14.0 = pH + pOH$, the water layer pH can be estimated as~~

~~$$pH = \min(14.0 - pOH, 9.0). \quad (34)$$~~

Formatted: Heading 3

~~The charge-adj approach described above is only applied to recalculate the HETP-derived pH when (1) [OH^-] calculated from (32b) is greater than 1×10^{-20} mol m^{-3} and (2) the pH predicted by HETP (when excess base cations are not considered) is greater than 6.68. The upper limit of 9.0 is applied here due to the relationship of Fig. 2 suggesting that higher pH values will not have a significant influence on the cuticle resistance.~~4.5.2 Final pH calculation: Thermodynamic Adjustment (CALCCO3)

~~As an alternative to the charge balance adjustment described above, a second more~~A rigorous thermodynamic adjustment algorithm, ~~called~~ CALCCO3, was developed, which explicitly accounts for equilibrium solution chemistry with ~~additional~~ free a~~ions~~nions associated with carbonate alkalinity, ~~unlike the above~~as a follow-on to the initial HETP calculation ~~adjustment~~. CALCCO3 simulates the water layer pH by including additional thermodynamic equilibria for atmospheric CO_2 and carbonate salts not considered in HETP. In this adjustment any excess of Ca, K, Na or Mg from the initial HETP calculation is assumed to be ~~in~~ matched with carbonate as $CaCO_3$, K_2CO_3, Na_2CO_3 and $MgCO_3$, respectively. The final ~~is adjustment produces an alternative estimate of~~ [H^+] estimate resulting from this adjustment ~~and~~ considers the individual temperature-dependant thermodynamic equilibria with additional considerations for mass balance, solubility constraints and electroneutrality ~~as is outlined in Appendix A~~. The CALCCO3 adjustment is applied to recalculate the initial HETP-derived pH if (1) the free mass of either Ca, Mg, Na or K

remaining after the HETP calculation exceeds 1×10^{-10} mol m^{-3} and (2) the amount of liquid water exceeds 1×10^{-10} kg m^{-3}. Below the limit applied in (1) we assume there is an insufficient mass of base cations yielding a negligible effect on the foliage water pH; below the limit of (2) we assume is insufficient foliage water to generate a water layer with a thickness exceeding L_{wThres}. No consideration has been made for activity coefficients in CALCCO3, unlike the original HETP algorithms. The reaction system solved by the CALCCO3 algorithm, and the theoretical development of the governing equations, are provided in the Supplement, Appendix D.

4.4 Removal of mass on foliage surfaces by precipitation

Particles deposited onto the leaf surface can be removed from the foliage surface by precipitation, a process referred to as *washoff*. The precipitation may dissolve solid soluble particles forming an aqueous solution or physically dislodge insoluble particles captured in the grooves or by the hairs of the leaf (Sect. 1). The net result is a reduction in the particle mass on the leaf surface. Experimental investigations into washoff under controlled conditions have shown that the cumulative precipitation amount is the dominant factor determining how much mass is removed from the leaf (Formann and Johnson, 1984; Potter and Ragsdale (1991); Pullman 2009; Xu et al., 2019). Potter and Ragsdale (1991) investigated the removal of SO_4^{2-} and K^+ ions by precipitation from freshly collected broadleaf forest species in North Carolina (*Acer rubrum L., Quercus prinus L., Cornus florida L., and Rhododendron maximum L*) using sequential simulated rainfall events. Their results showed that sulphate removal approached zero after 8 to 11 mm of precipitation, suggesting complete removal of soluble material is possible. Pullman (2009) similarly studied the washoff of applied KNO_3 particles from coniferous needles (*Pinus strobus*, *Taxus cuspidate* and *Tsuga canadensis*) and found that 70 to 90% of deposited mass was removed after 18.5 mm of simulated rainfall. To parameterize the washoff, Pullman (2009) suggested the function

$$R(P) = y_0 + ae^{-bP}, \quad (35)$$

where $R(P)$ is the remaining fraction of surface mass after cumulative precipitation P (in mm) and y_0, a and b are observation-based fitted constants. In Pullman (2009), the fitted y_0 value is nonzero, suggesting some residual mass is retained even after extensive precipitation – potentially due to insoluble material or mechanical retention within leaf structures. In this work, we adopt a simplified approach based on the sulphate data reported in Potter and Ragsdale (1991), where it is assumed that all particle species are fully soluble and subject to complete washoff with sufficient precipitation. Accordingly, we set $y_0 = 0$, $a = 1$ and determine $B = 0.189 \pm 0.032$ via least-squares regression of the Potter and Rasdale (1991) sulphate washoff measurements. The least squares regression is shown in Fig. 4 as a dashed line. This simplification assumes that all modelled particulate matter is readily water-soluble, representing a significant source of uncertainty and a likely oversimplification, especially for modelling the washoff of insoluble or the partially soluble part of material deposited on leaf surfaces (see Sect. 5.5 and 6.0). Nonetheless, we believe that it is not a major drawback for this study because our primary purpose is the simulation of pH in the hygroscopic material.

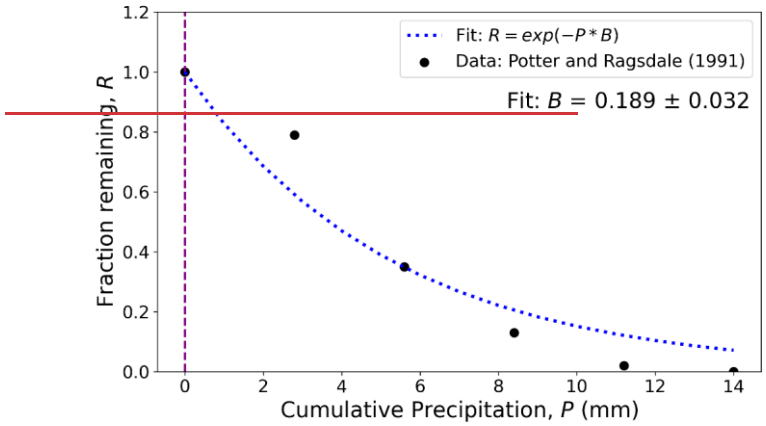

Figure 4: Linear least squares best fit of $\boldsymbol{R = \exp(-P \times B)}$, where $\boldsymbol{R}$ is the fraction of mass remaining on the leaf after $\boldsymbol{P}$ mm of cumulative rainfall. The fitting parameter $\boldsymbol{B}$ is estimated to be 0.189 ± 0.032. Data were obtained by interpolating data presented graphically in Potter and Ragsdale (1991).

Since GEM-MACH is a timestep based model, it is necessary to determine the washoff that would occur over timestep Δt. For each rainfall event, this requires tracking of (1) the concentration of each species (gas and particle) in the canopy volume at the commencement of the rainfall (M_{init}), and (2) the cumulative precipitation (P) at the current (i) and previous ($i-1$) timestep. Here the cumulative precipitation is tracked per timestep per rainfall event. Over timestep Δt where q mm of rainfall occurs ($P_i = P_{i-1} + q$), the mass of a deposited soluble species removed from the canopy volume after a timestep of precipitation (M_{rem}) is modelled as

$$M_{rem} = M_{init}[e^{-bP_{i-1}} - e^{-bP_i}]. \quad (36)$$

It should be noted that dry deposition is not accumulated on the leaf surface during precipitation events, and thus during precipitation events only removal is considered. Furthermore, a lower concentration limit of 1.0×10^{-20} mol m^{-3} is used in the case of complete removal to avoid division by zero. Fig. S2 shows a time series of P and the canopy concentration of PM at a location with the AOSR predicted by GEM-MACH, and the pH predicted by CALCCO3. This figure illustrates how the washoff algorithm applied herein works in our modelling context.

5 Results and Discussion

5.1 Simulation of foliage pH

As discussed in Sect. 2, the predicted foliage pH is a new driving parameter that modulates the dry deposition velocity of SO_2 in this work ($V_{d_{SO_2}}$), specifically by allowing a time-varying $H^*_{SO_2}$ in Eq. 5 and Eq. 7. As demonstrated in Fig. 2, a very small increase in the predicted foliage pH from the current GEM-MACH value of 6.68 can dramatically increase $V_{d_{SO_2}}$, but the pH impact on modulating $V_{d_{SO_2}}$ is most important only for a rather small pH range. For example, increasing the pH above 9.0 has little effect on

further increasing $V_{a_{SO_x}}$ (i.e., as $r_{cut}(SO_x) \rightarrow 0$); likewise decreasing the pH below 5.0 has little effect further decreasing $V_{a_{SO_x}}$ (i.e., as $r_{cut}(SO_x) \rightarrow \infty$). Furthermore, studies have indicated that the quantity of liquid water retained on the leaf, defined here in terms of the leaf water layer thickness, crucially affects the leaf water layer pH (Burkhardt and Eiden 1990; Chameides 1987; Klemm et al., 1987). For example, as the water layer thickness decreases the solution concentrates and the pH may become more acidic (basic) in the case of an initially acidic (basic) chemical solution. However, some question remains regarding the magnitude of the allowed lower limit of the leaf water layer thickness ($L_{w_{Thres}}$) for which pH calculations are carried out and used to modulate $V_{a_{SO_x}}$, with a water layer thickness as thin as 0.001 µm suggested by some previous work (Burkhardt and Eiden 1994; Burkhardt and Eiden 1990). Such microscopically thin leaf water layers may complicate the analysis by producing an extremely concentrated leaf water solution – this is especially true in the case of basic conditions where the pH adjustment CALCCO3 applied herein does not consider activity coefficients.

To investigate the pH modulated effect on $V_{a_{SO_x}}$ and the impact of $L_{w_{Thres}}$, four different simulations were carried out and compared directly against a 'Base Case', for the period May to August 2018. Each simulation calculates the foliage pH according to a slightly different methodology. It should be noted that in all simulations the foliage pH was initially calculated using HETP, before applying any subsequent pH adjustments. The Base Case in this study is the GEM-MACH model simulation using Eq. (1) to (10) but with a foliage pH always set to 6.68. Hence, the Base Case assumes a constant value of $H^+_{SO_x}$ (Makar et al., 2018). Case #1 labelled 'CALCCO3_Lw_low' applies to the use of the CALCCO3 pH adjustment, with $L_{w_{Thres}} = 0.0005$ µm. Case #2, labelled 'CALCCO3_Lw_high' is identical to Case #1 except with $L_{w_{Thres}} = 0.1$ µm. Case #3 labelled 'charge_adj_Lw_low' makes use of the charge balance adjustment described in Eq. (32) to (34) with $L_{w_{Thres}} = 0.0005$ µm. In Case #3, any pH < 4.0 is set to a floor value of 4.0 and any pH > 9.0 is set to a ceiling value of 9.0 – this is done in consideration of Fig. 2 and the range of pH impacting $V_{a_{SO_x}}$. Case #4 labelled 'charge_adj_Lw_high' also applies the charge balance adjustment like Case #3, except with $L_{w_{Thres}} = 0.1$ µm; in Case #4, any pH > 15.0 is reset to 6.68 and hence this case does not apply the strict pH adjustment bounds applied in Case #3. These different cases are summarized in Table 2.

Table 2: Main simulations performed in this work.

Case	**Adjustment Applied**	$L_{w_{Thres}}$	**Other conditions**
Base Case	N/A	N/A	pH always = 6.68
CALCCO3_Lw_low	CALCCO3	0.0005 µm	--
CALCCO3_Lw_high	CALCCO3	0.1 µm	--
charge_adj_Lw_low	Eq. 32 to Eq. 34	0.0005 µm	pH is restricted in range: $4.0 \leq pH \leq 9.0$
charge_adj_Lw_high	Eq. 32 to Eq. 34	0.1 µm	pH ≥ 15.0 is reset to 6.68

Figure 5 presents the foliage pH predicted by CALCCO3_Lw_low (left column: panels a, d) and CALCCO3_Lw_high (middle column: panels b, e) over North America at 10 km resolution for May 2018 (top row: a–c) and June 2018 (bottom row: d–f). The rightmost column (panels c, f) shows the ratio of CALCCO3_Lw_low to CALCCO3_Lw_high pH. In these ratio plots, red regions indicate where CALCCO3_Lw_low predicts a higher pH than CALCCO3_Lw_high, and blue regions indicate the opposite. The results show that CALCCO3_Lw_low generally predicts higher pH values, especially in northern British Columbia extending into Alaska, along the west coast of the United States, and in the Alberta Oil Sands Region (AOSR). The only difference between these two simulations is the threshold water layer thickness ($L_{w_{Thres}}$), set to 0.0005 µm for CALCCO3_Lw_low and 0.1 µm for

Formatted: Indent: First line: 0 cm

Formatted: Normal, Don't keep with next

Formatted: Justified

Formatted: Justified

Formatted: Justified

Formatted: Justified

Formatted: Justified

Formatted: Justified

Formatted: Indent: First line: 0 cm

CALCCO3_Lw_high. Using a smaller threshold (0.0005 µm) allows pH to be calculated under much drier conditions, leading to a significant increase in the frequency and extremity of predicted pH values. In both configurations, when $L_w < L_{w\,Thres}$, the pH is assumed to be 6.68. However, with the smaller threshold in CALCCO3_Lw_low, the model calculates pH more frequently, since fewer hours fall below the threshold where a fixed pH is assigned. Additionally, a greater number of pH calculations occur under highly concentrated conditions in CALCCO3_Lw_low, where the leaf surface water is microscopically thin but still active, resulting in more extreme pH values, either very acidic (pH < 2) or very basic (pH > 10) (see Fig. 6). These effects result in both increases (e.g., northern British Columbia; dark red areas) and decreases (e.g., widespread blue areas across North America) in the predicted foliage pH relative to in CALCCO3_Lw_high. This highlights the sensitivity of foliage pH estimates to the assumed minimum water layer thickness and underscores the importance of choosing an appropriate $L_{w\,Thres}$ value in the model.

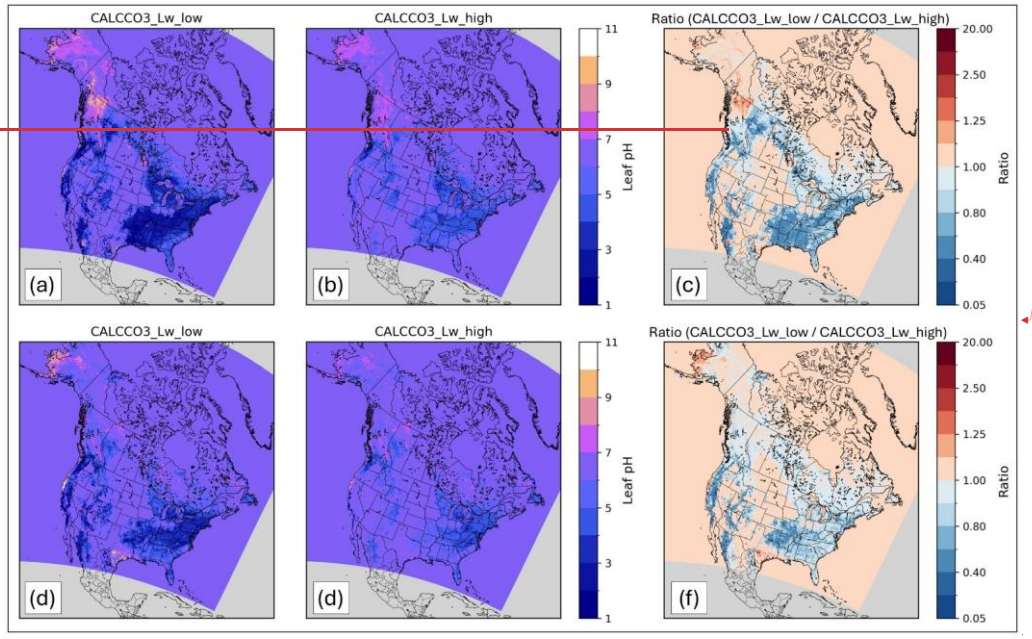

Figure 5: The mean monthly pH predicted for May 2018 (a – c) and June 2018 (d – f). The first column (a, d) shows the mean pH predicted by CALCCO3_Lw_low and the second column (b, e) by CALCCO3_Lw_high (Case #2). The third column shows the ratio of the results from the two model runs, calculated as CALCCO3_Lw_high / CALCCO3_Lw_low, demonstrating the impact of the choice of low leaf water thickness threshold on the calculated pH Thus, in the ratio plots, red areas denote areas where the predicted pH is greater in CALCCO3_Lw_low than CALCCO3_Lw_high, and vice versa for blue colours.

2018 (top row: a–c) and June 2018 (bottom row: d–f). The rightmost column (panels c, f) shows the ratio of CALCCO3_Lw_low to CALCCO3_Lw_high pH. In these ratio plots, red regions indicate where CALCCO3_Lw_low predicts a higher pH than CALCCO3_Lw_high, and blue regions indicate the opposite.

In charge_adj_Lw_low and charge_adj_Lw_high, the same impact from L_w on the estimated pH is noted at low pH since HETP is applied without subsequent adjustment. However, during periods with excess base cations (i.e., when the charge balance

Formatted: Don't keep with next

Formatted: Normal

Formatted: Indent: First line: 0 cm

adjustment is applied), the foliage water pH tends to be overpredicted, regardless of the L_w thickness. This overprediction becomes more pronounced at very low L_w, leading to unrealistically high pH estimates. To address this, a ceiling value of 9.0 was imposed in charge_adj_Lw_low (see Sect. 2.2); without this constraint, the predicted pH values can often exceed 14.0 (observed foliage pH values above 13.0 are rare, even in environments impacted by cement dust deposition; see Sect. 1). Although regions of elevated pH are similarly located in both charge_adj_Lw_low/high and CALCCO3_Lw_low/high, the magnitude of the predicted foliage water pH differs substantially. Both charge_adj_Lw_low/high tend to default to the ceiling of 9.0 whenever base cations are in excess and struggle to resolve variations in the pH range between 7.5 to 9.0. Variations in this range are important to capture because a pH near 9.0 corresponds to a near-maximum deposition velocity of SO_2 (see Fig. 2). Consequently, charge_adj_Lw_low and charge_adj_Lw_high likely represent the upper bound of the impact that pH modulation could have on SO_2 dry deposition. In contrast, CALCCO3_Lw_low and CALCCO3_Lw_high more accurately capture pH variability within the 7.5 to 9.0 range, allowing for a more realistic modulation of SO_2 deposition velocities. For this reason, we note that a simple charge balance is insufficient to accurately estimate leaf cuticle pH, and charge_adj_Lw_low and charge_adj_Lw_high are not discussed further in the subsequent sections. It is also worth noting that the CALCCO3 adjustment will approach the charge adjustment in the event that the water layers become sufficiently dilute to be considered "ideal". However, the comparison here suggests that high concentration (i.e. non-ideal solution) algorithms are indeed required to adequately simulate pH levels on leaf surfaces – the water layers are sufficiently thin to require the use of activity coefficient calculations as in CALCCO3. While the CALCCO3 routine itself does not explicitly consider activity coefficients during the pH adjustment, the initial ion concentrations used in the adjustment are derived from HETP which applies a rigorous treatment of activity coefficients (Miller et al., 2023; Fountoukis and Nenes, 2007).

The effect of $L_{w\,Thres}$ on the predicted SO_2 deposition velocity via foliage water pH is demonstrated in Fig. 56, which shows predicted $V_{d_{SO_2}}$ for our final configuration, "CALCCO3_Lw_low (a, b) and CALCCO3_Lw_high", (c, d) from the 2.5 km resolution model for May 2018. May 2018We highlight this month is highlighted here since it featured many dry periods where L_w became very small and is largely dominated by aerosol water W_{aero} – later months are wetter overall. Fig. 6b and Fig. 6d show the foliage pH as a function of L_w, where L_w has been separated into 12 discrete bins; the corresponding box plot gives the range of foliage pH in that bin. CALCCO3_Lw_high, with the higher value of L_w, does not include leaf water surfaces below 0.1 μm thickness (hence no values are shown below that limit in Fig 6(d)). The top and bottom of each box in the leaf pH box plots show the 75th and 25th percentiles, while the top and bottom whiskers give the 95th and 5th percentiles respectively. The median of each bin is represented by the horizontal line within each box. This format for box plots is applied henceforth. Each box is superimposed over a shaded bar that gives the percentage of L_w values occurring in that bin, across the model domain for the given month; each bin's percentage value is displayed at the base of the shaded bar. To avoid skewing the data shown in Fig. 56, times when the pH = 6.68 are excluded: a pH = 6.68 is used as the 'reset' pH applied during times of insufficient foliage water, or in regions where there is insufficient natural vegetation (i.e., crops). The panels of Fig. 56 thus show model results when the thin water layer threshold used 0f 0.1 μm has not been exceeded in each case. As demonstrated in Fig. 6b (which shows CALCCO3_Lw_low), when $L_w < 0.05$ μm the 95th percentile of the predicted foliage pH often exceeds 8.6. In contrast, when $L_w > 0.05$ μm for this case there are no bins in which the 95th percentile of foliage pH exceeds 9.0. This demonstrates that pH values exceeding 8.6 are nearly exclusive to the thinnest (microscopic) water layers, and excluding these water layers (i.e., CALCCO3_Lw_high) largely eliminates pH predictions exceeding 9.0 (i.e., Fig. 6d). Similar results are apparent for the lowest pH values predicted by HETP, that is, a pH less than 0.5 is predicted largely when $L_w < 0.05$ μm.

~~Fig. 6a and Fig. 6c also show $V_{d_{SO_2}}$ as a function of foliage water pH for CALCCO3_Lw_low and CALCCO3_Lw_high respectively; statistics for foliage pH are binned according to $V_{d_{SO_2}}$ and displayed as a box plot (lower x-axis is the leaf pH scale). Beneath each box is a horizontal shaded bar that gives the percentage of $V_{d_{SO_2}}$ in that bin, with each bin's percentage value superimposed on the graph (upper x-axis percentage scale).~~ Fig. 5a6a and 6c clearly demonstrate the influence of foliage pH on $V_{d_{SO_2}}$; when the pH is increased above 7.0 there is an almost monotonic increase in $V_{d_{SO_2}}$(as shown by the increasing median and spread of the box plots). In contrast, in the base case (not shown) where a constant foliage pH of 6.68 is assumed, there are very few instances where $V_{d_{SO_2}}$ exceeds 1 cm s^{-1}. Compared to the base case, a much larger incidence of $V_{d_{SO_2}}$ exceeding 1 cm s^{-1} are predicted in ~~CALCCO3_Lw_low and~~ CALCCO3_Lw_high coinciding with times when the predicted foliage pH exceeds 6.68. Although the distribution of $V_{d_{SO_2}}$ still peaks in the 0.3 to 1.0 cm s^{-1} range, a significant percentage of values now fall above 1 cm s^{-1} (top three bars of Fig. 5a), which is rarely seen in the Base Case where a constant pH of 6.68 was assumed.~~.~~

Formatted: Font: Bold

Fig. 5b show the foliage pH as a function of the calculated thickness of the foliage water layer L_w, where L_w has been separated into 8 discrete bins; the corresponding box plot gives the range of foliage pH in that bin. pH is the most acidic for thin water layers, and least acidic for thicker water layers. Water layer thickness under the relatively dry conditions of May peaks between 50 to 158 μm.

Combined, the two panels of Fig. 5 show that the highest foliage pH corresponds to the highest deposition velocities, and that the higher pH levels occur for thicker water layers.

~~By comparing Fig. 6a and Fig. 6c, the effect of L_w on $V_{d_{SO_2}}$ becomes apparent. For example, when $L_{w_{Thres}}$ = 0.0005 µm (CALCCO3_Lw_low), 2.50 % of $V_{d_{SO_2}}$ exceed 3 cm s^{-1}, but when $L_{w_{Thres}}$ = 0.5 µm (CALCCO3_Lw_low), only 2.38% exceed this threshold (Fig. 6c). This represents a 5 % decrease in the frequency of high deposition velocities when the threshold water layer thickness is increased. This suggests that allowing very thin water layers may enable more frequent prediction of extremely high $V_{d_{SO_2}}$ values. In both CALCCO3_Lw_low and CALCCO3_Lw_high, the majority of $V_{d_{SO_2}}$ fall within the 0.01 to 1.0 cm s^{-1} range (72.58% and 71.17% respectively). Interestingly, despite CALCCO3_Lw_low simulating more acidic conditions than CALCCO3_Lw_high (due to more frequent highly concentrated water layers) there is little difference in the frequency of the smallest $V_{d_{SO_2}}$: only 0.04% of the values from CALCCO3_Lw_low are fall below 0.03 cm s^{-1}, compared to 0.03% for CALCCO3_Lw_high. Additionally, there is no clear trend of decreasing $V_{d_{SO_2}}$ as the foliage pH drops below 6.68, reinforcing the conclusion that the pH modulation of SO_2 deposition is most important the 6 and 9 range. This analysis underscores the role of $L_{w_{Thres}}$ in determining the frequency and magnitude of high $V_{d_{SO_2}}$ associated with elevated foliage pH is relatively minor.~~

~~The results presented in this section suggest that CALCCO3_Lw_high is likely the more appropriate configuration for predicting dynamic foliage pH. This option avoids pH calculations during periods of very low L_w, when the aqueous solution becomes highly concentrated and activity coefficient calculations in HETP become increasingly uncertain (Fountoukis and Nenes, 2007). As a result, it reduces the occurrence of large predicted $V_{d_{SO_2}}$. These low L_w periods likely correspond to times when the water layer does not form a continuous film over the leaf surface but instead exists as microscopic beads (Rosado and Holder, 2013), thereby limiting the actual surface area available for gas dissolution. Therefore, allowing GEM-MACH to predict high $V_{d_{SO_2}}$ when L_w < 0.1 µm may not be physically realistic. This interpretation is further supported by the poor agreement between modeled and observed SO_2 surface concentrations during May. In that month, foliage water layers are often sustained only by aerosol deliquescence, resulting in very high ionic strength. Under these conditions, CALCCO3_Lw_high (which assumes a thicker water layer and hence lower ionic strength) shows better statistical agreement with observations than CALCCO3_Lw_low at several monitoring stations (see Sect. 5.3). Hence in the sections that follow, we focus on the results of CALCCO3_Lw_high.~~

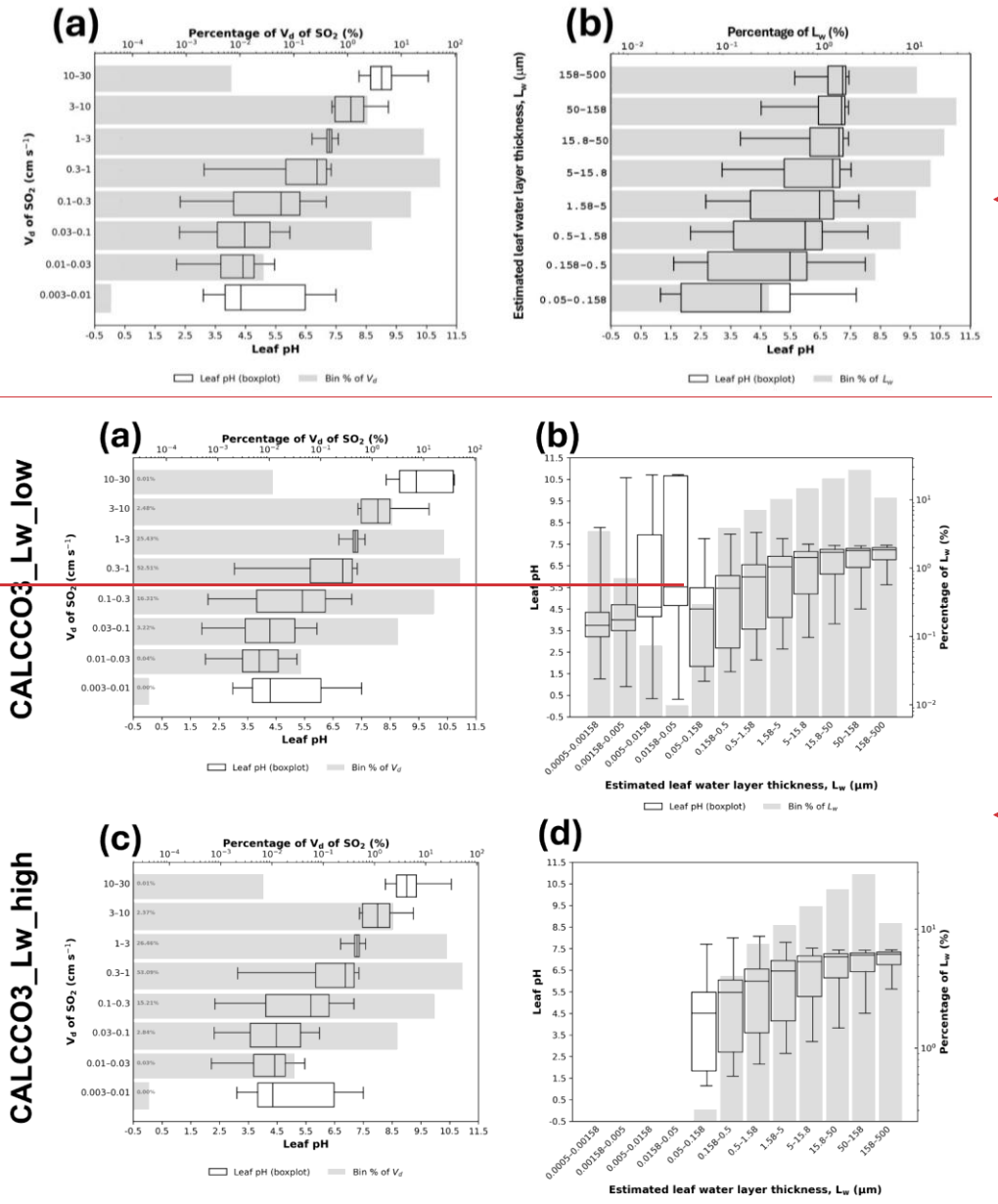

**Figure 5~~6~~: (a): ~~Panel a and c shows t~~The deposition velocity of SO_2 ($V_{d_{SO2}}$, cm s^{-1}) as a function of foliage (leaf) pH; data are from May 2018. $V_{d_{SO2}}$ has been separated into 8 discrete bins, and the corresponding box plots give~~s~~ the range of leaf pH (lower x-axis) ~~in that~~within each bin. The whiskers, box boundaries, central vertical line, etc. from left to right for each box are the 5th percentile, 25th percentile, median, 75th percentile, and 95th percentile, respectively. This format for box plots is applied henceforth. Each box is superimposed over a shaded bar that gives the ~~bin.~~

Formatted: Indent: First line: 0 cm

Formatted: Justified

Formatted: Superscript

Formatted: Superscript

Formatted: Superscript

Formatted: Superscript

Formatted: Superscript

~~The shaded bars give the~~ percentage of V_{dSO2} in the corresponding~~each~~ bin (upper x-axis)~~; each percentage value is superimposed on the graph~~. ~~(b)Panel c and d show:~~ T~~t~~he foliage (leaf) pH as a function of the estimated leaf water layer thickness (L_w, μm). L_w has been separated into 12 discrete bins, and the corresponding box plot gives the range of leaf pH in the corresponding~~hat~~ bin. The shaded bars give the percentage of L_w in each bin (right y-axis)~~; each percentage value is superimposed~~.

~~**Figure 7 shows the mean foliage pH predicted from CALCCO3_Lw_high, with a zoom of the AOSR. Figure 7(a), (b) and (c) show May, June and July 2018 respectively, using model output from the 2.5 km resolution nested domain. The AOSR appears as a distinct region of relatively alkaline foliage (7.5 ≤ pH ≤ 9.0). Downwind of the AOSR, the foliage pH decreases – first becoming neutral, then progressively more acidic (pH < 5.5) in May, with pH's of 6.5-7.5 downwind of the Oil Sands facilities in June and July. This spatial trend is consistent with the known behaviour of atmospheric PM in the region. The alkaline leaf surfaces in the AOSR are primarily due to coarse mode dust, which contains high levels of base cations and is deposited relatively close to emission sources (Zhang et al., 2018). In contrast, particulate sulphate is predominately found in the fine mode and can be transported much further downwind, beyond the zone of significant alkaline dust deposition. As a result, acidic conditions dominate further from the source region, where the neutralizing influence of base cations diminishes. This pattern is consistent with findings from Makar et al., (2018) who showed that at downwind distances less than 140 km from Oil Sands sources base cations are likely in excess relative to anions. Further insight is provided by examining the predicted composition of particulate matter deposited onto foliage in areas where high foliage pH values are predicted (see Fig. S2). These regions receive a large fraction of deposited mass as particulate calcium, mainly in the form of calcium carbonate ($CaCO_3$) (Watson et al., 2014; Wang et al., 2015). Upon deposition and dissolution in the leaf water layer, $CaCO_3$ hydrolyses raising the pH, consistent with the alkaline areas predicted in Fig. 7.~~

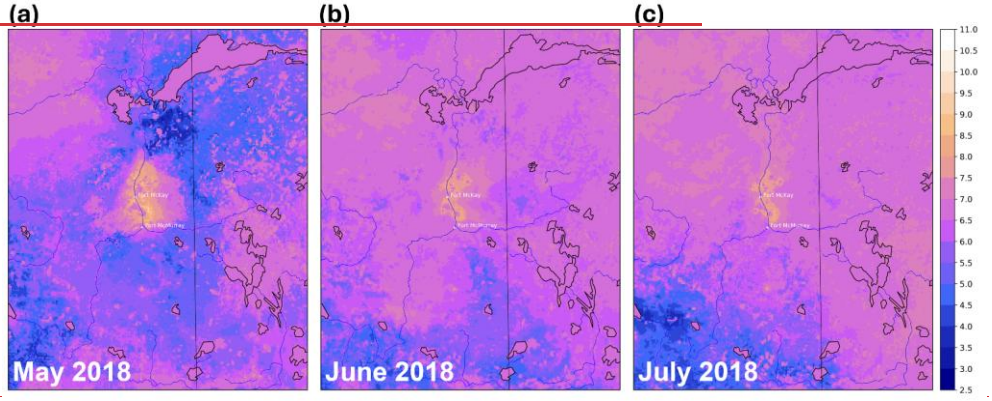

~~**Figure 7:** The mean foliage pH predicted using CALCCO3_Lw_high for (a) May 2018, (b) June 2018 and (c) July 2018. The results shown here are from the 2.5 km resolution nested domain of the GEM-MACH model, for a subregion centred on the largest facilities of the Athabasca Oil Sands.~~

5.2 Impact of pH on predicted SO_2 deposition velocities, surface concentrations, and deposition fluxes ~~Impact of pH on the deposition velocity of SO_2~~

~~Figure 8 shows the mean $V_{d_{SO_2}}$ predicted by the Base Case (top row: a, b, c) and by CALCCO3_Lw_high (middle row: d, e, f) over the 2.5 km resolution domain. Each column of Fig. 8 shows a different month: May (left column: a, d, g), June (middle column: b, e, h) and July (right column: c, f, i). The bottom row (g, h, i) shows the ratio of CALCCO3_Lw_high to the Base Case (i.e., ratio = $V_d^{CALCCO3\_Lw\_high} / V_d^{Base}$). In these ratio plots, red shading indicates where CALCCO3_Lw_high predicts larger $V_{d_{SO_2}}$ than in the Base Case, and blue shading shows the opposite. As expected from the results of Fig. 6 and Fig. 7, the highest mean $V_{d_{SO_2}}$ (exceeding 2 cm s^{-1}) occur in the AOSR irrespective of month. Near the Oil Sands facilities, CALCCO3_Lw_high predicts $V_{d_{SO_2}}$ values that are on average 2.5 to 10 times greater than those predicted by the Base Case. This range is consistent with aircraft measurements from Hayden et al. (2021), who observed that measured (inferred) $V_{d_{SO_2}}$ were 1.7 to 5.4 times larger than Base Case predictions from GEM-MACH.~~

Formatted: Font: Symbol

Formatted: Caption, Indent: First line: 0 cm

Formatted: Caption, Don't keep with next

Formatted: Caption

Formatted: Subscript

In July, a pronounced increase in $V_{d\,SO_2}$ is predicted by CALCCO3_Lw_high in northwestern Alberta, near the edge of the model domain. This enhancement is linked to wildfire emissions, which GEM-MACH predicts to cause alkaline foliage conditions (i.e., pH > 8.0) due to the deposition of wildfire-originating coarse mode base cations. Investigation of wildfire ash chemical composition support this result, with studies showing that $CaCO_3$ is a major component, and its dissolution in water often results in alkaline solutions with pH > 7.5, sometimes as high as 11 (Sánchez-García et al. 2023; Pereira et al., 2013; Pereira et al., 2012). Conversely, in the Foothills of Alberta where the foliage pH is often predicted to be acidic (i.e., Fig. 5, and blue regions of Figure 8(g, h, i)), CALCCO3_Lw_high predicts a 20 to 25 % reduction in $V_{d\,SO_2}$ compared to the base case. This reduction appears as dark blue areas east of the Alberta - British Columbia border, highlighting that the pH-modulated $V_{d\,SO_2}$ can vary substantially across the domain, depending on the chemical composition of the mass deposited onto foliage.

As the pH increases above 9.0, both $r_{cut}(SO_2)$ and the canopy resistance $r_c(SO_2)$ approach zero. In this work, a minimum value of 10^{-2} s m^{-1} was imposed on r_{cut}, which is much lower than the 20 s m^{-1} limit suggested by Zhang et al., (2003) under wet conditions. Applying the 20 s m^{-1} threshold would dampen the pH effects on $V_d(SO_2)$ beyond a pH of 8.0. However, that threshold is not based on field measurements. Sorteberg and Hov (1996) noted that no such measurements exist, and recent studies have reported $r_c(SO_2) \approx 0$, particularly in wet conditions (Neirynck et al., 2011; Feliciano et al., 2001). These findings suggest that $r_{cut}(SO_2) \ll 20$ s m^{-1} is plausible. If very low $r_{cut}(SO_2)$ lead to unrealistic V_d estimates, this may reflect issues with the parameterization of r_a and r_b, rather than with r_{cut} itself.

Formatted: Indent: First line: 0 cm

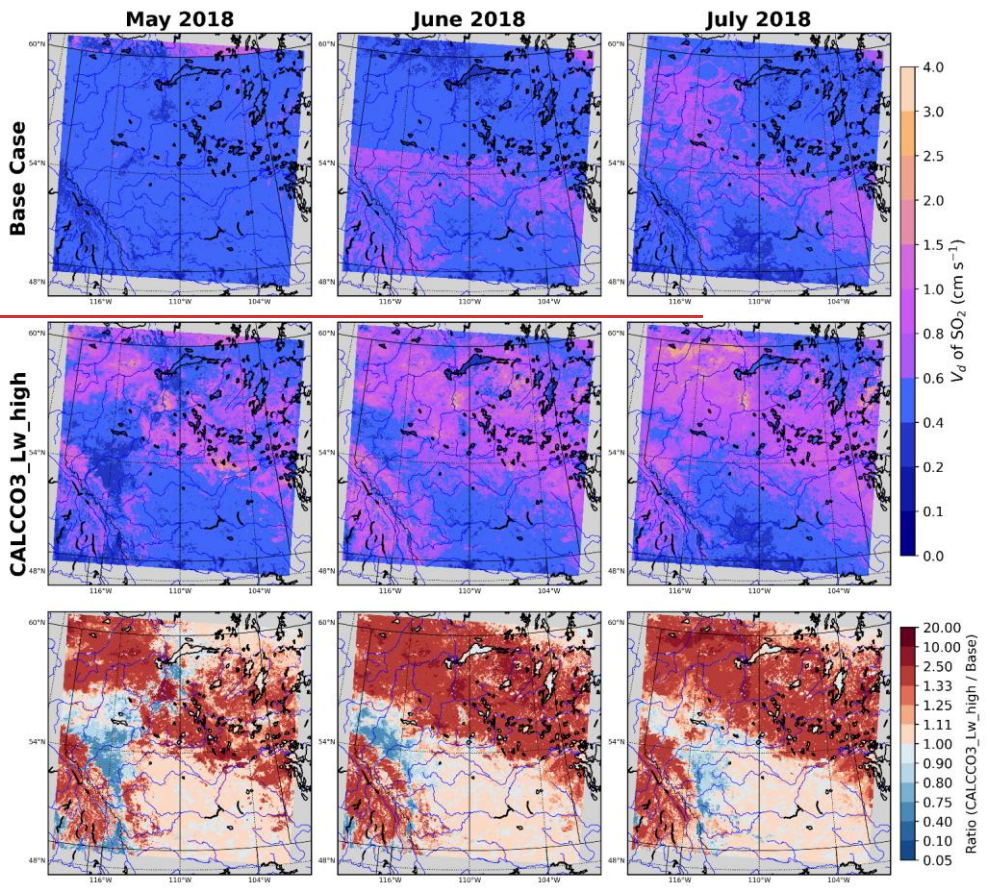

~~Figure 8: The mean deposition velocity of SO_2 (V_{dSO_2}) calculated from the Base Case of GEM-MACH (a, b, c) and CALCCO3_Lw_high (d, e, f). The columns denote specific months, with the first (a, d, g), second (b, e, h) and third (c, f, i) columns representing May, June and July 2018 respectively. The final row (e, h, i) shows the ratio of CALCCO3_Lw_high / Base Case; blue colours denote areas where V_{dSO_2} has decreased relative to the base case, while red values denote regions where V_{dSO_2} has increased.~~

The model's monthly average estimates of surface pH in the AOSR, and the corresponding (CALCCO3_Lw_high) : (Base Case) ratios of monthly average SO_2 deposition velocities, surface concentrations and deposition fluxes over the entire model domain, are shown in Figures 6, 7, and 8 for the months of May, June and July of 2018, respectively. Supplement Figures S3, S4 and S5 provide the corresponding Base Case and CALCCO3_Lw_high values of the latter three quantities in each month, and Figure S6 shows the differences in monthly mean deposition velocity and surface concentrations of SO_2.

Formatted: Don't keep with next

Formatted: Normal

Formatted: Heading 2, Indent: First line: 0 cm

Formatted: Subscript

Formatted: Subscript

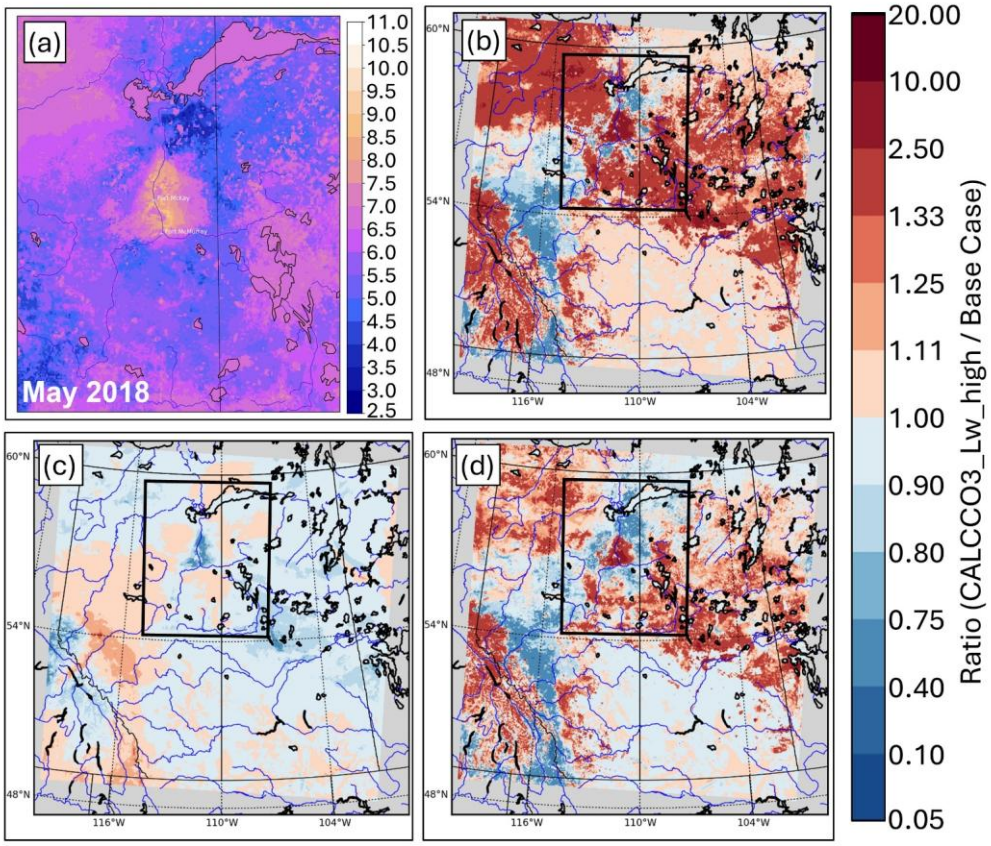

Figure 6. Average impact of surface foliage pH. May, 2018. (a): AOSR average surface foliage pH calculated using CALCCO3_Lw_high. (b,c,d) Ratios (CALCCO3_Lw_high: Base Case) of (b) $V_{d_{SO2}}$, (c) SO_2 concentration at the surface, (d) Monthly SO_2 deposition flux at the surface. Inset box in panels (b,c,d) shows the AOSR, displayed as a "zoom" in panel (a). Supplemental Figure S3 shows the Base Case and CALCCO3_Lw_high values corresponding to panels (b,c,d).

The AOSR appears as a distinct region of relatively alkaline foliage (7.5 ≤ pH ≤ 9.0), Fig. 6-8(a). Downwind of the AOSR, the foliage pH decreases – first becoming neutral, then progressively more acidic (pH < 5.5) in May (Fig. 6(a)), with pH's of 6.5 to 7.5 downwind of the Oil Sands facilities in June (Fig. 7(a)) and July (Fig. 8(a)). The highest pH levels (>9, orange to yellow colours in panel (a) of Figures 6 -8) are located close to the open pit mine facilities for all three months – that is, close to the source of base-cations originating in fugitive dust. This spatial trend is consistent with the known behaviour of atmospheric PM in the region. The alkaline leaf surfaces in the AOSR are primarily due to coarse mode dust, which contains high levels of base cations and is deposited relatively close to emission sources (Zhang et al., 2018). In contrast, particulate sulphate is predominately found in the fine mode and can be transported much further downwind, beyond the zone of significant alkaline dust deposition. As a result, acidic conditions dominate further from the source region, where the neutralizing influence of base cations diminishes. This pattern is also consistent with findings from Makar et al., (2018) who showed that at downwind distances less than 140 km from Oil Sands sources base cations are likely in excess relative to anions. Further insight is provided by examining the predicted

Formatted: Font: 9 pt, Bold
Formatted: Font: 9 pt
Formatted: Indent: First line: 0 cm
Formatted: Font: 9 pt
Formatted: Font: 9 pt
Formatted: Font: 9 pt
Formatted: Font: 9 pt
Formatted: Font: 9 pt
Formatted: Font: 9 pt
Formatted: Font: 9 pt, Subscript
Formatted: Font: 9 pt
Formatted: Font: 9 pt, Subscript
Formatted: Font: 9 pt
Formatted: Font: 9 pt

composition of particulate matter deposited onto foliage in areas where high foliage pH values are predicted (e.g. central high pH region, Figs. 6-8(a)). These regions receive a large fraction of deposited mass as particulate calcium, mainly in the form of calcium carbonate ($CaCO_3$) (Watson et al., 2014; Wang et al., 2015). Upon deposition and dissolution in the leaf water layer, $CaCO_3$ hydrolyses, raising the pH, consistent with the alkaline areas predicted in Fig. 6-8(a). This results in substantial increases in the SO_2 deposition velocity (brown regions, Figs. 6-8(b)), decreases in the SO_2 surface concentration (blue regions, Figs. 6-8(c)), and increases in the SO_2 dry deposition flux (brown regions, Figs. 6-8(d)).

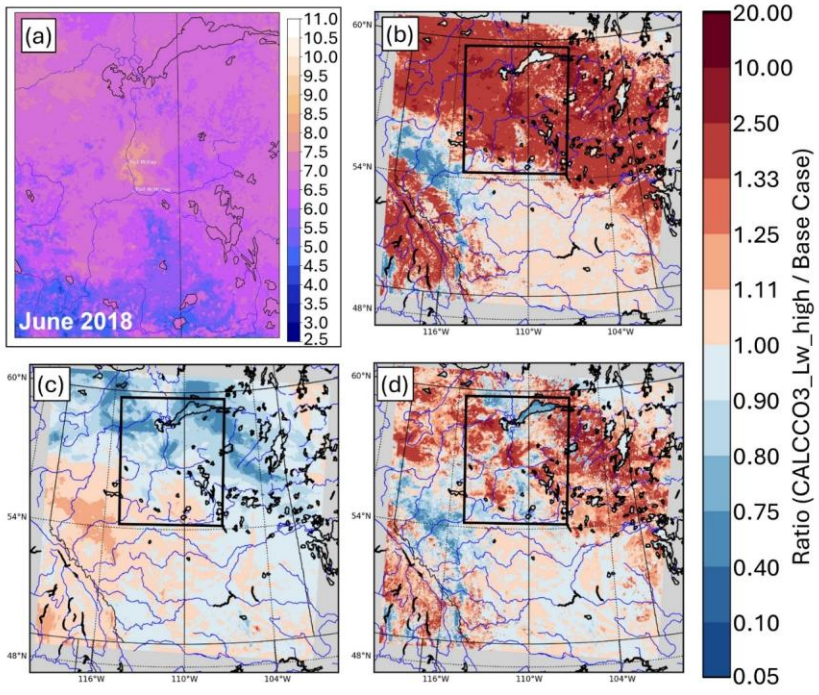

Figure 7: Average impact of surface foliage pH. June, 2018. Panels as in Figure 6. Supplemental Figure S4 shows the Base Case and CALCCO3_Lw_high values corresponding to panels (b,c,d).

Outside of the region influenced by Oil Sands facility fugitive dust, background pH levels increase from May and June (compare Fig 6(a) with 7(a), 8(a)) due to additional base cation deposition originating in forest fire particulate matter emissions, which increase towards the summer.

All three months show a substantial increase in $V_{d_{SO_2}}$ relative to the base case (Figures 6-9, panels (b)) with the use of the CALCCO3_Lw_high pH-dependent deposition algorithm in regions influenced by substantial base cation deposition. Base case deposition velocities over the domain range from 0.4 to 1.0 cm s^{-1}, while reaching 4.0 cm s^{-1} for CALCCO3_Lw_high (see Supplement Figures S3, S4, S5), with monthly average (CALCCO3_Lw_high) : (Base Case) ratios between 1.33 and 2.5 becoming common in the latter months in the boreal forest area. Ratios between 2.5 and 10 are present in the Oil Sands area in all three months due to the emissions of open pit mine fugitive dust from those facilities. Ratios of $V_{d_{SO_2}}$ also reach values greater than 2.5

Formatted: Subscript
Formatted: Subscript
Formatted: Subscript
Formatted: Centered, Indent: First line: 0 cm
Formatted: Indent: First line: 0 cm
Formatted: Superscript
Formatted: Superscript

in areas of forest fire emissions in all three months (eg. top left corner Figure 8(b)). The ratios of $V_{d_{SO_2}}$ in the AOSR are consistent with aircraft measurements from Hayden et al. (2021), who observed that measured (inferred) $V_{d_{SO_2}}$ was 1.7 to 5.4 times larger than Base Case predictions from GEM-MACH simulations lacking the pH correction described here.

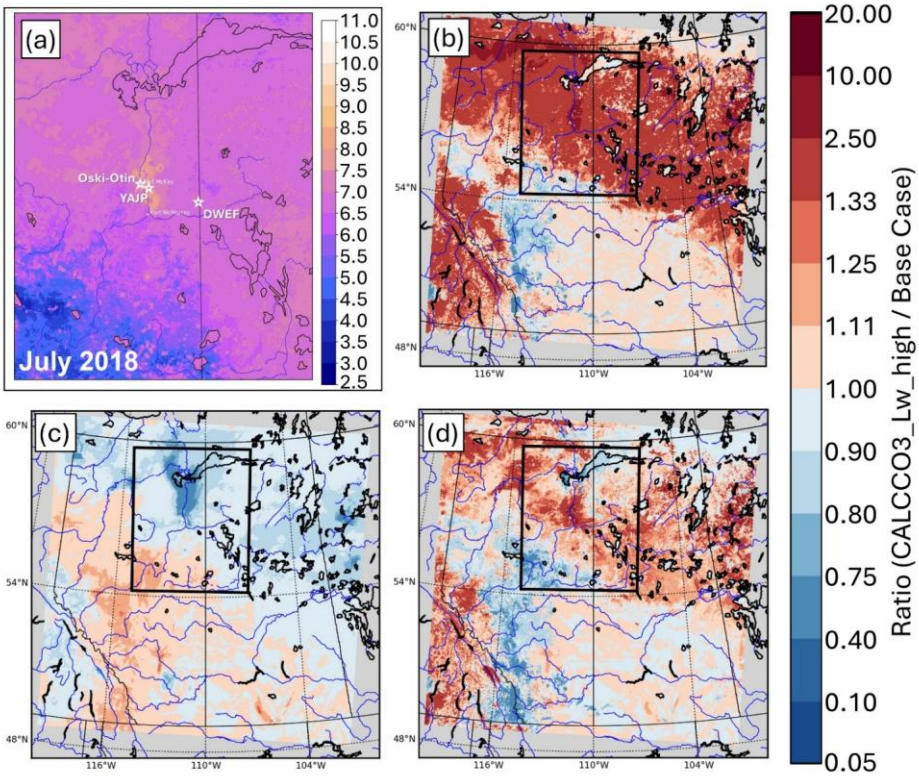

Figure 8: Average impact of surface foliage pH. July, 2018. Panels as in Figure 6. Supplemental Figure S5 shows the Base Case and CALCCO3_Lw_high values corresponding to panels (b,c,d). The locations of Oski-otin, YAJP and DWEF (stars) are provided for reference to Figure 9.

Investigation of wildfire ash chemical composition support the importance of forest fire emissions towards foliage pH, with studies showing that CaCO3 is a major component; its dissolution in water often resulting in alkaline solutions with pH > 7.5, and sometimes as high as 11 (Sánchez-García et al. 2023; Pereira et al., 2013; Pereira et al., 2012). Conversely, in the Foothills of Alberta where the foliage pH is often predicted to be acidic (blue regions Figures 6-9, panel (b)), CALCCO3_Lw_high predicts a 20 to 25 % reduction in $V_{d_{SO_2}}$, highlighting that the pH-modulated $V_{d_{SO_2}}$ can vary substantially across the domain, depending on the chemical composition of the mass deposited onto foliage.

As the pH increases above 9.0, both $r_{cut_{zha}}(SO_2)$ and the canopy resistance $r_c(SO_2)$ approach zero (see Figure 2). In this work, a minimum value of 10^{-2} s m^{-1} was imposed on r_{cut}, which is much lower than the 20 s m^{-1} limit suggested by Zhang et al., (2003) under wet conditions. Applying the 20 s m^{-1} threshold would dampen the pH effects on $V_{d_{SO_2}}$ beyond a pH of 8.0. However, the Zhang et al (2003) threshold was not based on field measurements. While Sorteberg and Hov (1996) noted that no such

Formatted: Centered
Formatted: Indent: First line: 0 cm
Formatted: Font: 9 pt
Formatted: Superscript
Formatted: Superscript
Formatted: Superscript
Formatted: Superscript

measurements existed, more recent studies have reported $r_c(SO_2) \approx 0$, particularly in wet conditions (Neirynck et al., 2011; Feliciano et al., 2001). These findings suggest that $r_{cut}(SO_2) \ll$ 20 s m^{-1} is plausible. If very low $r_{cut_{zha}}(SO_2)$ lead to unrealistic V_d estimates, this may reflect issues with the parameterization of r_a and r_b, rather than with $r_{cut_{zha}}$ itself.

Figure 6-8 (c) show the response of surface SO_2 concentrations towards these changes in $V_{d_{SO_2}}$. The largest decreases occur in the AOSR (ratios between 0.40 and 0.75; reductions of 0.25 to 0.75 ppb, see also Supplement Figs. S3, S4, S5). Large ratio decreases in SO_2 of between 0.40 and 0.75 can also be seen throughout the northern part of the domain in June (Figure 7(c)), a particularly active forest fire base cation emissions and deposition month in 2018. However, in these areas the absolute change is small (< 0.1 ppb, see Fig. S4), limiting practical significance despite the large percentage difference. Localized SO_2 concentration increases of 10 to 30 % are predicted in some regions, including the Foothills of Alberta and west of Cold Lake (orange colours, Fig. 6-8 (c)), where corresponding decreases in $V_{d_{SO_2}}$ have been predicted (panels (b)). Although the absolute increases are typically < 0.1 ppb (Fig. S3, S4, S5), there are localized areas exceeding 0.25 ppb. In absolute terms this decrease in the mean $V_{d_{SO_2}}$ is much less than the increase seen in the AOSR, which often exceeds 1.0 cm s^{-1}. This result demonstrates that even a relatively small decrease in the mean $V_{d_{SO_2}}$ (due to acidic foliage conditions) may cause a disproportionately large (localized) increase in the simulated mean surface SO_2 concentration. We note that the largest concentration decreases (blue colours, Figures 6-8(c)) correspond to areas and times where there is a high local deposition flux of base cations, from the Oil Sands facilities' fugitive dust emissions, or from forest fires.

The net impact of the changes on the SO_2 deposition flux (DSO2) is shown in Fig. 6-8(d). As outlined in Sect. 2, DSO2 is the calculated on a time-step basis as the product of $V_{d_{SO_2}}$ and the surface SO_2 concentration. Thus, increases in $V_{d_{SO_2}}$ only translate to increased DSO2 where appreciable surface SO_2 concentrations are present. Where SO_2 is available, however, higher $V_{d_{SO_2}}$ will proportionally increase DSO2, all else being equal. Accordingly, the largest absolute increases in DSO2 under CALCCO3_Lw_high occur in the AOSR, where elevated $V_{d_{SO_2}}$ (2.5 - 10 cm s^{-1}) coincide with elevated surface SO_2 concentrations (> 2 ppb). Since SO_2 emissions are identical in both Base Case and CALCCO3_Lw_high simulations, this increased flux is entirely attributable to changes in $V_{d_{SO_2}}$ resulting from base cation-driven co-deposition. This enhancement is consistent with aircraft-based measurements reported by Hayden et al., (2021), who found that an earlier version of GEM-MACH, lacking the pH $V_{d_{SO_2}}$ enhancement, underpredicted the dry deposition flux of total oxidized sulphur (TOS) by 2 to 14 times. While TOS measured in their study also included particulate sulphate, over 92 % of TOS their campaign was in the form of gaseous SO_2 making it reasonably representative of $V_{d_{SO_2}}$.

Further downwind, particularly beyond 100 km from the AOSR, DSO2 is reduced relative to the Base Case by up to 40%, especially in May (Fig. 6). Two factors contribute to this reduction – (1) depletion of SO_2 from upwind deposition and (2) local inhibition of deposition to acidic foliage conditions. The latter likely dominates, based on the spatial patterns: in regions where DSO2 is reduced under CALCCO3_Lw_high, surface SO_2 concentrations are increased relative to the Base Case, particularly in May (Fig . 6) – this occurs despite enhanced SO_2 removal to forests just upwind.

5.3 Comparison of modelled $V_{d_{SO_2}}$ and SO_2 at surface monitoring network observations

Three locations in the 2.5 km model domain; Oski-otin (near the village of Fort Mackay), the York Athabasca JackPine site (YAJP), and a downwind evergreen forest location near the Saskatchewan border (DWEF) are superimposed on the monthly average leaf pH field in Figure 8(a), and their corresponding diurnal cycles of $V_{d_{SO_2}}$ for the months of May and June are shown in Figure 9. ~~Figure 9 shows the diurnal cycle of $V_{d_{SO_2}}$ predicted by the Base Case (black) and CALCCO3_Lw_high (blue) for~~

Formatted: Superscript
Formatted: Subscript
Formatted: Subscript
Formatted: Subscript
Formatted: Superscript
Formatted: Subscript
Formatted: Subscript
Formatted: Subscript
Formatted: Subscript
Formatted: Superscript
Formatted: Subscript
Formatted: Subscript
Formatted: Subscript
Formatted: Subscript
Formatted: Subscript
Formatted: Subscript
Formatted: Subscript
Formatted: Subscript
Formatted: Heading 2, Indent: First line: 0 cm

~~May (top row: a, b, c) and June (bottom row: d, e, f). Data are from the 2.5 km resolution nested model domain. Each column represents a different monitoring location: Oski-otin (left column: a, d), the the York Athabasca JackPine site (YAJP) (middle: b, e) and a a downwind evergreen forest (DWEF) (right: c, f) shows.~~ ~~The box plot formatting is consistent with Fig. 6 and solid lines indicate the mean $V_{d_{SO_2}}$ in each hourly bin.~~ The DWEF site was selected to represent a downwind location where anthropogenic dust deposition is minimal and foliage water layers are often acidic to near neutral. This contrasts with both YAJP and Oski-otin, where deposition of alkaline dust frequently raises the foliage pH above 7.5 (see Fig. 6-8(a)~~7~~). As expected from Fig. 6-8~~8~~(a), YAJP and Oski-otin show substantial increases in $V_{d_{SO_2}}$ when CALCCO3_Lw_high is applied. At these sites, the mean $V_{d_{SO_2}}$ exceeds 1.0 cm s^{-1} at all hours of the day, except in May at Oski-otin. Although the average remains high, individual values of $V_{d_{SO_2}}$ vary widely – from as low as 0.5 cm s^{-1} to over 4.0 cm s^{-1} – as reflected in the large interquartile range (IQR). In the afternoon, the IQR exceeds 2 cm s^{-1} at YAJP and Oski-otin indicating strong temporal variability. In contrast, the Base Case rarely predicts a $V_{d_{SO_2}}$ that exceeds 0.5 cm s^{-1} at these locations, with a much narrower IQR around 0.2 cm s^{-1}. A notable exception occurs at Oski-otin in May between 12:00 to 00:00, where the median, 25th and 75th percentile for CALCCO3_Lw_high closely match those of the Base Case. This is due to insufficient predicted foliage water, leading to the pH being reset to 6.68 (the same constant value used in the Base Case). Nonetheless, the mean $V_{d_{SO_2}}$ during this period is still much higher than median, implying that a small number of very high values significantly raises the mean.

The $V_{d_{SO_2}}$ predicted by CALCCO3_Lw_high at Oski-Otin and YAJP are in the range of $V_{d_{SO_2}}$ inferred from tower and aircraft measurements reported in Hayden et al., (2021) and Gordon et al., (2023). Specifically, Hayden et al. (2021) measured $V_{d_{SO_2}}$ at a tower site in the AOSR over a three-day period (6 to 8 June 2018), finding a mean afternoon value (13:00 to 19:00) of 4.1 cm s^{-1}, with minimal uptake of SO_2 during the night ($V_{d_{SO_2}}$ < 0.5 cm s^{-1}). These values fall well within the diurnal ranges predicted by CALCCO3_Lw_high at Oski-otin (see Fig. 9~~9~~). Aircraft-based estimates from Hayden et al., (2021) (conducted between 13 Aug and 07 Sept 2013) reported afternoon $V_{d_{SO_2}}$ values ranging from 1.2 to 3.4 cm s^{-1}. Although these measurements were made in a different year and spanned various surface types (i.e., forests, lakes, wetlands and tailings ponds) they also align well with the CALCCO3_Lw_high predictions. At YAJP, Gordon et al. (2023) inferred $V_{d_{SO_2}}$ between July and October 2021, reporting values between 2.1 and 5.9 cm s^{-1}. While the Gordon et al (2023)~~his~~ measurement period does not overlap with the 2018 model simulations shown in Fig. 9~~9~~, similar magnitudes of anthropogenic dust deposition in both years suggest comparable pH conditions, and consequently, similar SO_2 uptake rates. In summary, all three observational datasets report $V_{d_{SO_2}}$ values within the range predicted by CALCCO3_Lw_high, reinforcing that the pH-dependent deposition algorithm offers a substantial improvement over the Base Case in replicating observed $V_{d_{SO_2}}$ in the AOSR.

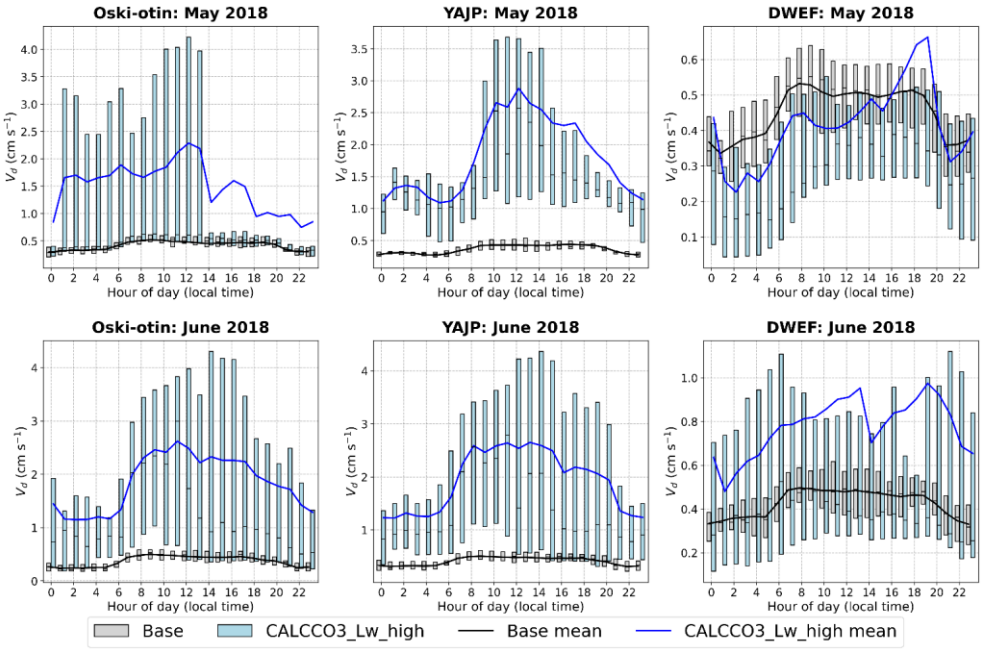

Figure 29: The diagnosed $V_{d_{SO_2}}$ at (a, d) Oski-otin, (b, e) the York Athabasca Jack Pine (YAJP) Tower, (c, f) a downwind evergreen forest (DWEF). The first row (a, b, c) shows the predicted $V_{d_{SO_2}}$ for May 2018 while the second row (d, e, f) shows June 2018. The box plot formatting in Figure 9 is consistent with Fig. 5 and solid lines indicate the mean $V_{d_{SO_2}}$ in each hourly bin. ~~The results are predictions using CALCCO3_Lw_high output from the 2.5 km resolution domain of GEM-MACH.~~

~~Figure 9 shows the diurnal cycle of $V_{d_{SO_2}}$ predicted by the Base Case (black) and CALCCO3_Lw_high (blue) for May (top row: a, b, c) and June (bottom row: d, e, f). Data are from the 2.5 km resolution nested model domain. Each column represents a different monitoring location: Oski-otin (left column: a, d), the the York Athabasca JackPine site (YAJP) (middle: b, e) and a a downwind evergreen forest (DWEF) (right: c, f) shows.~~

~~5.3 Modelled SO_2 surface concentrations and evaluation against surface monitoring network observations~~

~~Figure 10 presents the mean surface SO_2 concentration over the 2.5km resolution model domain, following the same format as Fig. 8. The largest absolute decrease in the mean surface SO_2 concentration relative to the Base Case (0.25 to 0.75 ppb; Fig. S3) occurs in the AOSR, near the Oil Sands facilities, where co-deposition of SO_2 with base cations is greatest. This corresponds to a relative reduction of up to 60% (Fig. 10 g-i). Other regions also show large reductions in mean surface SO_2 concentrations of up to 60 %, particularly north and east of Lake Athabasca in July. However, in these areas the absolute change is small (< 0.1 ppb), limiting practical significance despite the large percentage difference. While the AOSR generally shows a decrease in the mean surface SO_2 concentration, localized increases of 10 to 30 % are predicted in some regions, including the Foothills of Alberta and west of Cold Lake (orange colours , Figure 10). Although the absolute increases are typically < 0.1 ppb, there are localized areas exceeding 0.25 ppb (Fig. S3). These increases arise from a decrease in the mean $V_{d_{SO_2}}$ predicted by CALCCO3_Lw_high, on the order of 0.1 to 0.25 cm s^{-1} (see Fig. S2 and Figure 8). In absolute terms this decrease in the mean $V_{d_{SO_2}}$ is much less than the increase seen in the AOSR, which often exceeds 1.0 cm s^{-1}. This result demonstrates that even a~~

~~relatively small decrease in the mean $V_{d\,SO_2}$ (due to acidic foliage conditions) may cause a disproportionately large (localized) increase in the simulated mean surface SO_2 concentration. We note that the largest decreases (blue colours, bottom row of Figure 10) correspond to areas and times where there is a high local flux of base cations, from the Oil Sands facilities' fugitive dust emissions, or from forest fires.~~

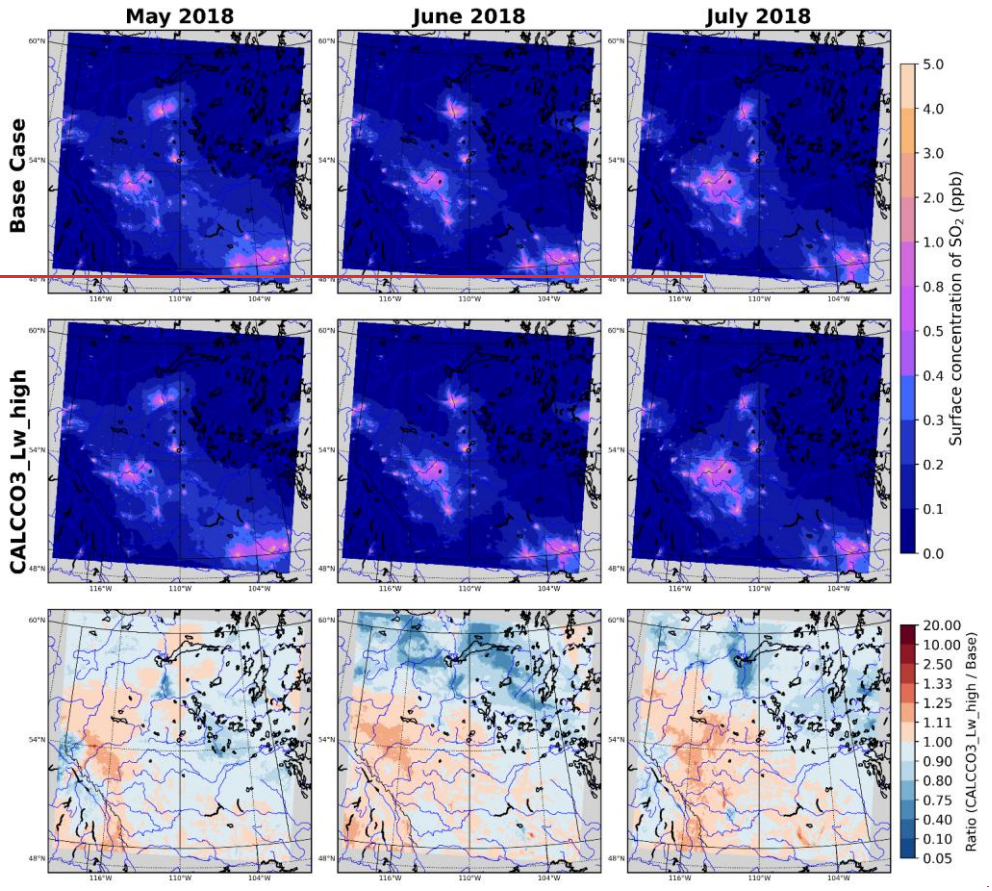

~~Figure 10:~~ ~~Identical to Fig. 8, except now the plots show the mean SO_2 surface concentration.~~

Time series of both observed and simulated mean diurnal cycles of the surface SO_2 concentration at ~~Figure 11 displays the mean diurnal cycle (local time) of the surface SO_2 concentration (ppb) during June 2018 at~~ 20 different WBEA continuous monitoring stations (Figures 10, S7, S8, S9, and 11, S10) show that th~~. Each plot shows observations (red dashed line), the Base Case (black line) and CALCCO3_Lw_high (blue line). Identical plots for May, July and August 2018 are provided in the supplemental material (Figures S4, S5, S6, respectively). In June, th~~e pH-modulation effect has the most pronounced impact on the mean surface SO_2 concentrations (relative to the Base Case) at the stations BGFM, FMCS, HRZN, MUSK, FTHL and WAPI, though improvements in NMB can be seen in 13 and 15 out of 21 stations in June and August 2018 respectively (Figure 11(a,b)).

Formatted: Caption

Formatted: Subscript

. At ~~all~~ the six stations with larger improvements, CALCCO3_Lw_high yields a substantial reduction in the normalized mean bias (NMB) relative to the Base Case (Table 3, see also Fig. 11(a,b)).

Notably, WAPI is the same tower site where Hayden et al., (2021) inferred $V_{d_{SO_2}}$ during a 3-day period in June 2018. During May 2018, these same stations often show an improvement in the NMB during the afternoon when CALCCO3_Lw_high is applied. However, at night CALCCO3_Lw_high tends to underpredict surface SO_2 concentrations more severely than the Base Case. This systematic underprediction, also present to a lesser extent in the Base Case (typically by ~0.5 ppb), suggests a broader issue likely related to the quasi-laminar sublayer resistance (r_b). Specifically, it may indicate that the nocturnal atmospheric stability is not properly represented in the model; r_b may not be sufficiently enhanced in response to suppressed turbulence, leading to an overestimation of SO_2 deposition. This may also suggest that the GEM model underrepresents nocturnal atmospheric stability, possibly due to excessive turbulent mixing or an inadequate parameterization of resistances in stable boundary layers. A similar nighttime underprediction pattern appears in July. In August, however, CALCCO3_Lw_high does a better job simulating the nighttime SO_2 surface concentrations than the Base Case. The Base Case often overpredicts the mean surface SO_2 concentration during the nighttime, while CALCCO3_Lw_high shows much better agreement overall, with a NMB at most stations that is closer to 0% (i.e., Fig. 11a,b).

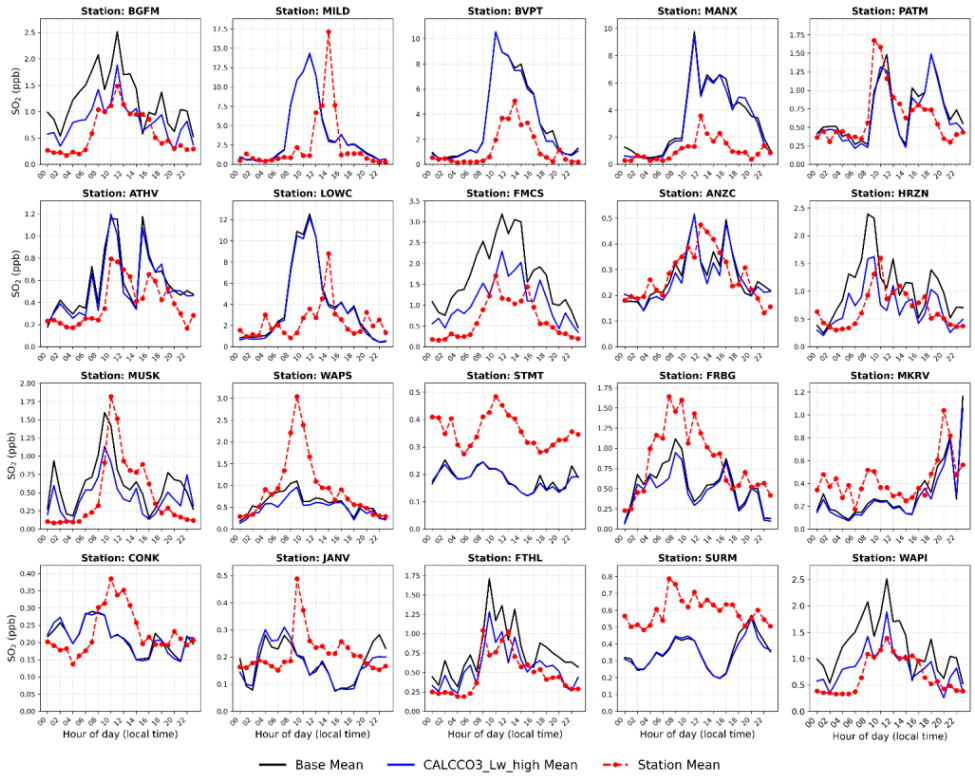

Figure 10: The mean diurnal cycle of SO_2 measured at WBEA continuous monitoring stations (red dashed line) given in local time. The data are for the month of June 2018. Also shown are the model predicted mean SO_2 surface concentrations at the same location. The black line is the Base Case, while the blue line is CALCCO3_Lw_high. Note that due to plotting limitations the WBEA station 'FTCH' is not included in the figure. Identical plots for May, July and August 2018 are provided in the supplemental material (Figures S5, S6, S7, respectively).

Formatted: Indent: First line: 1.27 cm

Table 3: Example NMB score changes by station, June 2018 (see also Figure 12(b)).

Station	Base Case NMB (%)	CALCCO3_Lw_high NMB (%)
HRZN	57.6	5.7
MUSK	34.6	- 4.5
FTHL	61.7	20.1
WAPI	83.3	22.6
BGFM	108.7	39.6
FMCS	167.9	72.6

: HRZN (57.6 → 5.7%), MUSK (34.6% → -4.5%), FTHL (61.7% → 20.1%), WAPI (83.3% → 22.6%), BGFM (108.7% → 39.6%) and FMCS (167.9% →72.6%). Notably, WAPI is the same tower site where Hayden et al., (2021) inferred $V_{d_{SO_2}}$ during a 3-day period in June 2018. During May 2018, these same stations often show an improvement in the NMB during the afternoon when CALCCO3_Lw_high is applied. However, at night CALCCO3_Lw_high tends to underpredict surface SO_2 concentrations more severely than the Base Case. This systematic underprediction, also present to a lesser extent in the Base Case (typically by ~0.5 ppb), suggests a broader issue likely related to the quasi-laminar sublayer resistance (r_b). Specifically, it may indicate that the nocturnal atmospheric stability is not properly represented in the model; r_b may not be sufficiently enhanced in response to suppressed turbulence, leading to an overestimation of SO_2 deposition. This suggests that the model underrepresents nocturnal atmospheric stability, possibly due to excessive turbulent mixing or an inadequate parameterization of resistances in stable boundary layers. A similar nighttime underprediction pattern appears in July. In August, however, CALCCO3_Lw_high does a better job simulating the nighttime SO_2 surface concentrations than the Base Case. The Base Case often overpredicts the mean surface SO_2 concentration during the nighttime, while CALCCO3_Lw_high shows much better agreement overall, with a NMB at most stations that is closer to 0% (i.e., Fig. 12d).

The application of CALCCO3_Lw_low, which permits much thinner water layers than CALCCO3_Lw_high, results in a larger absolute decrease in surface SO_2. However, this larger decrease does not compare well to observations in May. This discrepancy may imply that the presence of microscopically thin foliage water layers, primarily due to aerosol deliquescence, is less prevalent than assumed (at least during May 2018). In contrast, the difference between CALCCO3_Lw_low and CALCCO3_Lw_high is smaller in June, owing to a higher frequency of foliage water predicted by the meteorological model. This reduces the occurrence of very thin water layers in CALCCO_Lw_low, thereby diminishing the divergence between the two simulations.

Formatted: Don't keep with next
Formatted: Font: 10 pt, Not Bold
Formatted: Font: 10 pt, Not Bold
Formatted: Space After: 0 pt
Formatted Table
Formatted: Font: 10 pt, Not Bold
Formatted: Font: 10 pt, Not Bold
Formatted: Font: 10 pt, Not Bold
Formatted: Font: 10 pt, Not Bold
Formatted: Space After: 0 pt
Formatted: Font: 10 pt, Not Bold
Formatted: Font: 10 pt, Not Bold
Formatted: Font: 10 pt, Not Bold
Formatted: Space After: 0 pt
Formatted: Font: 10 pt, Not Bold
Formatted: Font: 10 pt, Not Bold
Formatted: Font: 10 pt, Not Bold
Formatted: Space After: 0 pt
Formatted: Font: 10 pt, Not Bold
Formatted: Font: 10 pt, Not Bold
Formatted: Font: 10 pt, Not Bold
Formatted: Space After: 0 pt
Formatted: Space After: 0 pt
Formatted: Space After: 0 pt
Formatted: Space After: 0 pt

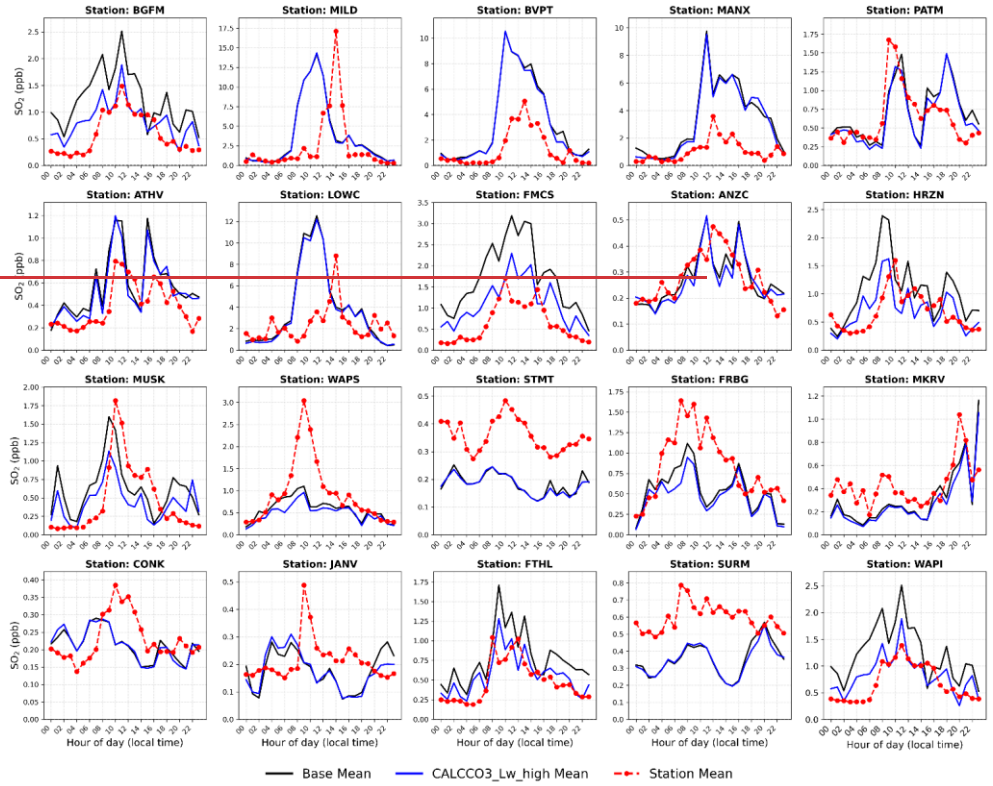

Figure 11: ~~The mean diurnal cycle of SO_2 measured at WBEA continuous monitoring stations (red dashed line) given in local time. The data are for the month of June 2018. Also shown are the model predicted mean SO_2 surface concentrations at the same location. The black line is the Base Case, while the blue line is CALCCO3_Lw_high. Note that due to plotting limitations the WBEA station 'FTCH' is not included in the figure.~~

~~. Each plot shows observations (red dashed line), the Base Case (black line) and CALCCO3_Lw_high (blue line). Identical plots for May, July and August 2018 are provided in the supplemental material (Figures S4, S5, S6, respectively). In June, th~~Figure 11 presents Taylor diagrams for (a) July and (b) Aug 2018 (see Supplement Figure S10 for May and June); these summarize graphically how closely modelled surface SO_2 concentrations match observations (Taylor, 1991). The diagrams simultaneously depict three key statistics: the correlation coefficient, the centred root-mean square difference (CRMS), and the standard deviation (amplitude of variation). ~~Figure 12 presents Taylor diagrams for (a) May, (b) June, (c) July and (d) Aug 2018, which summarize graphically how closely modelled surface SO_2 concentrations match observations (Taylor, 1991). These diagrams simultaneously depict three key statistics: the correlation coefficient, the centred root-mean square difference (CRMS), and the standard deviation (amplitude of variation). The equation used to compute these metrics are provided in Table S2. In each panel, the "star" symbol on x-axis marks the reference point for a perfect model, corresponding to a correlation = 1.0, a CRMS = 1.0 and a normalized standard deviation = 1.0. Arrows illustrate changes in model performance from the Base Case (arrow start) to CALCCO3_Lw_high (arrow end). A trajectory that moves closer to the reference point indicates improved agreement with observations.~~

~~The CRMS is proportional to the distance from the star; concentric circles centred on the star represent contours of constant CRMS. The standard deviation is measured radially from the origin.~~ In this work, both model and observed values are

normalized by the observed standard deviation, giving a normalized standard deviation. This implies that the observations always have a standard deviation of 1.0, marked as a black dashed line (semicircle) at a radius of 1.0 on each plot. Arrows that move closer to this dashed line indicate improved agreement in the amplitude of variation. The azimuthal angle represents the correlation, increasing clockwise from 0.0 to 1.0. To aid interpretation, the normalized mean bias (NMB) for each station is listed in the legend as (Base Case → CALCCO3). Red text and red arrows highlight stations where CALCCO3_Lw_high produces a better NMB than the Base Case. Black arrows indicate no improvement or a deterioration in the NMB. A general result of the comparison is that NMB values "shift towards negative numbers" – that is, all NMB values are decreasing. For stations where the base case NMB was positive this usually results in a smaller magnitude positive or negative NMB (red tabulated numbers), and for stations where the base case NMB was negative, the NMB becomes more negative (black tabulated numbers). Additional factors aside from the pH effect studied here are therefore likely to result in the remaining station-to-station variations in NMB. The results show that CALCCO3_Lw_high improves the standard deviation at several stations compared to the Base Case, especially in June (e.g. ~~i.e.~~, at BGFM, HRZN, FMCS, FTCH, FTHL, LOWC) and even more so in August, where all stations except BVPT, ANZC, MKRV and WAPS show improvement. In contrast, July exhibits mostly a deterioration in the standard deviation (see Supplement Figure S10), with many arrows pointing away from the reference line at 1.0, indicating poorer agreement with observed variability.

Formatted: Font color: Text 1

Despite modest to large statistical improvements in NMB in May, June, July and ~~and~~ August at some stations, substantial discrepancies remain between modelled and observed surface SO_2 concentrations, particularly in the form of low correlation coefficients (i.e., correlation $\ll 1.0$). While dry deposition plays a key role in determining the surface SO_2 concentrations in GEM-MACH, other factors may~~are~~ also contribute significantly to correlation, including:

i. the accuracy of meteorological variables predicted by GEM (i.e., air temperature, wind speed and direction, boundary-layer stability, precipitation occurrence and timing),

ii. the accuracy of SO_2 point-source emissions, including stack parameters required for plume rise calculations, as well as the fidelity of the plume rise algorithm itself (~~i.e.,~~ Fathi et al, 2025),

iii. chemical transformation of SO_2, particularly the aqueous-phase oxidation to sulphate in cloud droplets or within emission plumes, along with the cloud to rain conversion process governing wet deposition, and

iv. the effect of model grid resolution (Russell et al., 2019) which dilutes point-source emissions over much broader areas, smoothing out localized gradients.~~.~~

In addition to the factors listed above, instrumental limitations in the observations must also be considered. WBEA monitors employ continuous SO_2 analysers that are subject to a trace detection limit of 0.2 ppbv (AEP, 2014), below which concentrations are reported as zero. In contrast, GEM-MACH has no lower bound on predicted SO_2 concentrations, meaning it can simulate values that fall below the detection threshold and would therefore be recorded as below threshold in observations. Taken together, these points suggest that pH-modulated dry deposition alone cannot fully reconcile the modelled and observed SO_2 concentrations. However, as demonstrated in Fig. 1~~1~~2, the implementation of CALCCO3_Lw_high yields improvements in the NMB, and trajectories indicating improvements for correlation coefficient, CRMS, and standard deviation, for many stations.

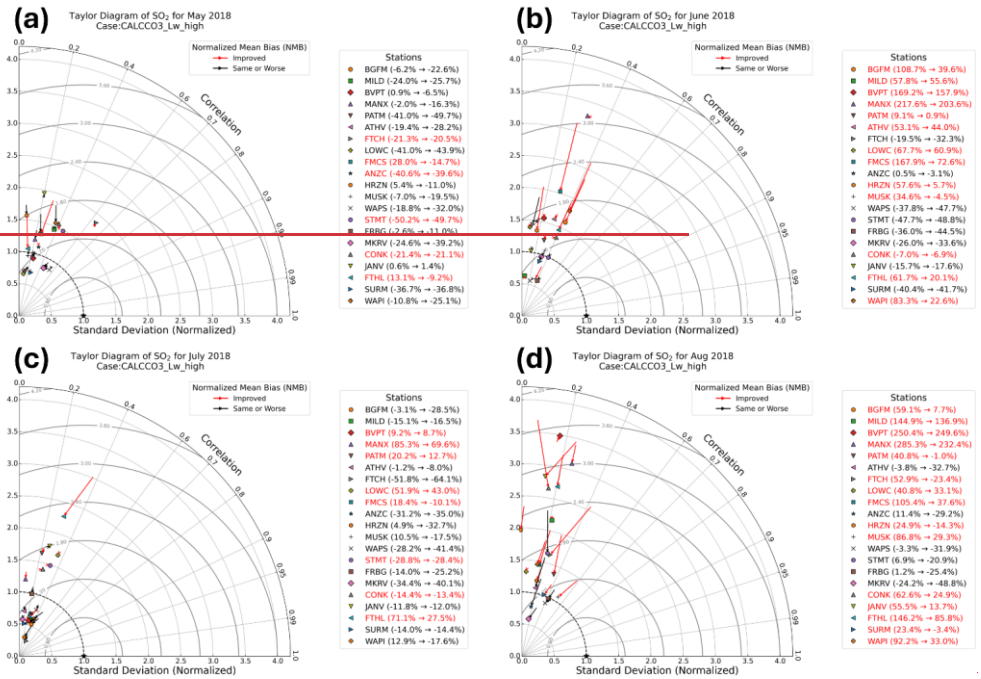

Formatted: Centered

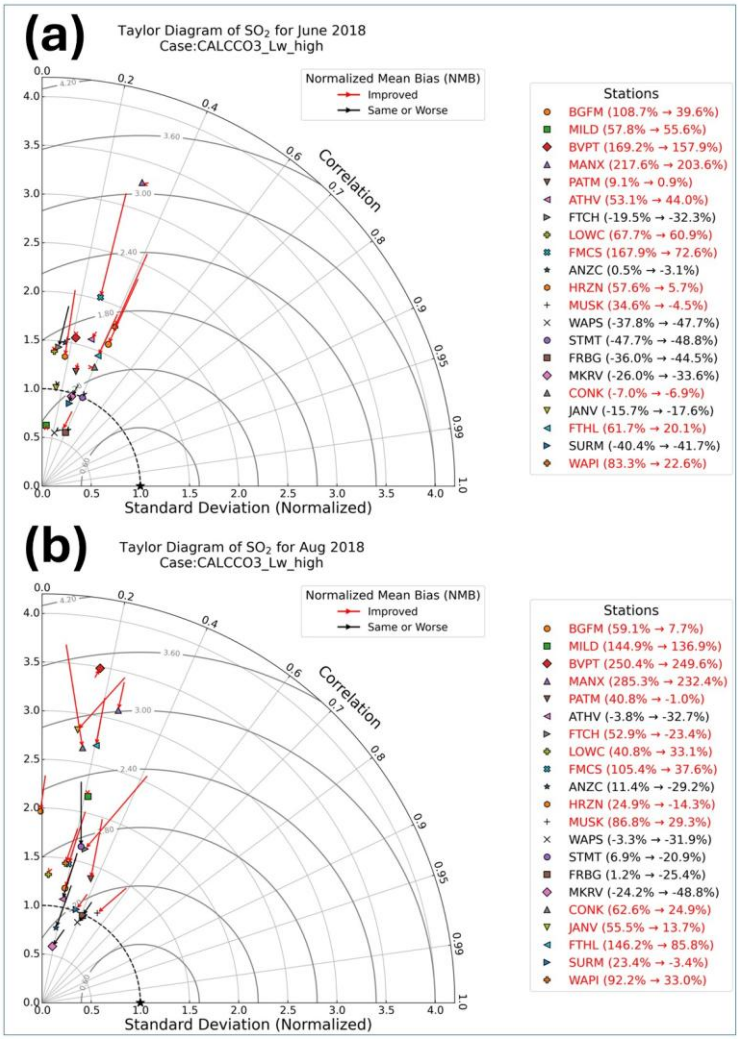

Figure ~~12~~11: Taylor Diagram of SO_2 for (a) ~~May 2018, (b)~~ June 2018, ~~(c) July 2018 and (d)~~(b) Aug 2018 (see Figure S10 for May and July). ~~.~~ The equations used to compute these metrics are provided in Table S3. In each panel, the "star" symbol on x-axis marks the reference point for a perfect model, corresponding to a correlation = 1.0, a CRMS = 1.0 and a normalized standard deviation = 1.0. Arrows illustrate changes in model performance from the Base Case (arrow start) to CALCCO3_Lw_high (arrow end). A trajectory that moves closer to the reference point indicates improved agreement with observations (red arrows). The CRMS is proportional to the distance from the star; concentric circles centred on the star represent contours of constant CRMS. The standard deviation is measured radially from the origin. The different WBEA stations are denoted by different symbols, with each arrow pointing from the Base Case to CALCCO3_Lw_high locations of station performance on the diagram. Red (black) arrows denote an improvement (deterioration or no change) in the normalized mean bias error (NMB) for CALCCO3_Lw_high compared to the Base Case. The value of the NMB for each station is shown in the legend after the station name as (Base Case → CALCCO3_Lw_high), with red text likewise representing improvements in the NMB when using CALCCO3_Lw_high compared to the Base Case. The azimuthal distance represents the correlation (i.e., r) starting from 0.0 and increasing clockwise to 1.0. The radial distance from the origin gives the normalized standard deviation of the model at the station. Each station standard deviation has been normalized by the observed standard deviation at that station. Thus, the observed standard deviation is always at (1.0, 1.0) ~~and this is~~ represented by ~~the~~a star on each plot. May and July Taylor diagrams are given in the Supplement, Figure S10.

Figure 12 presents Taylor diagrams for (a) May, (b) June, (c) July and (d) Aug 2018, which summarize graphically how closely modelled surface SO_2 concentrations match observations (Taylor, 1991). These diagrams simultaneously depict three key statistics: the correlation coefficient, the centred root-mean square difference (CRMS), and the standard deviation (amplitude of variation). The equation used to compute these metrics are provided in Table S2. In each panel, the "star" symbol on x-axis marks the reference point for a perfect model, corresponding to a correlation = 1.0, a CRMS = 1.0 and a normalized standard deviation = 1.0. Arrows illustrate changes in model performance from the Base Case (arrow start) to CALCCO3_Lw_high (arrow end). A trajectory that moves closer to the reference point indicates improved agreement with observations.

5.4 SO_2 dry deposition flux

Figure 13 shows the dry deposition flux of SO_2 (DSO_2) following the same layout as Fig. 8. As outlined in Sect. 2, DSO_2 is the calculated as the product of $V_{d_{SO_2}}$ and the surface SO_2 concentration. Thus, increases in $V_{d_{SO_2}}$ only translate to increased DSO_2 where appreciable surface SO_2 concentrations are present. Where SO_2 is available, however, higher $V_{d_{SO_2}}$ will proportionally increase DSO_2, all else being equal. Accordingly, the largest absolute increases in DSO_2 under CALCCO3_Lw_high occur in the AOSR, where elevated $V_{d_{SO_2}}$ (> 2 cm s^{-1}; Fig. 8) coincide with elevated surface SO_2 concentrations (> 2 ppb; Fig. 10). Since SO_2 emissions are identical in both simulations, the increased flux is entirely attributable to changes in $V_{d_{SO_2}}$ predicted by CALCCO3_Lw_high. In the AOSR, CALCCO3_Lw_high predicts DSO_2 values that are 2.5 to 10 times greater than those of the Base Case. This enhancement is consistent with aircraft-based measurements reported by Hayden et al., (2021), who found that GEM-MACH, lacking the pH $V_{d_{SO_2}}$ enhancement, underpredicted the dry deposition flux of total oxidized sulphur (TOS) by 2 to 14 times. While TOS measured in their study also included particulate sulphate, over 92 % of TOS their campaign was in the form of gaseous SO_2 making it reasonably representative of $V_{d_{SO_2}}$. Further downwind, particularly beyond 100 km from the AOSR, DSO_2 is reduced relative to the Base Case by up to 40%, especially in May. This reduction arises from enhanced dry deposition of SO_2 in the forests immediately downwind of sources, which depletes the SO_2 available for further transport and deposition. Additionally, these more remote regions receive much less base cation input, resulting in acidic foliage water layers (see Fig. 7), which further suppresses SO_2 dry deposition. Of these two contributing factors – (1) depletion of SO_2 from upwind deposition and (2) local inhibition of deposition to acidic foliage conditions – the latter likely dominates. The conclusion is supported by the spatial patterns: in regions where DSO_2 is reduced under CALCCO3_Lw_high (Fig 13g-i), surface SO_2 concentrations are increased relative to the Base Case, particularly in May (Fig 10g-i) – this occurs despite enhanced SO_2 removal to forests just upwind.

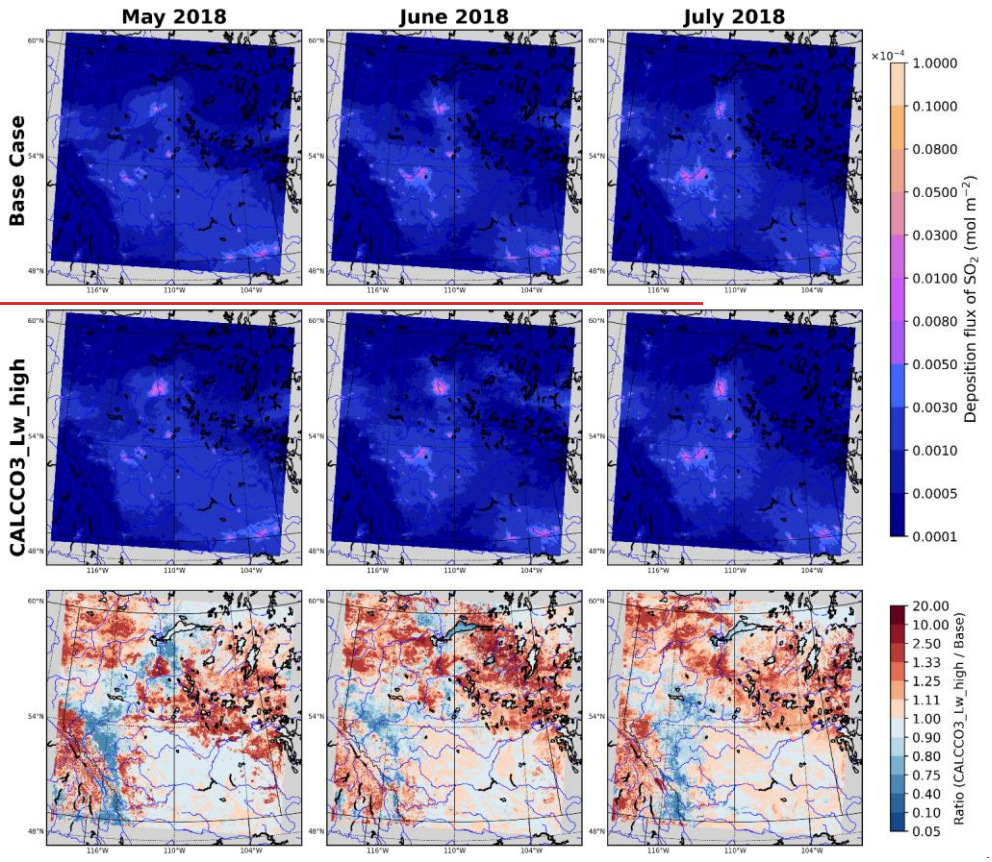

Figure 13: Identical to Fig 8, except now the plots show the deposition flux of SO_2.

6. Uncertainties and Observation Needs

While we have identified the potential for base cation co-deposition to significantly influence SO_2 deposition velocities and fluxes, there are several potential sources of uncertainty in this work, meriting further research. Many of these would require the collection of new observation data in order to be resolved. Several assumptions or omissions in our model reflect these potential uncertainties in the prediction of foliage pH and its effect on the SO_2 dry deposition velocity. Key limitations include:

1. Bulk canopy treatment: The foliage pH is modelled as a single value per grid cell, despite field observations showing strong vertical variability within a single forest stand (Fritsche, 1992)
2. Simplified particle deposition: The particle collection efficiency $\eta_{veg_{sp}}$ depends only on the LAI and particle size, omitting effects of species-specific leaf morphology such as hairs, roughness and waves (Pryor et al., 2013, Gronholm et al., 2009; Donat and Ruck 1999).
3. Leaf-surface microclimate simplification: The near-leaf relative humidity is likely elevated due to transpiration and boundary-layer effects (Boulard et al., 2002), but the model uses the ambient relative humidity to drive pH calculations. This may underestimate the water liquid water content on foliage where hygroscopic aerosols are present, affecting the ionic strength, and hence predicted pH of the leaf water layer on foliage (Tredenick et al., 2022; Coopman 2021; Katata and Held 2021; Burkhardt et al. 1999; Eiden et al., 1994).
4. Water and particle retention on foliage: The model does not account for the foliage water holding capacity (Wohlfahrt et al., 2006; Bradley et al., 2003; Brewer and Smith 1997; Sellers et al., 1986) or the PM retention capacity (Zheng and Peng, 2019; Chen et al., 2017) of the foliage. Neglecting the leaf water holding capacity may result in 'false' washoff events during light precipitation where the leaf water holding capacity is not exceeded (i.e., no actual washoff occurs).
5. Wet deposition simplification: Wet deposition was excluded from foliage pH calculations, assuming that during precipitation only the removal of soluble dry deposition mass from foliage occurs. Given sufficient precipitation, complete washoff is assumed, resetting accumulators to near-zero and yielding near-neutral pH. However, this likely overestimates pH during and immediately after the precipitation event, as most precipitation has pH < 6 (Vet et al., 2014 and references therein). Wet deposition retention on leaves is poorly constrained due to limited data on how much precipitation mass is retained by foliage. Observational data from Fort McMurray (AOSR) indicate that measurable precipitation was rare (≤0.07% of the time between May–August 2018), supporting the assumption that dry deposition dominates pH modulation in this region. Nonetheless, the simplification may not hold in wetter environments or during/after rain events, when wet deposition can transiently alter leaf surface chemistry.
6. Unmodelled surface chemistry: Processes such as SO_2 oxidation in the water layer boundary via soluble oxidants such as H_2O_2 (Chameides, 1987), organic acid buffering (Shigihara et al., 2008; Rogge et al., 1993; Tukey, 1966), foliar leaching (Tukey, 1966; Adams and Hutchinson 1984; Adams and Hutchinson, 1987; Potter 1990; Scherbatskoy and Tyree 1989; Kohno et al 2001) and bi-directional exchange (Wang et al., 2010; Massad et al., 2010; Flechard et al., 1999) are neglected.
7. Non-precipitation water sources: Fog, dew, and leaf guttation contribute to foliar moisture (Sect. 3). Dew adds only water, whereas guttation and fog can also deposit particle mass. Potential washoff due to dripping from these sources is neglected, and mass deposition from fog and guttation is ignored. Observational data show fog was rare (<0.02% of the May to August 2018 period in the AOSR), supporting the assumption that these additional sources of wet removal are minimal in this region.
8. No particle resuspension: Particle resuspension from foliage due to wind shear is highly variable and depends on wind conditions, canopy structure, and leaf morphology (see Sect 1). Due to these uncertainties and the likelihood that

Formatted: Left, Line spacing: single

Formatted: Subscript

resuspended particles remain within the same model grid cell, wind-driven resuspension was not explicitly included in this study's deposition algorithm.

9. Resistance parameter uncertainty: the boundary layer resistance R_b and the aerodynamic resistance R_a are fixed based on literature parametrizations. Inaccuracies in these terms could contribute to model-observation discrepancies in V_d even in the absence of a pH feedback effect (Hayden et al., 2021).
10. Other: other sources of uncertainty include chemical aging of foliage, model emission errors (e.g., wildfires), unmodeled surfaces such as bark, and the impact of insects and microbes.

Having identified several key uncertainties and limitations associated with this work, particularly surrounding the prediction of foliage pH, which directly modulates $V_{d_{SO_2}}$, we note that the level of uncertainty in simulating foliage pH is high due to the many poorly constrained biological, chemical, and physical processes that influence it. To improve the parameterization described in Sect. 3, a comprehensive and targeted suite of *in-situ* observations is needed. These observations should span a range of vegetation types, canopy structures, and environmental conditions to be broadly representative. Some specific data needs include:

1. Measurements of the vertical variation of foliage pH within canopies. Since canopy-level pH is currently treated as a bulk value, vertical profiles of leaf-surface [H^+] at different heights within the canopy are needed to determine whether a layered or height-dependent approach is more appropriate.
2. Measurements of particle collection efficiency $\alpha_{cut_{psp}}$ across multiple plant forest types are needed to refine deposition estimates (currently the only factor considered is leaf area index).
3. Measurements of the chemical composition of leaf surface water layers. *In-situ* sampling of thin water films for ionic composition (including base cations, nitrate, sulfate, and organic acids/bases) would help validate the HETP and CALCCO3 chemical modules and constrain assumptions about neglected organic species.
4. Measurements of particle mass and chemical composition deposited on to foliage via fog and guttation are needed to assess whether this process is significant.
5. While lab-based estimates of leaf water holding capacity help determine the potential for retention, what is critically needed are field observations of actual washoff events across a range of plant species, canopy structures, and rainfall intensities. These should quantify both the timing and chemical composition of material removed from foliage during precipitation. Such data would help determine when light rainfall leads to retention versus wash-off of deposited material and would inform improvements to model algorithms that currently rely on oversimplified thresholds. Ideally, these measurements would capture (1) the onset of washoff relative to cumulative rainfall, (2) the fraction of dry-deposited mass removed, (3) variability by leaf type and canopy exposure, and (4) how the chemical composition of washoff differs from precipitation input.
6. Wind tunnel and in-situ field studies measuring resuspension rates across wind regimes, canopy densities, and species types would help quantify the extent to which resuspended mass remains in-canopy opposed to being deposited to the ground.
7. Finally, it is imperative that whenever dry deposition velocities of SO_2 are inferred from *in-situ* measurements (whether by flux towers or aircraft campaigns) a complementary characterization of the foliage is conducted. This includes not only direct quantification of leaf wetness (e.g., via electrical conductance) but also measurements of the pH of the thin aqueous layers on the foliage. Without such information, it is difficult to interpret SO_2 deposition estimates or validate model predictions with confidence.

Formatted: Indent: First line: 0 cm

~~7.~~ Conclusions

7.

Despite the above uncertainties, this work has shown that the deposition of base cations to the forests downwind of the AOSR can modify the pH of thin water layers present on the foliage, and that these modifications can have significant local impacts on SO_2 deposition velocities, concentrations and deposition fluxes. For example, forests immediately downwind of the AOSR often have foliage water layers with a pH exceeding 7.5, while further downwind forests have foliage that is more acidic (pH < 5.0) since the co-deposition of base cations and gaseous SO_2 no longer occurs in significant amounts. Incorporating a pH feedback effect into the dry deposition code (specifically by allowing the predicted foliage pH to modify the effective Henry's law constant for SO_2) results in an increase of $V_{d_{SO_2}}$ in the AOSR by 2.5 to 10x (relative to a Base Case without any feedback effect). This increase brings modelled $V_{d_{SO_2}}$ in the range of observations (ground-based and aircraft) made in the vicinity of the facilities, where the mean $V_{d_{SO_2}}$ often exceeds 2 cm s^{-1} during the afternoon.

The impact of modifying $V_{d_{SO_2}}$ is also evident in the predicted mean monthly SO_2 surface concentrations and the monthly mean SO_2 dry deposition flux (Figs. 6-8(c), Supplement Figs. S3-S6~~10~~); ~~and mean daily SO_2 dry deposition flux (Fig. 13);~~ the former of which has decreased by up to 0.75 ppb (representing a decrease of up to 60%) while the latter has increased by 2.5 to 10 times. This decrease in the surface SO_2 concentrations represents an overall improvement to the model performance when the pH feedback effect is included, particularly in June and August. This improvement is represented in the statistical metrics calculated at the individual WBEA stations, especially a~~ts~~ stations BGFM, FMCS, HRZN, MUSK, FTHL and WAPI, but can also be seen over large areas as a greater than factor of two change in deposition flux.~~.~~

While these results have focused on a region with a combination of base cation emissions from anthropogenic fugitive dust and anthropogenic SO_2 emissions, we note that base cation deposition fluxes from natural sources may be very large, and are known to result in significant base cation deposition flux far downwind (in downwind continents from those with the emissions – Sahara and Asian dust events). Our results here suggest that forest fires are one such source of significant base cation emissions and deposition with large impacts on pH-modulated co-deposition of SO_2. We also note that a recent comparison of ensembles of regional air-quality models carrying out simulations for North American and European domains have shown that many models have positive biases of SO_2 in these regions, particularly at more remote sites, suggesting a need for a missing SO_2 loss mechanism (Makar et al., 2025), potentially ~~here filled~~filled here by base-cation co-deposition and SO_2 deposition enhancement due to pH effects.

Formatted: List Paragraph, Outline numbered + Level: 1 + Numbering Style: 1, 2, 3, … + Start at: 7 + Alignment: Left + Aligned at: 0.63 cm + Tab after: 1.27 cm + Indent at: 1.27 cm

Formatted: Subscript

Formatted: Subscript

Formatted: Subscript

8 Code availability

The GEM-MACH model code used in this work is available through Zenodo (Miller *et al.*, 2025): https://doi.org/10.5281/zenodo.17989573

9 Data Availability

Observation data used in this work are publicly available via the website of the Wood Buffalo Environmental Association (https://wbea.org/wp-content/uploads/2023/02/WBEA-Data-Access-Jan-2023.pdf)

10 Author Contributions

SJM led the project, developed the initial methodology, implemented the model code, ran all simulations, compiled the results, and created the figures. He also wrote the manuscript. PM contributed substantially to the development of the initial planning and conceptualization of the study (i.e., the study methodology) and provided detailed feedback and revisions to the entire manuscript. KT and CL provided significant input on the study's methodological design and contributed to the refinement of the manuscript. VSJ supported the initial model setup, assisted with code implementation, and helped identify and resolve technical issues during development. SF configured and provided the model code and simulation suite for the base-case (control case). SF and MM provided Python-based code support essential for generating graphical outputs. KH contributed to the initial planning and conceptualization of the study.

11 Competing interests

The authors declare that they have no conflict of interest.

12 Acknowledgements

This work was partially funded under the Oil Sands Monitoring (OSM) Program. It is independent of any position of the OSM Program.

13 Financial support

This research has been supported by the Environment and Climate Change Canada (grant no. Oil Sands Monitoring (OSM) Program, subproject "Integrated Atmospheric Deposition", A-PD-6-2324).

14 References

Adams, C. M., and Hutchinson, T. C. (1984). A comparison of the ability of leaf surfaces of three species to neutralize acidic rain drops. New Phytologist, 97(3), 463–478. https://doi.org/10.1111/j.1469-8137.1984.tb03612.x

Adams, C. M., & Hutchinson, T. C. (1987). Comparative abilities of leaf surfaces to neutralize acidic raindrops. II. the influence of leaf wettability, leaf age and rain duration on changes in droplet pH and chemistry on leaf surfaces. New Phytologist, 106(1), 437–456. https://doi.org/10.1111/j.1469-8137.1987.tb00124.x

Adema, E. H., & Heeres, P. (1995). Dry deposition of sulphur dioxide and ammonia on wet surfaces and the surface oxidation kinetics of bisulphite. Atmospheric Environment, 29(10), 1091–1103. https://doi.org/10.1016/1352-2310(95)00039-2

Alberta Environment and Parks (AEP): Development of Performance Specifications for Continuous Ambient Air Monitoring Analyzers, Government of Alberta, AEP, Alberta, Canada, 2014.

Avila, A., Alarcón, M., & Queralt, I. (1998). The chemical composition of dust transported in Red Rains—its contribution to the biogeochemical cycle of a Holm Oak Forest in Catalonia (Spain). Atmospheric Environment, 32(2), 179–191. https://doi.org/10.1016/s1352-2310(97)00286-0

Barker, M. G., & Ashenden, T. W. (1992). Effects of acid fog on cuticular permeability and cation leaching in holly (ilex aquifolium). Agriculture, Ecosystems & Environment, 42(3–4), 291–306. https://doi.org/10.1016/0167-8809(92)90005-v

Beckett, K. P., Freer-Smith, P. H., & Taylor, G. (2000). Particulate pollution capture by urban trees: Effect of species and Windspeed. Global Change Biology, 6(8), 995–1003. https://doi.org/10.1046/j.1365-2486.2000.00376.x

Beckett, K. P., Freer-Smith, P. H., & Taylor, G. (1998). Urban woodlands: Their role in reducing the effects of particulate pollution. Environmental Pollution, 99(3), 347–360. https://doi.org/10.1016/s0269-7491(98)00016-5

Berger, T. W., Eagar, C., Likens, G. E., & Stingeder, G. (2001). Effects of calcium and aluminum chloride additions on foliar and throughfall chemistry in Sugar Maples. Forest Ecology and Management, 149(1–3), 75–90. https://doi.org/10.1016/s0378-1127(00)00546-6

Beysens, D., Mongruel, A., & Acker, K. (2017). Urban dew and rain in Paris, France: Occurrence and physico-chemical characteristics. *Atmospheric Research*, *189*, 152–161. https://doi.org/10.1016/j.atmosres.2017.01.013

Beysens, D., Ohayon, C., Muselli, M., & Clus, O. (2006). Chemical and biological characteristics of dew and rain water in an urban coastal area (Bordeaux, France). Atmospheric Environment, 40(20), 3710–3723. https://doi.org/10.1016/j.atmosenv.2006.03.007

Boulard, T., Mermier, M., Fargues, J., Smits, N., Rougier, M., & Roy, J. C. (2002). Tomato leaf boundary layer climate: Implications for microbiological whitefly control in greenhouses. Agricultural and Forest Meteorology, 110(3), 159–176. https://doi.org/10.1016/s0168-1923(01)00292-1

Burkhardt, J., & Gerchau, J. (1994). A new device for the study of water vapour condensation and gaseous deposition to plant surfaces and particle samples. Atmospheric Environment, 28(12), 2012–2017. https://doi.org/10.1016/1352-2310(94)90470-7

Burkhardt, J., Koch, K., & Kaiser, H. (2001). Deliquescence of deposited atmospheric particles on leaf surfaces. *Water, Air, and Soil Pollution*, Focus 1, 313-321, https://doi.org/10.1007/978-94-010-9026-1_31

Burkhardt, J., Kaiser H., Goldbach, H., & Kappen, L. (1999). Measurements of electrical leaf surface conductance reveal re-condensation of transpired water vapour on leaf surfaces. Plant, Cell & Environment, 22(2), 189–196. https://doi.org/10.1046/j.1365-3040.1999.00387.x

Burkhardt, J. (1995). Hygroscopic salts on the leaf surface as a possible cause of forest decline symptoms. *Water, Air, & Soil Pollution*, *85*(3), 1245–1250. https://doi.org/10.1007/bf00477152

Burkhardt, J., & Eiden, R. (1990). The ion concentration of dew condensed on Norway spruce (picea abies (L.) karst.) and Scots pine (pinus sylvestris L.) needles. Trees, 4(1). https://doi.org/10.1007/bf00226236

Burkhardt, J., Flechard, C. R., Gresens, F., Mattsson, M., Jongejan, P. A., Erisman, J. W., Weidinger, T., Meszaros, R., Nemitz, E., & Sutton, M. A. (2009). Modelling the dynamic chemical interactions of atmospheric ammonia with leaf surface wetness in a managed grassland canopy. Biogeosciences, 6(1), 67–84. https://doi.org/10.5194/bg-6-67-2009

Burkhardt, J,, Basi, S., Pariyar, S., & Hunsche, M. (2012). Stomatal penetration by aqueous solutions – an update involving leaf surface particles. New Phytologist, 196(3), 774–787. https://doi.org/10.1111/j.1469-8137.2012.04307.x

Burkhardt, Jürgen, & Eiden, R. (1994). Thin water films on coniferous needles. Atmospheric Environment, 28(12), 2001–2011. https://doi.org/10.1016/1352-2310(94)90469-3

Burkhardt, J., & Hunsche, M. (2013). “breath figures” on leaf surfaces—formation and effects of microscopic leaf wetness. Frontiers in Plant Science, 4. https://doi.org/10.3389/fpls.2013.00422

Cadle, S. H., Marshall, J. D., & Mulawa, P. A. (1991). A laboratory investigation of the routes of HNO3 dry deposition to coniferous seedlings. Environmental Pollution, 72(4), 287–305. https://doi.org/10.1016/0269-7491(91)90003-f

Carlson, R. W., Bazzaz, F. A., Stukel, J. J., & Wedding, J. B. (1976). Physiological effects, wind reentrainment, and rainwash of lead aerosol particulate deposited on plant leaves. Environmental Science & Technology, 10(12), 1139–1142. https://doi.org/10.1021/es60122a001

Cape, J. N. (1993). Direct damage to vegetation caused by acid rain and polluted cloud: Definition of critical levels for forest trees. *Environmental Pollution*, *82*(2), 167–180. https://doi.org/10.1016/0269-7491(93)90114-4

Cape, J. N., Sheppard, L. J., Fowler, D., Harrison, A. F., Parkinson, J. A., Dao, P., & Paterson, I. S. (1992). Contribution of canopy leaching to sulphate deposition in a Scots Pine Forest. Environmental Pollution, 75(2), 229–236. https://doi.org/10.1016/0269-7491(92)90044-b

Chameides, W. L. (1984). The photochemistry of a Remote Marine Stratiform Cloud. Journal of Geophysical Research: Atmospheres, 89(D3), 4739–4755. https://doi.org/10.1029/jd089id03p04739

Chameides, W. L., & Stelson, A. W. (1992). Aqueous-phase chemical processes in Deliquescent Sea-salt aerosols: A mechanism that couples the atmospheric cycles of S and sea salt. Journal of Geophysical Research: Atmospheres, 97(D18), 20565–20580. https://doi.org/10.1029/92jd01923

Chameides, W. L. (1987). Acid Dew and the role of chemistry in the dry deposition of reactive gases to wetted surfaces. Journal of Geophysical Research: Atmospheres, 92(D10), 11895–11908. https://doi.org/10.1029/jd092id10p11895

Chen, L., Liu, C., Zhang, L., Zou, R., & Zhang, Z. (2017). Variation in tree species ability to capture and retain airborne fine particulate matter (PM2.5). Scientific Reports, 7(1). https://doi.org/10.1038/~~s4~~S51598-017-03360-1

Chiwa, M., Oshiro, N., Miyake, T., Nakatani, N., Kimura, N., Yuhara, T., Hashimoto, N., & Sakugawa, H. (2003). Dry deposition washoff and dew on the surfaces of pine foliage on the urban- and mountain-facing sides of Mt. Gokurakuji, Western Japan. Atmospheric Environment, 37(3), 327–337. https://doi.org/10.1016/s1352-2310(02)00889-0

Clarke, A. G., & Radojevic, M. (1987). Oxidation of SO2 in rainwater and its role in acid rain chemistry. *Atmospheric Environment (1967)*, *21*(5), 1115–1123. https://doi.org/10.1016/0004-6981(87)90238-1

Clifton, O. E., Schwede, D., Hogrefe, C., Bash, J. O., Bland, S., Cheung, P., Coyle, M., Emberson, L., Flemming, J., Fredj, E., Galmarini, S., Ganzeveld, L., Gazetas, O., Goded, I., Holmes, C. D., Horváth, L., Huijnen, V., Li, Q., Makar, P. A., … Zhang, L. (2023). A single-point modeling approach for the Intercomparison and evaluation of ozone dry deposition across chemical transport models (activity 2 of AQMEII4). Atmospheric Chemistry and Physics, 23(17), 9911–9961. https://doi.org/10.5194/acp-23-9911-2023

Coopman, R. E., Nguyen, H. T., Mencuccini, M., Oliveira, R. S., Sack, L., Lovelock, C. E., & Ball, M. C. (2021). Harvesting water from unsaturated atmospheres: Deliquescence of salt secreted onto leaf surfaces drives reverse sap flow in a dominant arid climate mangrove, avicennia marina. New Phytologist, 231(4), 1401–1414. https://doi.org/10.1111/nph.17461

Cox, R. M., Spavold-Tims, J., & Hughes, R. N. (1989). Acid fog and ozone: Their possible role in birch deterioration around the Bay of Fundy, Canada. *Water, Air, and Soil Pollution*, *48*(1–2). https://doi.org/10.1007/bf00282383

Dasch, J. M. (1989). Dry deposition of sulfur dioxide or nitric acid to oak, elm and Pine Leaves. Environmental Pollution, 59(1), 1–16. https://doi.org/10.1016/0269-7491(89)90018-3

Darley, E. F. (1966). Studies on the effect of cement-kiln dust on vegetation. Journal of the Air Pollution Control Association, 16(3), 145–150. https://doi.org/10.1080/00022470.1966.10468456

Dentener, F. J., Carmichael, G. R., Zhang, Y., Lelieveld, J., & Crutzen, P. J. (1996). Role of mineral aerosol as a reactive surface in the global troposphere. Journal of Geophysical Research: Atmospheres, 101(D17), 22869–22889. https://doi.org/10.1029/96jd01818

Donat, J., & Ruck, B. (1999). Simulated ground deposition of fine airborne particles in an array of idealized tree crowns. Boundary-Layer Meteorology, 93(3), 469–492. https://doi.org/10.1023/a:1002019623725

Draaijers, G. P. J., Erisman, J. W., Leeuwen, N. F. M. V., Römer, F. G., Winkel, B. H. T., Veltkamp, A. C., Vermeulen, A. T., & Wyers, G. P. (1997). The impact of canopy exchange on differences observed between atmospheric deposition and throughfall fluxes. Atmospheric Environment, 31(3), 387–397. https://doi.org/10.1016/s1352-2310(96)00164-1

Draaijers, G. P., Van Ek, R., & Bleuten, W. (1994). Atmospheric deposition in complex forest landscapes. Boundary-Layer Meteorology, 69(4), 343–366. https://doi.org/10.1007/bf00718124

Dutcher, C. S., Wexler, A. S., & Clegg, S. L. (2010). Surface tensions of inorganic multicomponent aqueous electrolyte solutions and melts. The Journal of Physical Chemistry A, 114(46), 12216–12230. https://doi.org/10.1021/jp105191z

Dzierżanowski, K., Popek, R., Gawrońska, H., Sæbø, A., & Gawroński, S. W. (2011). Deposition of particulate matter of different size fractions on leaf surfaces and in waxes of urban forest species. *International Journal of Phytoremediation*, *13*(10), 1037–1046. https://doi.org/10.1080/15226514.2011.552929

Eiden, R., Burkhardt, J., & Burkhardt, O. (1994). Atmospheric aerosol particles and their role in the formation of dew on the surface of plant leaves. Journal of Aerosol Science, 25(2), 367–376. https://doi.org/10.1016/0021-8502(94)90087-6

El Haber, M., Gérard, V., Kleinheins, J., Ferronato, C., & Nozière, B. (2024). Measuring the surface tension of atmospheric particles and relevant mixtures to better understand key atmospheric processes. Chemical Reviews, 124(19), 10924–10963. https://doi.org/10.1021/acs.chemrev.4c00173

Elleman, C. J., & Entwistle, P. F. (1982). A study of glands on cotton responsible for the high ph and cation concentration of the leaf surface. Annals of Applied Biology, 100(3), 553–558. https://doi.org/10.1111/j.1744-7348.1982.tb01422.x

Emerson, E. W., Hodshire, A. L., DeBolt, H. M., Bilsback, K. R., Pierce, J. R., McMeeking, G. R., & Farmer, D. K. (2020). Revisiting particle dry deposition and its role in radiative effect estimates. Proceedings of the National Academy of Sciences, 117(42), 26076–26082. https://doi.org/10.1073/pnas.2014761117

Erisman, J. W. (1994). Evaluation of a surface resistance parametrization of sulphur dioxide. *Atmospheric Environment*, *28*(16), 2583–2594. https://doi.org/10.1016/1352-2310(94)90432-4

Ervens, B., George, C., Williams, J. E., Buxton, G. V., Salmon, G. A., Bydder, M., Wilkinson, F., Dentener, F., Mirabel, P., Wolke, R., & Herrmann, H. (2003). Capram 2.4 (MODAC mechanism): An extended and condensed tropospheric aqueous phase mechanism and its application. Journal of Geophysical Research: Atmospheres, 108(D14). https://doi.org/10.1029/2002jd002202

Flechard, C. R., Fowler, D., Sutton, M. A., & Cape, J. N. (1999). A dynamic chemical model of BI-directional ammonia exchange between semi-natural vegetation and the atmosphere. Quarterly Journal of the Royal Meteorological Society, 125(559), 2611–2641. https://doi.org/10.1002/qj.49712555914

Foster, J. R., Pribush, R. A., & Carter, B. H. (1990). The chemistry of Dews and frosts in Indianapolis, Indiana. Atmospheric Environment. Part A. General Topics, 24(8), 2229–2236. https://doi.org/10.1016/0960-1686(90)90254-k

Fountoukis, C., & Nenes, A. (2007). ISORROPIA II: A computationally efficient thermodynamic equilibrium model for K+–ca2+–mg2+–nh4+–na+–so42−–no3−–cl−–h2O aerosols. Atmospheric Chemistry and Physics, 7(17), 4639–4659. https://doi.org/10.5194/acp-7-4639-2007

Fowler, D., Sutton, M.A., Flechard, C., Cape, J.N., Storeton-West, R., Coyle, M. and Smith, R.I. (2001). The control of SO_2 dry deposition on to natural surfaces by NH_3 and its effects on regional deposition. Water, Air, & Soil Pollution: Focus 1, 39–48. https://doi.org/10.1023/A:1013161912231

Fortmann, R. C., & Johnson, D. L. (1984). Effect of simulated rainfall on removal and in situ formation of particles on Taxus Needles. Environmental Pollution Series B, Chemical and Physical, 7(4), 297–316. https://doi.org/10.1016/0143-148x(84)90044-2

Freer-Smith, P. H., Beckett, K. P., & Taylor, G. (2005). Deposition velocities to Sorbus aria, Acer campestre, populus deltoides × trichocarpa 'beaupré', pinus nigra and × cupressocyparis leylandii for coarse, fine and ultra-fine particles in the urban environment. Environmental Pollution, 133(1), 157–167. https://doi.org/10.1016/j.envpol.2004.03.031

Fowler, D., & Unsworth, M. (1979). Turbulent transfer of sulphur dioxide to a wheat crop. *Quarterly Journal of the Royal Meteorological Society*, *105*(446), 767–783. https://doi.org/10.1256/smsqj.44602

Fritsche, U. (1992). Studies on leaching from spruce twigs and beech leaves. Environmental Pollution, 75(2), 251–257. https://doi.org/10.1016/0269-7491(92)90047-e

Fuentes, J. D., Gillespie, T. J., & Bunce, N. J. (1994). Effects of foliage wetness on the dry deposition of ozone onto Red Maple and Poplar leaves. Water, Air, and Soil Pollution, 74(1–2), 189–210. https://doi.org/10.1007/bf01257155

Galmarini, S., Makar, P., Clifton, O. E., Hogrefe, C., Bash, J. O., Bellasio, R., Bianconi, R., Bieser, J., Butler, T., Ducker, J., Flemming, J., Hodzic, A., Holmes, C. D., Kioutsioukis, I., Kranenburg, R., Lupascu, A., Perez-Camanyo, J. L., Pleim, J., Ryu, Y.-H., … Wolke, R. (2021). Technical note: AQMEII4 activity 1: Evaluation of wet and dry deposition schemes as an integral part of regional-scale air quality models. Atmospheric Chemistry and Physics, 21(20), 15663–15697. https://doi.org/10.5194/acp-21-15663-2021

Garland, J. A. (1977). The dry deposition of sulphur dioxide to land and water surfaces. Proc. R. Soc. Lond. A 354, 245-268. https://doi.org/10.1098/rspa.1977.0066

Gordon, A. G., & Gorham, E. (1963). Ecological aspects of air pollution from an iron-sintering plant at Wawa, Ontario. *Canadian Journal of Botany*, *41*(7), 1063–1078. https://doi.org/10.1139/b63-089

Gilbert, O. L. (1986). Field evidence for an acid rain effect on lichens. *Environmental Pollution Series A, Ecological and Biological*, *40*(3), 227–231. https://doi.org/10.1016/0143-1471(86)90097-8

Government of Alberta. (last access: June 30, 2025). *Oil sands facts and statistics*. Alberta.ca. https://www.alberta.ca/oil-sands-facts-and-statistics

Grace, J., & Wilson, J. (1976). The boundary layer over a*populus*leaf. *Journal of Experimental Botany*, *27*(2), 231–241. https://doi.org/10.1093/jxb/27.2.231

Grönholm, T., Launiainen, S., Ahlm, L., Mårtensson, E. M., Kulmala, M., Vesala, T., & Nilsson, E. D. (2009). Aerosol particle dry deposition to canopy and forest floor measured by two-layer eddy covariance system. Journal of Geophysical Research: Atmospheres, 114(D4). https://doi.org/10.1029/2008jd010663

Hames, R. S., Rosenberg, K. V., Lowe, J. D., Barker, S. E., & Dhondt, A. A. (2002). Adverse effects of acid rain on the distribution of the wood thrush*hylocichla mustelina*in North America. *Proceedings of the National Academy of Sciences*, *99*(17), 11235–11240. https://doi.org/10.1073/pnas.172700199

Hansen, K., Draaijers, G., Ivens, W., Gundersen, P., & Vanleeuwen, N. (1994). Concentration variations in rain and canopy throughfall collected sequentially during individual rain events. Atmospheric Environment, 28(20), 3195–3205. https://doi.org/10.1016/1352-2310(94)00176-l

Harr, J., Guggenheim, R., & Boller, T. (1984). High PH-values and secretion of ions on leaf surfaces: A characteristic of the phylloplane of Malvaceae. Experientia, 40(9), 935–937. https://doi.org/10.1007/bf01946445

Holloway, P. J. (1969). The effects of superficial wax on Leaf Wettability. *Annals of Applied Biology*, *63*(1), 145–153. https://doi.org/10.1111/j.1744-7348.1969.tb05475.x

Hovland, J., Abrahamsen, G., & Ogner, G. (1980). Effects of artificial acid rain on decomposition of spruce needles and on mobilisation and leaching of elements. Plant and Soil, 56(3), 365–378. https://doi.org/10.1007/bf02143031

Hughes, R. N., & Brimblecombe, P. (1994). Dew and guttation: Formation and environmental significance. Agricultural and Forest Meteorology, 67(3–4), 173–190. https://doi.org/10.1016/0168-1923(94)90002-7

Hutchinson, T. C., & Whitby, L. M. (1977). The effects of acid rainfall and heavy metal particulates on a boreal forest ecosystem near the Sudbury Smelting Region of Canada. *Water, Air, and Soil Pollution*, *7*(4). https://doi.org/10.1007/bf00285542

Hwang, H.-J., Yook, S.-J., & Ahn, K.-H. (2011). Experimental investigation of submicron and ultrafine soot particle removal by tree leaves. Atmospheric Environment, 45(38), 6987–6994. https://doi.org/10.1016/j.atmosenv.2011.09.019

Igawa, M., Kase, T., Satake, K., & Okochi, H. (2002). Severe leaching of calcium ions from fir needles caused by acid fog. Environmental Pollution, 119(3), 375–382. https://doi.org/10.1016/s0269-7491(01)00342-6

Irwin, J. G., & Williams, M. L. (1988). Acid rain: Chemistry and transport. *Environmental Pollution*, *50*(1–2), 29–59. https://doi.org/10.1016/0269-7491(88)90184-4

Jones, M. R., Raven, J. A., Leith, I. D., Cape, J. N., Smith, R. I., & Fowler, D. (2008b). Short-term flux chamber experiment to quantify the deposition of gaseous 15n-NH3 to calluna vulgaris. Agricultural and Forest Meteorology, 148(6–7), 893–901. https://doi.org/10.1016/j.agrformet.2007.12.003

Klemm, O., Riederer, M., & Frevert, T. (1987). PH-response on leaves and isolated cuticles of Hedera helix L. after wetting with artificial rainwater. Environmental and Experimental Botany, 27(3), 349–355. https://doi.org/10.1016/0098-8472(87)90045-1

Knabe, W. (1976). Effects of Sulphur Dioxide on Terrestrial Vegetation. Ambio, 5(5/6), 213–218. http://www.jstor.org/stable/4312219

Kohno, Y., Matsuki, R., Nomura, S., Mitsunari, K., & Nakao, M. (2001). Neutralization of acid droplets on plant leaf surfaces. Water, Air and Soil Pollution, 130, 977–982. https://doi.org/10.1007/978-94-007-0810-5_10

Konrad, W., Burkhardt, J., Ebner, M., & Roth-Nebelsick, A. (2014). Leaf pubescence as a possibility to increase water use efficiency by promoting condensation. Ecohydrology, 8(3), 480–492. https://doi.org/10.1002/eco.1518

Landis, M. S., Studabaker, W. B., Pancras, J. P., Graney, J. R., White, E. M., & Edgerton, E. S. (2019). Source apportionment of ambient fine and coarse particulate matter polycyclic aromatic hydrocarbons at the Bertha Ganter-Fort McKay community site in the Oil Sands Region of Alberta, Canada. Science of The Total Environment, 666, 540–558. https://doi.org/10.1016/j.scitotenv.2019.02.126

Leep, N. W., N. M. Dickinson (1976). The pH of leaf surfaces, and its modification by atmospheric pollution. Lauri Karenlampi (ed.): Proceedings of the Kuopio meeting on plant damages caused by air pollution, 138-139.

Lekouch, I., Mileta, M., Muselli, M., Milimouk-Melnytchouk, I., Šojat, V., Kabbachi, B., & Beysens, D. (2010). Comparative Chemical Analysis of dew and rain water. Atmospheric Research, 95(2–3), 224–234. https://doi.org/10.1016/j.atmosres.2009.10.002

Li, S.-M., Leithead, A., Moussa, S. G., Liggio, J., Moran, M. D., Wang, D., Hayden, K., Darlington, A., Gordon, M., Staebler, R., Makar, P. A., Stroud, C. A., McLaren, R., Liu, P. S., O'Brien, J., Mittermeier, R. L., Zhang, J., Marson, G., Cober, S. G., … Wentzell, J. J. (2017). Differences between measured and reported volatile organic compound emissions from oil sands facilities in Alberta, Canada. *Proceedings of the National Academy of Sciences*, *114*(19). https://doi.org/10.1073/pnas.1617862114

Lindberg, S. E., & Lovett, G. M. (1985). Field measurements of particle dry deposition rates to foliage and inert surfaces in a forest canopy. Environmental Science & Technology, 19(3), 238–244. https://doi.org/10.1021/es00133a003

Lovett, G. M., & Hubbell, J. G. (1991). Effects of ozone and acid mist on foliar leaching from eastern white pine and Sugar Maple. Canadian Journal of Forest Research, 21(6), 794–802. https://doi.org/10.1139/x91-112

Luo, J., Niu, Y., Zhang, Y., Zhang, M., Tian, Y., & Zhou, X. (2019). Dynamic Analysis of retention PM2.5 by plant leaves in rainfall weather conditions of six tree species. Energy Sources, Part A: Recovery, Utilization, and Environmental Effects, 42(8), 1014–1025. https://doi.org/10.1080/15567036.2019.1602212

Makar, P. A., Cheung, P., Hogrefe, C., Akingunola, A., Alyuz, U., Bash, J. O., Bell, M. D., Bellasio, R., Bianconi, R., Butler, T., Cathcart, H., Clifton, O. E., Hodzic, A., Kioutsioukis, I., Kranenburg, R., Lupascu, A., Lynch, J. A., Momoh, K., Perez-Camanyo, J. L., Pleim, J., Ryu, Y.-H., San Jose, R., Schwede, D., Scheuschner, T., Shephard, M. W., Sokhi, R. S., and Galmarini, S. (2025). Critical load exceedances for North America and Europe using an ensemble of models and an investigation of causes of environmental impact estimate variability: an AQMEII4 study, Atmos. Chem. Phys., 25, 3049–3107, https://doi.org/10.5194/acp-25-3049-2025

Mamun, A. A., Celo, V., Dabek-Zlotorzynska, E., Charland, J.-P., Cheng, I., & Zhang, L. (2021). Characterization and source apportionment of airborne particulate elements in the athabasca oil sands region. Science of The Total Environment, 788, 147748. https://doi.org/10.1016/j.scitotenv.2021.147748

Mandre, M., & Tuulmets, L. (1997). Pigment changes in Norway spruce induced by dust pollution. Water, Air, & Soil Pollution, 94(3–4), 247–258. https://doi.org/10.1007/bf02406061

Manning, W. J. (1971). Effects of limestone dust on leaf condition, foliar disease incidence, and leaf surface microflora of native plants. Environmental Pollution (1970), 2(1), 69–76. https://doi.org/10.1016/0013-9327(71)90038-3

Massad, R.-S., Nemitz, E., & Sutton, M. A. (2010). Review and Parameterisation of bi-directional ammonia exchange between vegetation and the atmosphere. Atmospheric Chemistry and Physics, 10(21), 10359–10386. https://doi.org/10.5194/acp-10-10359-2010

Meng, Z., Seinfeld, J. H., Saxena, P., & Kim, Y. P. (1995). Atmospheric gas-aerosol equilibrium: IV. thermodynamics of carbonates. Aerosol Science and Technology, 23(2), 131–154. https://doi.org/10.1080/02786829508965300

Miller, S. J., Makar, P. A., & Lee, C. J. (2024). Heterogeneous vectorized or parallel (HETPv1.0): An updated inorganic heterogeneous chemistry solver for the metastable-state NH4+–na+–ca2+–k+–mg2+–so42−–no3−–cl−–h2O system based on ISORROPIA II. Geoscientific Model Development, 17(6), 2197–2219. https://doi.org/10.5194/gmd-17-2197-2024

Miller, S. J., Makar, P., Toyota, K., Lee, C., Savic Jovcic, V., Fathi, S., Majdzadeh, M., & Hayden, K. (2025). Model code version for "Alkaline dust deposition to foliage surfaces likely enhances the dry deposition velocity of SO2: A modelling investigation in the Alberta Oil-Sands Region using the GEM-MACH air-quality model". Zenodo. https://doi.org/10.5281/zenodo.17989573

Mitterhuber, E., Pfanz, H., & Kaiser, W. M. (1989). Leaching of solutes by the action of acidic rain: A comparison of efflux from twigs and single needles of picea abies (L. karst.). Plant, Cell & Environment, 12(1), 93–100. https://doi.org/10.1111/j.1365-3040.1989.tb01920.x

Monteith, J. L. (1957). Dew. Quarterly Journal of the Royal Meteorological Society, 83(357), 322–341. https://doi.org/10.1002/qj.49708335706

Mori, J., Sæbø, A., Hanslin, H. M., Teani, A., Ferrini, F., Fini, A., & Burchi, G. (2015). Deposition of traffic-related air pollutants on leaves of six evergreen shrub species during a Mediterranean summer season. Urban Forestry & Urban Greening, 14(2), 264–273. https://doi.org/10.1016/j.ufug.2015.02.008

Munger, J. W., Jacob, D. J., Waldman, J. M., & Hoffmann, M. R. (1983). Fogwater Chemistry in an urban atmosphere. *Journal of Geophysical Research: Oceans*, *88*(C9), 5109–5121. https://doi.org/10.1029/jc088ic09p05109

Neinhuis, C., Koch, K., & Barthlott, W. (2001). Movement and regeneration of epicuticular waxes through plant cuticles. Planta, 213(3), 427–434. https://doi.org/10.1007/s004250100530

Neirynck, J., Flechard, C. R., & Fowler, D. (2011). Long-term (13 years) measurements of SO2 fluxes over a forest and their control by Surface Chemistry. Agricultural and Forest Meteorology, 151(12), 1768–1780. https://doi.org/10.1016/j.agrformet.2011.07.013

Nemitz, E., Milford, C., and Sutton, M. A. (2001). A two-layer canopy compensation point model for describing bi-directional biosphere-atmosphere exchange of ammonia, Quarterly Journal of the Royal Meteorological Society, 127, 573, 815–833. https://doi.org/10.1002/qj.49712757306

Oertil, J, J., Harr, J. and Guggenhein, R. (1977). The pH values as an indicator for the leaf surface microenvironment. Journal of Plant Diseases and Protection, 84, 729-737. https://www.jstor.org/stable/43213485

Odeh, I., Arar, S., Al-Hunaiti, A., Sa'aydeh, H., Hammad, G., Duplissy, J., Vuollekoski, H., Korpela, A., Petäjä, T., Kulmala, M., & Hussein, T. (2017). Chemical Investigation and quality of Urban dew collections with Dust Precipitates. Environmental Science and Pollution Research, 24(13), 12312–12318. https://doi.org/10.1007/s11356-017-8870-3

Ottelé, M., van Bohemen, H. D., & Fraaij, A. L. A. (2010). Quantifying the deposition of particulate matter on climber vegetation on living walls. Ecological Engineering, 36(2), 154–162. https://doi.org/10.1016/j.ecoleng.2009.02.007

Ould-Dada, Z., & Baghini, N. M. (2001). Resuspension of small particles from tree surfaces. Atmospheric Environment, 35(22), 3799–3809. https://doi.org/10.1016/s1352-2310(01)00161-3

Ould-Dada, Z, Copplestone, D., Toal, M., & Shaw, G. (2002). Effect of forest edges on deposition of radioactive aerosols. Atmospheric Environment, 36(36–37), 5595–5606. https://doi.org/10.1016/s1352-2310(02)00699-4

Pandis, S. N., & Seinfeld, J. H. (1989). Mathematical modeling of acid deposition due to radiation fog. *Journal of Geophysical Research: Atmospheres*, *94*(D10), 12911–12923. https://doi.org/10.1029/jd094id10p12911

Pfanz, H., Martinoia, E., Lange, O.-L., & Heber, U. (1987). Mesophyll resistances to so2 fluxes into leaves. Plant Physiology, 85(4), 922–927. https://doi.org/10.1104/pp.85.4.922

Pereira, P., Úbeda, X., & Martin, D. A. (2012). Fire severity effects on ash chemical composition and water-extractable elements. *Geoderma*, *191*, 105–114. https://doi.org/10.1016/j.geoderma.2012.02.005

Pereira, P., Úbeda, X., Martin, D., Mataix-Solera, J., Cerdà, A., & Burguet, M. (2013). Wildfire effects on extractable elements in ash from apinus pinasterforest in Portugal. Hydrological Processes, 28(11), 3681–3690. https://doi.org/10.1002/hyp.9907

Pio, C. A., & Feliciano, M. S. (1996). Dry deposition of ozone and sulphur dioxide over low vegetation in moderate southern European weather conditions. measurements and modelling. Physics and Chemistry of the Earth, 21(5–6), 373–377. https://doi.org/10.1016/s0079-1946(97)81126-3

Popek, R., Gawrońska, H., Wrochna, M., Gawroński, S. W., & Sæbø, A. (2013). Particulate matter on foliage of 13 woody species: Deposition on surfaces and phytostabilisation in waxes – a 3-year study. International Journal of Phytoremediation, 15(3), 245–256. https://doi.org/10.1080/15226514.2012.694498

Popek, R., Haynes, A., Przybysz, A., & Robinson, S. A. (2019). How much does weather matter? effects of rain and wind on PM accumulation by four species of Australian native trees. Atmosphere, 10(10), 633. https://doi.org/10.3390/atmos10100633

Potter, C. S. (1991). Nutrient leaching from *Acer rubrum* leaves by experimental acid rainfall. Canadian Journal of Forest Research, 21(2), 222–229. https://doi.org/10.1139/x91-027

Potter, C. S., & Ragsdale, H. L. (1991). Dry deposition Washoff from forest tree leaves by experimental acid rainfall. Atmospheric Environment. Part A. General Topics, 25(2), 341–349. https://doi.org/10.1016/0960-1686(91)90305-q

Proemse, B., Maynard, D., & Mayer, B. (2016). Foliage chemistry of pinus baksiana in the athabasca oil sands region, Alberta, Canada. Forests, 7(12), 312. https://doi.org/10.3390/f7120312

Przybysz, A., Sæbø, A., Hanslin, H. M., & Gawroński, S. W. (2014). Accumulation of particulate matter and trace elements on vegetation as affected by pollution level, rainfall and the passage of Time. Science of The Total Environment, 481, 360–369. https://doi.org/10.1016/j.scitotenv.2014.02.072

Puckett, L. J. (1990). Time- and ph-dependent leaching of ions from deciduous and coniferous foliage. Canadian Journal of Forest Research, 20(11), 1779–1785. https://doi.org/10.1139/x90-237

Pullman, M. R. (2009). Conifer $PM_{2.5}$ deposition and re-suspension in wind and rain events (MSc Thesis, Cornell University): https://ecommons.cornell.edu/server/api/core/bitstreams/c035123c-c2c2-4cde-a133-e77d23a25400/content, last accessed December 12, 2025.

Pye, H. O., Nenes, A., Alexander, B., Ault, A. P., Barth, M. C., Clegg, S. L., Collett Jr., J. L., Fahey, K. M., Hennigan, C. J., Herrmann, H., Kanakidou, M., Kelly, J. T., Ku, I.-T., McNeill, V. F., Riemer, N., Schaefer, T., Shi, G., Tilgner, A., Walker, J. T., … Zuend, A. (2020). The acidity of atmospheric particles and clouds. Atmospheric Chemistry and Physics, 20(8), 4809–4888. https://doi.org/10.5194/acp-20-4809-2020

Rafaï, S., Sarker, D., Bergeron, V., Meunier, J., & Bonn, D. (2002). Superspreading: aqueous surfactant drops spreading on hydrophobic surfaces. Langmuir, 18(26), 10486–10488. https://doi.org/10.1021/la020271i

Raynor, G. S., Hayes, J. V., & Ogden, E. C. (1974). Particulate dispersion into and within a forest. Boundary-Layer Meteorology, 7(4), 429–456. https://doi.org/10.1007/bf00568335

Rennenberg, H. (1984). The fate of excess sulfur in higher plants. Annual Review of Plant Physiology and Plant Molecular Biology, 35(1), 121–153. https://doi.org/10.1146/annurev.arplant.35.1.121

Rodríguez-Germade, I., Mohamed, K. J., Rey, D., Rubio, B., & García, Á. (2014). The influence of weather and climate on the reliability of magnetic properties of tree leaves as proxies for Air Pollution Monitoring. Science of The Total Environment, 468–469, 892–902. https://doi.org/10.1016/j.scitotenv.2013.09.009

Rogge, W. F., Hildemann, L. M., Mazurek, M. A., Cass, G. R., & Simoneit, B. R. (1993). Sources of fine organic aerosol. 4. particulate abrasion products from leaf surfaces of urban plants. Environmental Science & Technology, 27(13), 2700–2711. https://doi.org/10.1021/es00049a008

Rosado, B. H., & Holder, C. D. (2012). The significance of Leaf Water Repellency in Ecohydrological research: A Review. *Ecohydrology*, *6*(1), 150–161. https://doi.org/10.1002/eco.1340

Rosas, D., Silva, M. M., Figueroa, B., Morton-Bermea, O., Miranda, J., Alvarez, H., Puig, T. P., Morales, J., Uuh, J., Hernández-Alvarez, E., Novelo, S., Olivares, J., Salcedo, D., Rosas, I., Ponce, C., Raga, G. B., & Ladino, L. A. (2025). African dust particles over the western caribbean: Chemical characterization. Atmospheric Environment, 347, 121095. https://doi.org/10.1016/j.atmosenv.2025.121095

Russell, M., Hakami, A., Makar, P.A., Akingunola, A., Zhang, J., Moran, M.D., and Zheng, Q. (2019), An evaluation of the efficacy of very high resolution air-quality modelling over the Athabasca oil sands region, Alberta, Canada, Atm. Chem. Phys., 19, 4393-4417. https://doi.org/10.5194/acp-19-4393-2019

Sæbø, A., Popek, R., Nawrot, B., Hanslin, H. M., Gawronska, H., & Gawronski, S. W. (2012). Plant species differences in particulate matter accumulation on Leaf Surfaces. *Science of The Total Environment*, *427–428*, 347–354. https://doi.org/10.1016/j.scitotenv.2012.03.084

Sánchez-García, C., Santín, C., Neris, J., Sigmund, G., Otero, X. L., Manley, J., González-Rodríguez, G., Belcher, C. M., Cerdà, A., Marcotte, A. L., Murphy, S. F., Rhoades, C. C., Sheridan, G., Strydom, T., Robichaud, P. R., & Doerr, S. H. (2023). Chemical characteristics of wildfire ash across the globe and their environmental and socio-economic implications. Environment International, 178, 108065. https://doi.org/10.1016/j.envint.2023.108065

Savchenko, G., Wiese, C., Neimanis, S., Hedrich, R., & Heber, U. (2000). Ph regulation in apoplastic and cytoplasmic cell compartments of leaves. *Planta*, *211*(2), 246–255. https://doi.org/10.1007/s004250000280

Scherbatskoy, T., & Klein, R. M. (1983). Response of spruce and birch foliage to leaching by acidic mists. Journal of Environmental Quality, 12(2), 189–195. https://doi.org/10.2134/jeq1983.00472425001200020008x

Scherbatskoy, T., and Tyree, M. T (1990). Kinetics of exchange of ions between artificial precipitation and Maple Leaf Surfaces. New Phytologist, 114(4), 703–712. https://doi.org/10.1111/j.1469-8137.1990.tb00442.x

Scheuvens, D., Schütz, L., Kandler, K., Ebert, M., & Weinbruch, S. (2013). Bulk composition of northern African dust and its source sediments — a compilation. Earth-Science Reviews, 116, 170–194. https://doi.org/10.1016/j.earscirev.2012.08.005

Schier, G. A. (1987). Throughfall chemistry in a red maple provenance plantation sprayed with "acid rain." Canadian Journal of Forest Research, 17(7), 660–665. https://doi.org/10.1139/x87-108

Schindler, D. W., Kasian, S. E., & Hesslein, R. H. (1989). Losses of biota from American aquatic communities due to acid rain. *Environmental Monitoring and Assessment*, *12*(3), 269–285. https://doi.org/10.1007/bf00394806

Schuepp, P. H. (1993). Tansley Review no. 59 leaf boundary layers. *New Phytologist*, *125*(3), 477–507. https://doi.org/10.1111/j.1469-8137.1993.tb03898.x

Shi, Q., Davidovits, P., Jayne, J. T., Worsnop, D. R., & Kolb, C. E. (1999). Uptake of gas-phase ammonia. 1. uptake by aqueous surfaces as a function of ph. The Journal of Physical Chemistry A, 103(44), 8812–8823. https://doi.org/10.1021/jp991696p

Siqueira-Silva, A. I., Pereira, E. G., Modolo, L. V., Lemos-Filho, J. P., & Paiva, E. A. (2016). Impact of cement dust pollution on Cedrela Fissilis Vell. (Meliaceae): A potential bioindicator species. Chemosphere, 158, 56–65. https://doi.org/10.1016/j.chemosphere.2016.05.047

Shigihara, A., Matsumoto, K., Sakurai, N., & Igawa, M. (2008). Leaching of cell wall components caused by acid deposition on Fir Needles and trees. Science of The Total Environment, 398(1–3), 185–195. https://doi.org/10.1016/j.scitotenv.2008.03.007

Singh, S. (2016). Guttation: Mechanism, momentum and modulation. *The Botanical Review*, *82*(2), 149–182. https://doi.org/10.1007/s12229-016-9165-y

Sorteberg, A., & Hov, Ø. (1996a). Two parametrizations of the dry deposition exchange for SO2 and NH3 in a numerical model. Atmospheric Environment, 30(10–11), 1823–1840. https://doi.org/10.1016/1352-2310(95)00381-9

Sutton, M. A., Burkhardt, J. K., Guerin, D., Nemitz, E., & Fowler, D. (1998). Development of resistance models to describe measurements of bi-directional ammonia surface–atmosphere exchange. Atmospheric Environment, 32(3), 473–480. https://doi.org/10.1016/s1352-2310(97)00164-7

Taylor, K. E. (2001). Summarizing multiple aspects of model performance in a single diagram. Journal of Geophysical Research: Atmospheres, 106(D7), 7183–7192. https://doi.org/10.1029/2000jd900719

Taylor, G. E., McLaughlin, S. B., Shriner, D. S., & Selvidge, W. J. (1983). The flux of sulfur-containing gases to vegetation. Atmospheric Environment (1967), 17(4), 789–796. https://doi.org/10.1016/0004-6981(83)90428-6

Tiwary, A., Morvan, H. P., & Colls, J. J. (2006). Modelling the size-dependent collection efficiency of hedgerows for ambient aerosols. Journal of Aerosol Science, 37(8), 990–1015. https://doi.org/10.1016/j.jaerosci.2005.07.004

Tomson, M., Kumar, P., Abhijith, K. V., & Watts, J. F. (2024). Exploring the interplay between particulate matter capture, wash-off, and leaf traits in green wall species. Science of The Total Environment, 921, 170950. https://doi.org/10.1016/j.scitotenv.2024.170950

Tredenick, E. C., Stuart-Williams, H., & Enge, T. G. (2022). Materials on plant leaf surfaces are deliquescent in a variety of environments. Frontiers in Plant Science, 13. https://doi.org/10.3389/fpls.2022.722710

Tukey, H. B. (1966). Leaching of metabolites from above-ground plant parts and its implications. Bulletin of the Torrey Botanical Club, 93(6), 385. https://doi.org/10.2307/2483411

Turner, D. P., & van Broekhuizen, H. J. (1992). Nutrient leaching from conifer needles in relation to foliar apoplast cation exchange capacity. Environmental Pollution, 75(3), 259–263. https://doi.org/10.1016/0269-7491(92)90124-s

Turunen, M., & Huttunen, S. (1990). A review of the response of epicuticular wax of conifer needles to air pollution. Journal of Environmental Quality, 19(1), 35–45. https://doi.org/10.2134/jeq1990.00472425001900010003x

Unsworth, M., & Wilshaw. J. (1989). Wet, occult and dry deposition of pollutants on forests. Agricultural and Forest Meteorology, 47(2–4), 221–238. https://doi.org/10.1016/0168-1923(89)90097-x

Val Martin, M., Heald, C. L., & Arnold, S. R. (2014). Coupling dry deposition to vegetation phenology in the Community Earth System Model: Implications for the simulation of surface O3. Geophysical Research Letters, 41(8), 2988–2996. https://doi.org/10.1002/2014gl059651

Van Hove, L. W. A., Adema, E. H., Vredenberg, W. J., & Pieters, G. A. (1989). A study of the adsorption of NH_3 and SO_2 on leaf surfaces. Atmospheric Environment (1967), 23(7), 1479–1486. https://doi.org/10.1016/0004-6981(89)90407-1

Vet, R., Artz, R. S., & Carou, S. (2014). A global assessment of precipitation chemistry and deposition of sulfur, nitrogen, sea salt, base cations, organic acids, acidity and ph, and phosphorus. Atmospheric Environment, 93, 1–2. https://doi.org/10.1016/j.atmosenv.2013.11.013

Wang, X., Chow, J. C., Kohl, S. D., Percy, K. E., Legge, A. H., & Watson, J. G. (2015). Characterization of PM2.5 and pm10 fugitive dust source profiles in the athabasca oil sands region. *Journal of the Air & Waste Management Association*, *65*(12), 1421–1433. https://doi.org/10.1080/10962247.2015.1100693

Wang, H., Shi, H., & Wang, Y. (2015). Effects of weather, time, and pollution level on the amount of particulate matter deposited on leaves of ligustrum lucidum. The Scientific World Journal, 2015(1). https://doi.org/10.1155/2015/935942

Wang, W., Ganzeveld, L., Rossabi, S., Hueber, J., & Helmig, D. (2020). Measurement report: Leaf-scale gas exchange of atmospheric reactive trace species (no2, no, o3) at a Northern Hardwood Forest in Michigan. Atmospheric Chemistry and Physics, 20(19), 11287–11304. https://doi.org/10.5194/acp-20-11287-2020

Wang, Y., Zhuang, G., Sun, Y., & An, Z. (2005). Water-soluble part of the aerosol in the dust storm season—evidence of the mixing between mineral and pollution aerosols. Atmospheric Environment, 39(37), 7020–7029. https://doi.org/10.1016/j.atmosenv.2005.08.005

Weerakkody, U., Dover, J. W., Mitchell, P., & Reiling, K. (2018). The impact of rainfall in remobilising particulate matter accumulated on leaves of four evergreen species grown on a green screen and a living wall. Urban Forestry & Urban Greening, 35, 21–31. https://doi.org/10.1016/j.ufug.2018.07.018

Wesely, M. (1989). Parameterization of surface resistances to gaseous dry deposition in regional-scale numerical models. Atmospheric Environment, 23, 1293–1304. https://doi.org/10.1016/0004-6981(89)90153-4

Wesely, M. L., & Hicks, B. B. (1977). Some factors that affect the deposition rates of sulfur dioxide and similar gases on vegetation. Journal of the Air Pollution Control Association, 27(11), 1110–1116. https://doi.org/10.1080/00022470.1977.10470534

Wesely, M. L., Sisterson, D. L., & Jastrow, J. D. (1990). Observations of the chemical properties of dew on vegetation that affect the dry deposition of so2. Journal of Geophysical Research: Atmospheres, 95(D6), 7501–7514. https://doi.org/10.1029/jd095id06p07501

Wisniewski, J. (1982). The potential acidity associated with dews, frosts, and Fogs. Water, Air, and Soil Pollution, 17(4), 361–377. https://doi.org/10.1007/bf00460104

Wohlfahrt, G., Bianchi, K., & Cernusca, A. (2006). Leaf and stem maximum water storage capacity of herbaceous plants in a mountain meadow. Journal of Hydrology, 319(1–4), 383–390. https://doi.org/10.1016/j.jhydrol.2005.06.036

Wu, Z., Schwede, D. B., Vet, R., Walker, J. T., Shaw, M., Staebler, R., & Zhang, L. (2018). Evaluation and Intercomparison of five North American dry deposition algorithms at a mixed forest site. Journal of Advances in Modeling Earth Systems, 10(7), 1571–1586. https://doi.org/10.1029/2017ms001231

Wu, Z., Staebler, R., Vet, R., & Zhang, L. (2016). Dry deposition of O3 and SO2 estimated from gradient measurements above a temperate mixed forest. Environmental Pollution, 210, 202–210. https://doi.org/10.1016/j.envpol.2015.11.052

Wuyts, K., De Schrijver, A., Staelens, J., Gielis, L., Vandenbruwane, J., & Verheyen, K. (2008). Comparison of forest edge effects on throughfall deposition in different forest types. Environmental Pollution, 156(3), 854–861. https://doi.org/10.1016/j.envpol.2008.05.018

Xu, X., Yu, X., Bao, L., & Desai, A. R. (2019). Size distribution of particulate matter in runoff from different leaf surfaces during controlled rainfall processes. Environmental Pollution, 255, 113234. https://doi.org/10.1016/j.envpol.2019.113234

Xu, X., Zhang, Z., Bao, L., Mo, L., Yu, X., Fan, D., & Lun, X. (2017). Influence of rainfall duration and intensity on particulate matter removal from plant leaves. Science of The Total Environment, 609, 11–16. https://doi.org/10.1016/j.scitotenv.2017.07.141

Yang, Y., Jing, L., Li, Q., Liang, C., Dong, Q., Zhao, S., Chen, Y., She, D., Zhang, X., Wang, L., Cheng, G., Zhang, X., Guo, Y., Tian, P., Gu, L., Zhu, M., Lou, J., Du, Q., Wang, H., … Wang, W. (2023). Big-sized trees and higher species diversity improve water holding capacities of forests in Northeast China. Science of The Total Environment, 880, 163263. https://doi.org/10.1016/j.scitotenv.2023.163263

You, Y., O'Brien, J. M., Cole, A. S., Zhang, L., He, Z., Feng, J., & Pearson, S. (2024). Contribution of emissions from the oil sands activities in Alberta, Canada to atmospheric concentration and deposition of nitrogen and sulfur species at a downwind site. *Environmental Pollution*, *356*, 124301. https://doi.org/10.1016/j.envpol.2024.124301

Yu, Q., Tang, C., & Kuo, J. (2000). A critical review on methods to measure apoplastic pH in plants. Plant and Soil, 219(1/2), 29–40. https://doi.org/10.1023/a:1004724610550

Zhai, J., Cong, L., Yan, G., Wu, Y., Liu, J., Wang, Y., Ma, W., & Zhang, Z. (2018). Dry deposition of particulate matter and ions in forest at different heights. International Journal of Environmental Research, 13(1), 117–130. https://doi.org/10.1007/s4S51742-018-0158-z

Zhang, J., Moran, M. D., Zheng, Q., Makar, P. A., Baratzadeh, P., Marson, G., Liu, P., & Li, S.-M. (2018). Emissions preparation and analysis for multiscale air quality modeling over the Athabasca Oil Sands Region of Alberta, Canada. Atmospheric Chemistry and Physics, 18(14), 10459–10481. https://doi.org/10.5194/acp-18-10459-2018

Zhang, L., Wright, L. P., & Asman, W. A. (2010). Bi-directional air-surface exchange of atmospheric ammonia: A review of measurements and a development of a big-leaf model for applications in regional-scale air-quality models. *Journal of Geophysical Research: Atmospheres*, *115*(D20). https://doi.org/10.1029/2009jd013589

Zhang, W., Zhang, Z., Meng, H., & Zhang, T. (2018). How does leaf surface micromorphology of different trees impact their ability to capture particulate matter? *Forests*, *9*(11), 681. https://doi.org/10.3390/f9110681

Zheng, G., & Li, P. (2019). Resuspension of settled atmospheric particulate matter on plant leaves determined by wind and leaf surface characteristics. Environmental Science and Pollution Research, 26(19), 19606–19614. https://doi.org/10.1007/s11356-019-05241-8